Bulletin of Romanian Chemical Engineering Society

ISSN 2360-4697

Bulletin of Romanian Chemical Engineering Society

Volume 1   2014   Number 1

Contents

TEG DEHYDRATION OF NATURAL GAS: VOLUMETRIC MASS AND HEAT TRANSFER COEFFICIENTS IN PACKED BED ABSORBERS

Teodor TODINCĂ[1], Alexandru-Dan FILEP[1*], Teodor MUREȘAN[2]

[1]Depart. Applied Chemistry and Engineering of Natural Organic Compounds, POLITEHNICA University Timișoara, 2 Piața Victoriei, 300006, Timișoara, Romania
[2]S.C. ARMAX GAZ S.A. Mediaș, Romania

Abstract

In the design of triethylene glycol (TEG) natural gas dehydration units, the correct estimation of absorber size is essential in terms of both efficiency and costs. In this paper, volumetric mass and heat transfer coefficients are estimated by comparing structured packing industrial absorbers experimental data with the simulation results of a non-isothermal model describing phases composition and temperature modifications along packing height. Due to non-ideal behavior of water-TEG mixture, Parrish et al. empirical correlations have been used for the evaluation of the activity coefficients in the liquid phase. In the range of experimental data, volumetric overall mass transfer coefficient is found to be a function of gas phase F-factor (superficial gas velocity multiplied by the square root of the gas density) and liquid phase Reynolds and Schmidt numbers. The values of gas to liquid heat transfer coefficient confirms the effect of simultaneous condensation and mass transfer on heat transfer, its value being few times higher than those predicted by Chilton - Colburn analogy.

Keywords: volumetric overall mass transfer coefficient, gas-liquid heat transfer coefficient, natural gas dehydration, structured packing, TEG

1. Introduction

As extracted through wellheads, natural gas (NG) is associated with water, crude oil and gaseous components like CO_2, N_2, H_2S, etc. A preliminary NG separation from these unnecessary/dangerous components for further NG processing is taking place at the field level in the so-called first stage separators. Gas leaving these separators is saturated with water, a component which amount should be

---

* Coressponding author: E-mail address: alexandru-dan.filep@upt.ro (A. D. Filep)

decreased at levels avoiding ice or hydrates formation and the corrosion of the transport pipe lines due to the presence of CO_2 or H_2S.

In function of natural gas parameters, several methods for drying natural gas are available [1,2]: compression and cooling, absorption in selective liquids, adsorption on solid desiccants (silica gel, activated alumina), hydration of deliquescent compounds ($CaCl_2$, LiCl) etc. One of the most widely used processes is water absorption in glycols, especially in triethylene glycol (TEG) - which is preferred due to its high water absorption capacity, high thermal stability (285 ºC boiling temperature) and small vapor pressure. Typically, a TEG dehydration unit contains a contactor (absorber) where water is absorbed in the counter-current lean TEG flow, a flash tank acting as a three phase separator (pressure is decreased at values usually around 3-4 bar – the hydrocarbons retained in the absorber are separated from the rich TEG), filters, rich/lean TEG heat exchangers (lean TEG going to contactor is cooled down by the rich TEG) and, finally, a regenerator where water is boiled out of TEG. Usually, the regeneration unit contains a so called still column where rich TEG is entering between its transfer (bottom) and rectification (top) sections and a reboiler (heat being provided by firing natural gas or electrically) in which the temperature is limited to values up to 204 ºC because of TEG increasing decomposition at higher temperatures. For this reason, at an operating pressure slightly above atmospheric pressure, one can reach up to 98.8 w% TEG in the lean TEG. Such degree of regeneration is not enough at relatively high temperatures and low pressures of wet gas if specifications as a water dew point of -15 ºC (at operating or another pressure) or water content of 7 lbs/MMSCF are asked. Lean TEG regeneration up to 99.9 w% TEG can be reached by using a stripping gas which is injected in counter current with the TEG leaving the reboiler in a short column (the "stripping" column). Such column is placed between a surge tank and the reboiler (Figure 1).
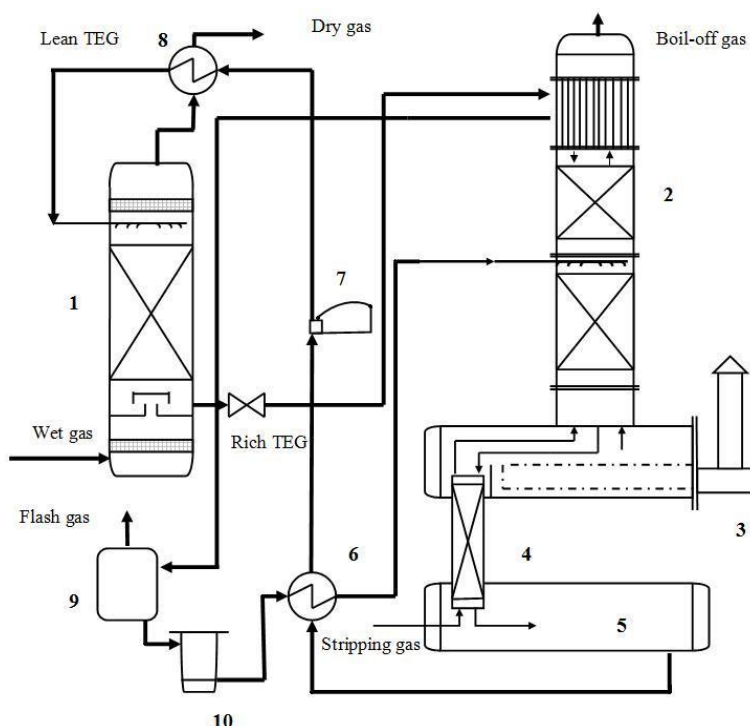
Fig. 1. Process scheme for a typical TEG dehydration unit.
1 – contactor (absorber); 2 – still column; 3 – reboiler; 4 – stripping column; 5 – surge drum; 6 – rich TEG/lean TEG heat exchanger; 7 – TEG pumps; 8 – gas/TEG heat exchanger; 9 – flash drum; 10 – filters

From simulation point of view, Aspen HYSYS software with its Peng Robinson/Glycol property packages is the main tool used for the flowsheeting of the TEG dehydration units.

If initally glycol – gas contactors were developed as trayed towers, in the last decades structured packings became an attractive option because of their hydraulic performances in terms of irrigation, gas load, pressure drop, etc.

Armax Gaz S.A., one of the main Romanian companies in the field of manufacturing equipment and devices for gas and oil industry, is actually delivering TEG based dehydration units in a large range of NG flow rate (20000 – 5000000 Nm^3/day) and pressure (5- 80 barg). In the design of TEG natural gas dehydration units, the correct estimation of absorber size is essential in terms of water removal efficiency, glycol loses (entrainment, vaporization), investment and operating costs. If in the final step of the contactor design structured packing manufacturer evaluation is decisive, an initial estimation of absorber size is necessary in order to account for investment costs and for main operating

parameter values. Guidance for such estimation can be found in well known specification API Spec 12GDU [3], engineering texts like GPSA Engineering Data Book [1] or open literature [4]. A preliminary size of the contactor can be also quickly calculated on the basis of HYSYS „column" unit operation by using „tray" utility, the number of teoretical stages resulted for reaching water content in gas (tower outlet) and folowing the rules of thumbs [1] for the estimation of HETP (height equivalent to a teoretical plate). Comparing with real plants data, such methodologies revealed as not enough accurate in predicting structured packing performances.

In this paper, for a better evaluation of structured packing height asked for reaching dryed gas water content targeted by TEG unit design, volumetric mass and heat transfer coefficients have been estimated by comparing industrial plants experimental data with the simulation results of a non-isothermal plug flow model describing phases composition and temperature modifications along packing height.

2. Experimental, contactor modeling and tuning of the model parameters

One of the most important issues to be correctly accounted for in the contactor design is the behavior of TEG – water mixture. In the last years improvement of equation of state methods can be found in literature [5, 6] but, because Parrish et al. methodology for the calculation of component activities is largely used in the industry practice, these hyperbolic equations have been chosen for the evaluation of TEG –water mixture non ideality [5]:

$$\ln(\gamma_{TEG}) = \frac{B^2 \cdot \ln[\cosh(\tau)]}{A} - \frac{x_w \cdot B \cdot \tanh(\tau)}{x_{TEG}} - C^2 \cdot x_w^2 \tag{1}$$

$$\ln(\gamma_w) = B \cdot [\tanh(\tau) - 1] - C \cdot x_{TEG}^2 \tag{2}$$

where:

$$\tau = \frac{A \cdot x_w}{B \cdot x_{TEG}} \tag{3}$$

$$A = \exp(-12.792 + 0.03293 \cdot T_K) \tag{4}$$

$$B = \exp(0.77377 - 0.00695 \cdot T_K) \tag{5}$$

$$C = 0.88874 - 0.001915 \cdot T_K \tag{6}$$

At moderate pressure, assuming a non-ideal gas and liquid behavior, gas phase mole fraction in equilibrium with liquid composition at a given temperature is:

$$y_w^* = x_w \cdot \gamma_w \cdot \frac{\phi_w^{sat} \cdot p_w^{sat}}{P \cdot \phi_w}$$

(7)

In the relations 1-7, x_w and x_{TEG} are water and TEG mole fractions in liquid phase, γ_w and γ_{TEG} are activity coefficients of water and TEG, P is the total pressure, p_w^{sat} is the saturated water vapor pressure (at operating temperature), y_w^* is equilibrium water mole fraction in the gas phase, ϕ_w and ϕ_w^{sat} are water fugacity coefficients in the gas mixture (at operating pressure and temperature) and of pure water (at p_w^{sat} and operating temperature), T_K is temperature in K.

Plant data from three TEG dehydration units covering nominal flow rates up to 3000000 Nm^3/day and working pressures between 15 and 40 bar have been analyzed for the evaluation of volumetric mass transfer coefficients in different operating conditions (gas velocities between 0.1 and 0.75 m/s, liquid stripping densities up to 2 m^3/(m^2·hr). A typical set of data is shown in table 1.

The simplest way to calculate volumetric mass transfer coefficient $Kya = K_y \cdot a$ is based on a gas mole balance in a differential tower volume:

$$Kya = \frac{G_0}{H} \int_{y_w^{btm}}^{y_w^{top}} \frac{dy_w}{(1 - y_w)^2 \cdot (y_w - y_w^*)} \approx \frac{G_0}{H} \int_{y_w^{btm}}^{y_w^{top}} \frac{dy_w}{(y_w - y_w^*)}$$

(8)

where: Kya is the volumetric overall mass transfer coefficient based on mole fraction driving force in $kmol/(m^3 \cdot hr)$, G_0 is the gas molar flow rate per square meter of tower transversal area in $kmol/(m^2 \cdot hr)$, H is the tower height in m, btm and top superscripts stands for tower bottom and top gas entry/exit.

The value of the integral in equation 8 is the number of transfer units, simplification of the first integral being due to the very small water mole fraction in gas. At constant gas molar flux along the tower height, operating line can be expressed as:

$$y_w = \frac{y_w^{btm} + \dfrac{L_0^{TEG}}{G_0} \cdot \left(\dfrac{x_w}{1 - x_w} - \dfrac{x_w^{btm}}{1 - x_w^{btm}} \right)}{1 + y_w^{btm} + \dfrac{L_0^{TEG}}{G_0} \cdot \left(\dfrac{x_w}{1 - x_w} - \dfrac{x_w^{btm}}{1 - x_w^{btm}} \right)} \tag{9}$$

where L_0^{TEG} is the molar TEG flow rate divided by the column transversal area in $kmol/(m^2 \cdot hr)$.

Assuming ideal gas behavior, water vapor equilibrium mole fraction can be calculated as in relation 7 by setting fugacity coefficients to 1. Operating and equilibrium lines in x-y diagram at the average value of the temperature in contactor are presented in figure 2. The number of transfer units can be calculated by graphical integration of equation 8 or by using an analytical solution of the integral like Kremser equation [7].

Table 1

Industrial TEG contactor typical operating parameters

Parameter	Value	Parameter	Value
Packing nominal specific surface	250 m^2/m^3	Operating pressure	16 barg
Gas inlet temperature	34.8 °C	Liquid inlet temperature	40.7 °C
Gas velocity	0.68 m/s	Liquid stripping density	1.4 $m^3/(m^2 \cdot hr)$
Gas water mole fraction - gas inlet	0.005	Water mole fraction in liquid -TEG inlet)	0.0295
Gas water mole fraction - gas outlet	0.000142	Water mole fraction in liquid - TEG outlet	0.435
Gas outlet temperature	40.5 °C	Liquid outlet temperature	36.3 °C
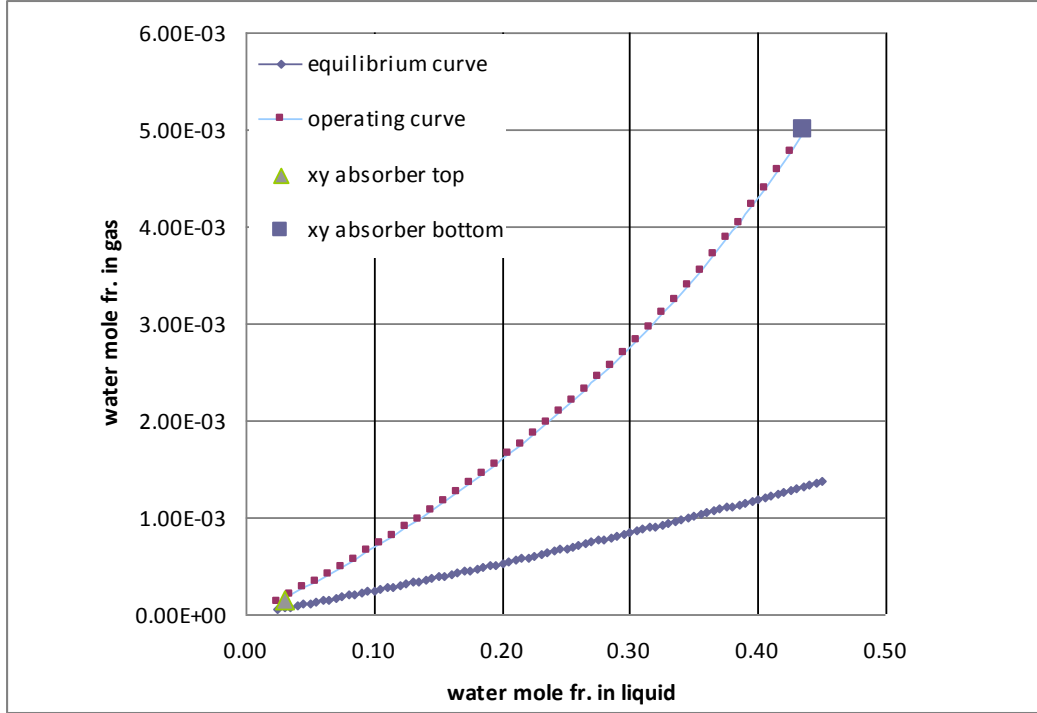
Fig. 2. Operating and equilibrium curves for the operating data mentioned in Table 1.

Such approach cannot account for non-ideal gas behavior, phases temperature modifications along packing height, etc. For this reason, in the evaluation of the volumetric mass and heat transfer coefficients a non-isothermal plug flow model has been used. The model equations are shown below:

$$\frac{dL}{dh} = -Kya \cdot H \cdot S \cdot \left(y_w - y_w^*\right)$$
(10)

$$\frac{dy_w}{dh} = -\frac{Kya \cdot H \cdot S}{G} \cdot \left(y_w - y_w^*\right)$$
(11)

$$\frac{dx_w}{dh} = -\frac{Kya \cdot H \cdot S}{L} \cdot \left(y_w - y_w^*\right) - \frac{x_w}{L} \cdot \frac{dL}{dh}$$
(12)

$$\frac{dT_G}{dh} = \frac{\alpha_V \cdot \left(T_L - T_G\right) \cdot H \cdot S - Kya \cdot H \cdot S \cdot \left(y_w - y_w^*\right) \cdot c_M^G \cdot T_G}{G \cdot c_M^G}$$
(13)

$$\frac{dT_L}{dh} = \frac{-\alpha_V \cdot (T_L - T_G) \cdot H \cdot S + Kya \cdot H \cdot S \cdot (y_w - y_w^*) \cdot (\Delta H_{abs} + c_M^G \cdot T_G)}{L_M \cdot c_{SL}}$$

(14)

Boundary conditions:

$$\text{at } h=0 \quad y_w = y_w^{btm} \qquad T_G = T_G^{btm} \qquad\qquad (15)$$
$$\text{at } h=H \quad x_w = x_w^{top} \qquad T_L = T_L^{top} \qquad L = L^{top}$$

In the relations (10) – (15), G and L are the gas and liquid molar flow rates in *kmol/hr*, S is tower transversal area in m^2, h is axial coordinate in m, T_G and T_L are gas and liquid temperatures in Celsius degrees, L_m is liquid mass flow rate in kg/hr, α_V is the volumetric heat transfer coefficient in $kJ/(m^3 \cdot hr \cdot °C)$, ΔH_{abs} is water molar heat of absorption (condensation and solution in TEG), c_M^G is the molar heat capacity of gas in $kJ/(kmol \cdot °C)$ and c_{SL} is the mass heat capacity of the liquid in $kJ/(kg \cdot °C)$.

While activities in the liquid phase have been calculated on the basis of Parrish et al. hyperbolic equations (1-6), all other physical properties (fugacity coefficients, gas and liquid phases heat capacities, densities, etc.) have been evaluated by using Aspen Custom Modeler property procedures and Aspen Plus Peng Robinson equation of state.

For the estimation of volumetric mass and heat transfer coefficients, the equations 10 -14 with boundary conditions 15 have been solved numerically, Kya and α_V values being tuned in order to reach plant data. Typical results are shown in the figures 3 (composition profile) and 4 (temperature profile).

Volumetric heat transfer coefficient value has been also checked by comparing the value estimated by integration with the value calculated on the basis of contactor heat balance and using average temperatures of the gas and liquid [8].

Similar steps have been used in the evaluation of volumetric transfer coefficients for 11 other sets of data collected from TEG units under different operating conditions, in total 12 sets being used in view of developing correlations for volumetric mass and heat transfer coefficients estimation. For all cases, structured packing specific surface is 250 m²/m³.
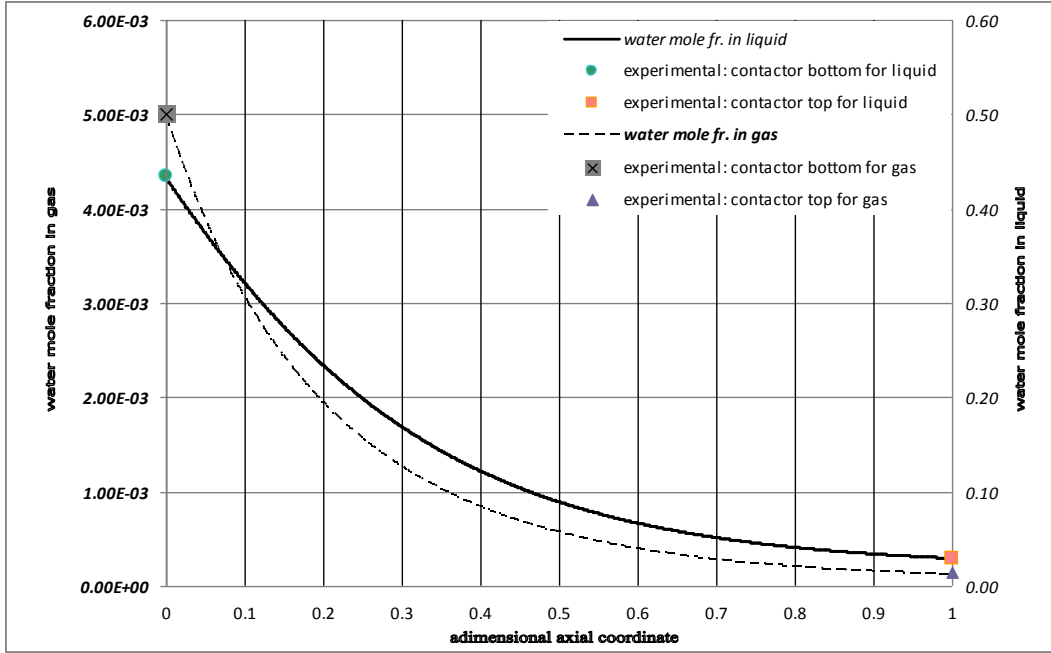
Fig. 3. Gas and liquid water mole fraction profiles for the data from Table 1 (Kya = 1750 kmol/(m³·hr), α_V = 90 kW/(m³·°C)).
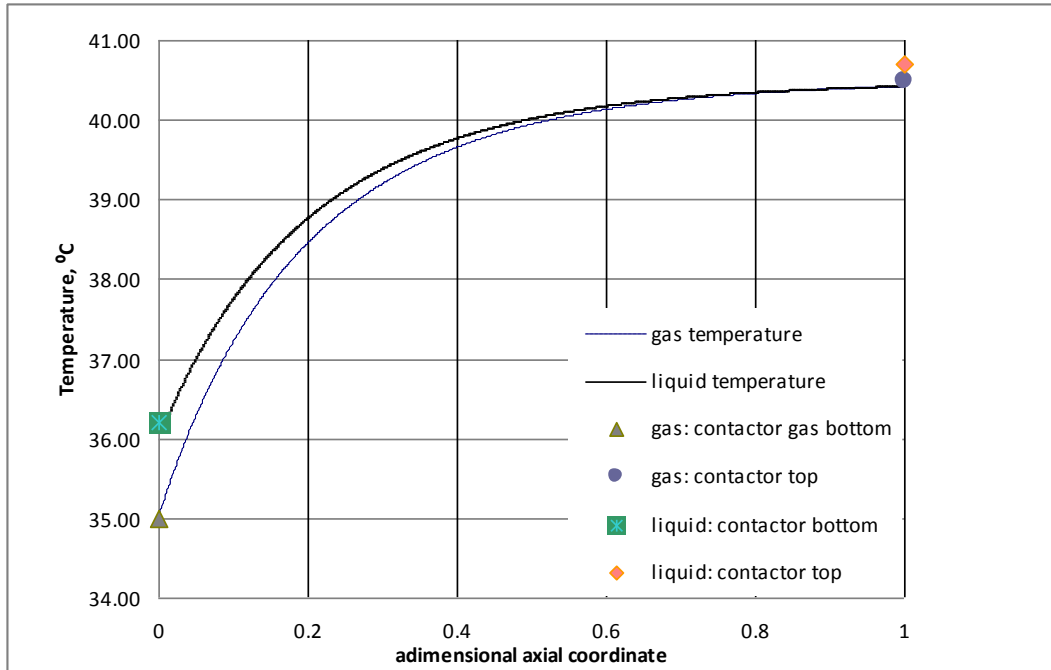
Fig. 4. Gas and liquid temperature profiles for the data from Table 1 (Kya = 1750 kmol/(m³·hr), α_V = 90 kW/(m³·°C)).

3. Results analysis and best fitted correlations

Despite of the important number of mass transfer correlations for packed beds which can be found in the open literature [9, 10, 11], no one of these correlations has been found enough accurate to account for the complexity and particularities of water absorption in TEG process. Phases non-ideal behavior, hydraulics of structured packing at TEG contactors operating conditions and the characteristics of the distributors used in industrial practice could explain these differences.

In many specific cases in which the evaluation of mass transfer coefficients is focusing on a specific process, very simple expressions are taken into account. For example, in the simultaneous determination of volumetric mass transfer coefficients, Linek [12] expressed both vapor and liquid side coefficients as functions of superficial velocity and diffusion coefficients. In case of natural gas TEG dehydration process, for the evaluation of volumetric overall mass transfer coefficient, the following expression has been found as giving best results:

$$Kya = \varphi_1 \cdot \left(F_f\right)^{\varphi_2} \cdot \left(\frac{Re_L}{h_L}\right)^{\varphi_3} \cdot Sc_L^{0.33}$$

(16)

where:

$$h_L = \varphi_4 \cdot \left(\frac{\eta_L}{\rho_L} \cdot w_L \cdot a_P^2\right)^{0.33}$$

(17)

$$F_f = w_g \cdot \sqrt{\rho_G}$$

(18)

$$Re_L = \frac{d_{SP} \cdot w_L \cdot \rho_L}{\eta_L}$$

(19)

$$Sc_L = \frac{\eta_L}{\rho_L \cdot D_L}$$

(20)

In the equations 16-20: h_L is liquid hold up (m^3/m^3), η_L and ρ_L are liquid viscosity and density, w_L is liquid superficial velocity (m/s), a_P is packing specific surface (m^2/m^3), F_f is the F factor, w_g is gas velocity (m/s), ρ_G is gas density (kg/m^3), Re_L is liquid Reynolds number, d_{SP} is structured packing equivalent diameter (calculated as $4\varepsilon_P/a_P$, a_P=250 m^2/m^3, ε_P – bed voidage), Sc_L is liquid Schmidt number, D_L is water diffusion coefficient in liquid (m^2/s). For liquid hold-up an expression similar with Billet et al. [13] equation has been taken into consideration.

The parameters $\varphi_1 - \varphi_4$ from equations 16 and 17 have been estimated by minimizing the square sum of the differences between calculated values according to the procedure mentioned above (tuning Kya and α_V for reaching plant data) versus the values predicted by the equation 16. The final expressions for overall volumetric mass transfer coefficient and liquid hold up are presented below:

$$Kya = 8.424 \cdot \left(F_f \right)^{0.85} \cdot \left(\frac{\mathrm{Re}_L}{h_L} \right)^{0.41} \cdot Sc_L^{0.33}$$

(21)

$$h_L = 0.41 \cdot \left(\frac{\eta_L}{\rho_L} \cdot w_L \cdot a_P^2 \right)^{0.33}$$

(22)

A comparison between the calculated values of Kya for each set of plant data and those predicted by the equation 21 is shown in Figure 5.

Despite of the importance of the evaluation of gas-liquid heat transfer coefficient for the design of gas-liquid contactors the available information is still scarce and the situation is even worse in the case of structured packing. Some correlations are present in the literature for few particular cases like packed bed type direct air – water contactors [8, 14], air dehumidificators [15], heat recovery through direct contact systems [16], etc.

In principle, in the case of no correlation is available in the range of system operating parameters, an estimation can be made on the basis of heat transfer/mass transfer analogy [12, 16]. This approach has been used also in this paper - on the basis of Chilton - Colburn analogy, volumetric gas-liquid heat transfer coefficient is expressed in function of volumetric overall mass transfer and the ratio of Schmidt and Prandl numbers:

$$\alpha_V = \varphi_5 \cdot Kya \cdot \left(M_w \cdot c_{SG} \right) \cdot \left(\frac{Sc_G}{\mathrm{Pr}_G} \right)^{0.66}$$

(23)

In the equation 23, φ_5 value has been tuned in view of minimizing the square of the differences between heat transfer coefficient value estimated through simulation (as described in the paragraph #2) and the values predicted by the equation 23. The best fitted value, for all 12 experimental point has shown an increase of around 5 times of volumetric gas – liquid heat transfer coefficient comparing with the values predicted by Chilton – Colburn analogy. As mentioned

by Kypridzis [8], this increase is due to the sensible heat exchange between phases, which takes place simultaneously with the mass transfer.
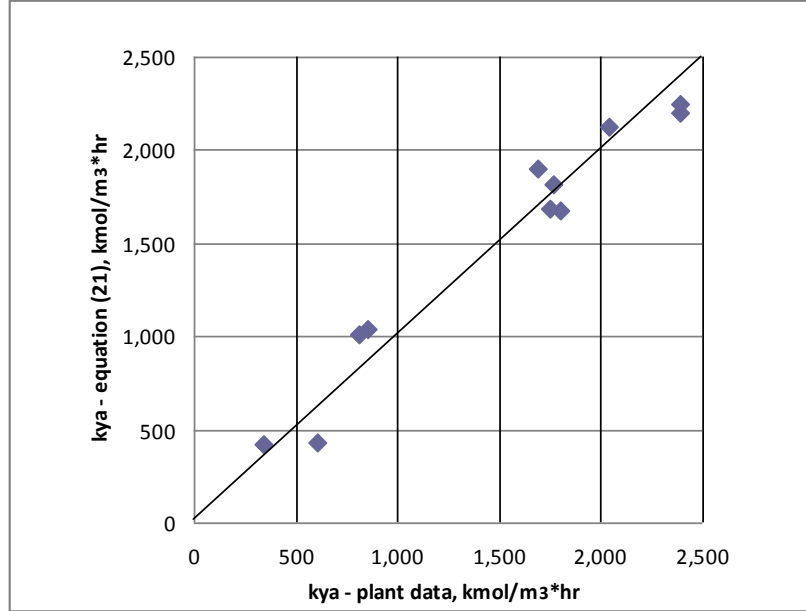
Fig. 5. Comparison between calculated values of *Kya* (from sets of experimental data) and the values predicted by the equation 21.

4. Conclusions

In this paper, volumetric mass and heat transfer coefficients for TEG dehydration of natural gas in the particular case of structured packing towers have been estimated by comparing industrial plants experimental data with the simulation results of a non-isothermal plug flow model. Phases non-ideality has been accounted for by the calculation of the activity coefficients in the liquid phase and using Peng Robinson equation of state for the gas phase.
Volumetric overall mass transfer coefficient has been expressed as function of F factor, liquid Reynolds and Schmidt numbers and liquid hold-up in the column. Gas-liquid heat transfer coefficient has been estimated on the basis of Chilton – Colburn analogy. The values of gas to liquid heat transfer coefficient confirms the effect of simultaneous condensation with mass transfer on heat transfer, the values of gas-liquid mass transfer being few times higher than those predicted by Chilton - Colburn analogy.

REFERENCES

[1]   GPSA Engineering Data Book - *Gas Processors and Suppliers Association*, Tulsa, OK, USA, 12th edition, 2004.

[2]   Netusil M., Ditl P., Comparison of three methods for natural gas dehydration. *Journal of Natural Gas Chemistry*, 20 (5), (2011), 471–476.

[3]   API Spec 12GDU, American Petroleum Institute. Production Dept. *Specification for glycol-type gas dehydration units*. American Petroleum Institute, 1990.

[4]   Bahadori A., Vuthaluru H.B., Simple methodology for sizing of absorbers for TEG (triethylene glycol) gas dehydration systems. *Energy*, 34 (11), (2009), 1910–1916.

[5]   Twu C.H., Tasone V., Sim W.D., Watanasiri S., Advanced equation of state method for modeling TEG–water for glycol gas dehydration. *Fluid phase equilibria*, 228, (2005), 213–221.

[6]   Carnelli L., Lazari C., Caretta A., Pandolfi G., Valli F., Ceradini G., Scerra S., Experimental activity of distillation, thermodynamic model and simulation for performance analysis of a glycol reclaiming unit. *Journal of Natural Gas Science and Engineering*, 10, (2013), 89–98.

[7]   Treybal R., *Mass-Transfer Operations*. McGraw-Hill Book Company, 1981.

[8]   Kypritzis S., Karabelas A.J., Direct contact air-water heat transfer in a column with structured packing. 5th World Conference on Experimental Heat Transfer, Fluid Mechanics, and Thermodynamics, Thessaloniki, Greece, 2001

[9]   Larachi F., Lévesque S., Grandjean B.P.A., Seamless mass transfer correlations for packed beds bridging random and structured packings. *Industrial and Engineering Chemistry Research*, 47 (9), (2008), 3274–3284.

[10] Orlando A.E., Medina L.C., Mendes M.F., Nicolaiewsky E.M.A., HETP evaluation of structured packing distillation column. Brazilian Journal. of Chemical Engineering, 26 (3), (2009), 619–633.

[10] New mass-transfer correlations for packed towers. *American Institute of Chemical Engineers Journal*, 58 (1), (2012), 132–152.

[12] Linek V., Kordač M., Moucha T., Mechanism of mass transfer from bubbles in dispersions: part II: mass transfer coefficients in stirred gas–liquid reactor and bubble column. *Chemical Engineering and Processing: Process Intensification*, 44 (1), (2005), 121–130.

[13] Billet R., Schultes M., Prediction of mass transfer columns with dumped and arranged packings: updated summary of the calculation method of Billet and Schultes. *Chemical Engineering Research and Design*, 77 (6), (1999), 498–504.

[14] Floarea O., Jinescu G., Balaban C., Vasilescu P., Dima R., *Operaţii şi utilaje în industria chimică. Probleme*, E.D.P, Bucureşti, 1980.

[15] Rahimi A., Babakhani D., Mathematical modeling of a packed-bed air dehumidifier: The impact of empirical correlations. *Journal of Petroleum Science and Engineering*, 108, (2013), 222–229.

[16] Fair J.R., Bravo J.L, Energy Recovery By Direct Contact Gas-Liquid Heat Exchange. *Proceedings from 10th Annual Ind. Energy Conference*, Houston, (1988), 13–15.

MODELLING AND EVALUATION OF CHEMICAL REACTORS FOR ISOBUTENE DIMERIZATION

Petru I. DRAGNEA, Costin Sorin BÎLDEA*

Depart. Chemical and Biochemical Engineering, POLITEHNICA University of Bucharest, 1-7 Gh. Polizu, 011061, Bucharest, Romania

Abstract

Dimerization of isobutene (IB) to di-isobutene (DIB) is seen as an attractive alternative for the production isooctane. This species can be added in gasoline blends for octane number enhancement. In this article, the performance of batch, continuous stirred tank and plug-flow reactors is analyzed. For the plug-flow reactor, two models are investigated. The pseudo-homogeneous model neglects the heat and mass transfer resistances in the liquid film around the catalyst particle. With the heterogeneous model these effects are included. The calculation of the heat and mass transfer coefficients in the liquid film is performed and their influence on several reaction parameters is presented.

Keywords: oligomerizarion, liquid phase reactors, catalysts, dimensionless analysis

1. Introduction

Dimerization of isobutene (*IB*) to obtain di-isobutene (*DIB*) followed by the hydrogenation of the later one is seen to be a valuable alternative, besides the alkylation process, for the isooctane production. Isooctane has a high commercial interest since it can successfully replace the current well disputed MTBE compound, associated with many environmental issues.

Previous studies focused on determining the kinetics of both wet (with tert-butanol or water as selectivity enhancers) and dry IB dimerization in continuous stirred (CSTR) and discontinuous (DC) reactors [1-3]. The main outcomes were: a) besides the main dimerization reaction, several oligomerization side reactions occur b) the presence of polar components plays an important role in selectivity improvement and c) the reaction kinetics in the presence and absence of polar compounds (wet and dry) is likely to be significantly different. Moreover, the kinetics determined was used to analyze the behavior of the reaction system in

---

* Corresponding author: E-mail address: s_bildea@upb.ro (C.S. Bîldea)

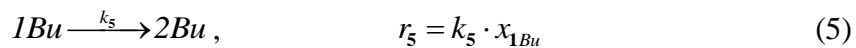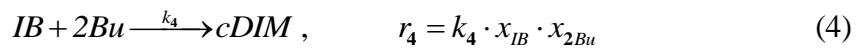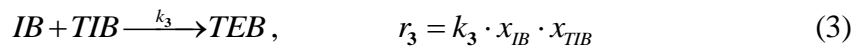continuous and batch reactive distillation columns with the purpose of reaching higher selectivity towards the isooctene products, up to 93%.

The present paper presents a study of the (dry) isobutene dimerization, based on the kinetics presented by Tawalkar et al. [1]. The goal of the paper is finding the critical parameters that influence the conversion and selectivity in several reactor types. First, the model of a discontinuous (DC) reactor is developed and the results are compared and validated against the previous published outcomes. Then, the kinetics is used for analyzing the behavior of a CSTR. Finally, the behavior of the plug-flow reactor (PFR) is analyzed, demonstrating the influence of the resistance to heat and mass transfer around the catalyst.

2. Reaction system

Reactions and Kinetics

The dimerization of isobutene can be performed in the presence of a solid acid catalyst such as ion exchange resins or zeolites. The reactions take place in liquid phase and are highly exothermic. The reaction system consists of the following parallel consecutive reactions, where *IB*, *DIB*, *TIB* and *TEB* stand for isobutene, di-isobutene, tri-isobutene and tetra-isobutene, respectively. Usually, the feed stream contains significant amounts of 1-butene (*1Bu*) which is isomerized to 2-butene (*2Bu*). The reaction between isobutene and 2-butene leads to a mixture of octene isomers, known as c-dimer (*cDIM*). The reaction rates [1] are given by relations (1)-(5), where x_k stands for the mole fraction of species k. The kinetic parameters are presented in Table 1.

$$IB + IB \xrightarrow{\ k_1\ } DIB, \qquad r_1 = k_1 \cdot x_{IB}^2 \qquad (1)$$

$$IB + DIB \xrightarrow{\ k_2\ } TIB, \qquad r_2 = k_2 \cdot x_{IB} \cdot x_{DIB} \qquad (2)$$

$$IB + TIB \xrightarrow{\ k_3\ } TEB, \qquad r_3 = k_3 \cdot x_{IB} \cdot x_{TIB} \qquad (3)$$

$$IB + 2Bu \xrightarrow{\ k_4\ } cDIM, \qquad r_4 = k_4 \cdot x_{IB} \cdot x_{2Bu} \qquad (4)$$

$$1Bu \xrightarrow{\ k_5\ } 2Bu, \qquad r_5 = k_5 \cdot x_{1Bu} \qquad (5)$$
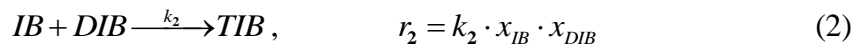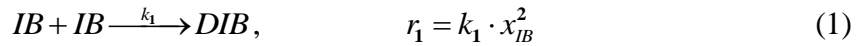
Considering the high activation energies of reactions (1) and (5), it is expected that the formation of the useful products *DIB* and *cDIM* is favored by high temperatures. However, the experimental data and catalyst information [1] [3], indicate that the reaction temperature should not exceed 130 °C in order to avoid

catalyst deactivation. This factor is a major process constraint which prevents high selectivity.

Kinetic data [1]

Reaction no.	Pre-exponential factor, k_i (mol/kg/s)	Activation energy, E_a (kJ/mol)
1	$3.01 \cdot 10^{13}$	89.3
2	$3.38 \cdot 10^{4}$	26.7
3	$6.45 \cdot 10^{4}$	31.0
4	$1.32 \cdot 10^{8}$	57.6
5	$5.63 \cdot 10^{11}$	86.1

3. Discontinuous Reactor (DC)

In the discontinuous reactor, the reaction takes place in liquid phase, at constant temperature. The effect of the external mass and heat transfer resistances from/to the catalyst particle can be neglected due to the high speed of agitation [1] and of small dimension of catalyst. The reactor model is characterized by species material balance equations, which are given by differential equations (6). The species mole fraction is computed by their definition relationship (7).

$$\frac{dn_i}{dt} = m_{cat} \cdot \sum_{j=1}^{R} v_{i,j} \cdot r_j(x) \qquad i = 1, NC \qquad (6)$$

$$n_i(t=0) = n_{i,0}$$

$$x_i = \frac{n_i}{\sum_{i=1}^{NC} n_i} \qquad (7)$$

Feed Composition

Component	Moles ($n_{i,0}$),	Mole fraction	Mass	Mass fraction
IB	44.5	0.380	2492	0.328
BU2	14.5	0.124	812	0.107
BU1	28.1	0.240	1573	0.207
IO	17.5	0.150	1999	0.263
I	12.4	0.106	719	0.095

Figure 1 presents the evolution of components mole fraction, obtained for the initial conditions presented in Table 2 and a catalyst amount $m_{cat} = 29$ kg (similarly to the experimental trials [1]).
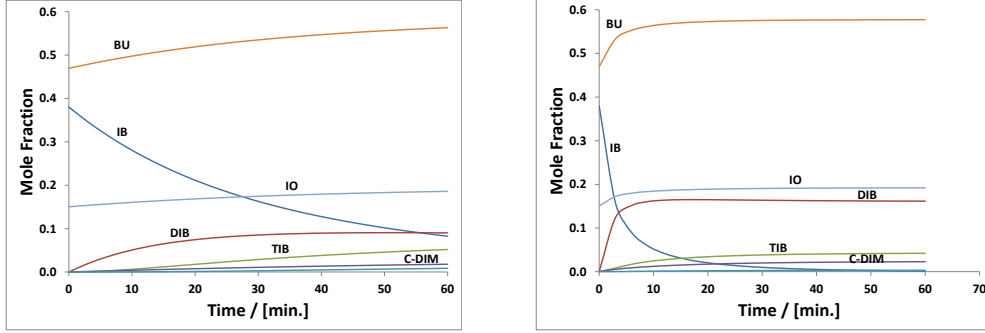
Fig. 1. Components mole fraction in a batch reactor a) at 363 K; b) at 393 K.

The selectivity towards the formation of *C8* species (*DIB* and *cDIM*), defined by equation (8), and the isobutene conversion are presented in Fig. 2, for two different values of the reaction temperature. As expected, high temperature increases both the conversion of *IB* and selectivity towards *C8*.

$$\sigma = \frac{2 \cdot n_{DIB} + n_{cDIM}}{2 \cdot n_{DIB} + 3 \cdot n_{TIB} + n_{cDIM} + 4 \cdot n_{TEB}} \tag{8}$$
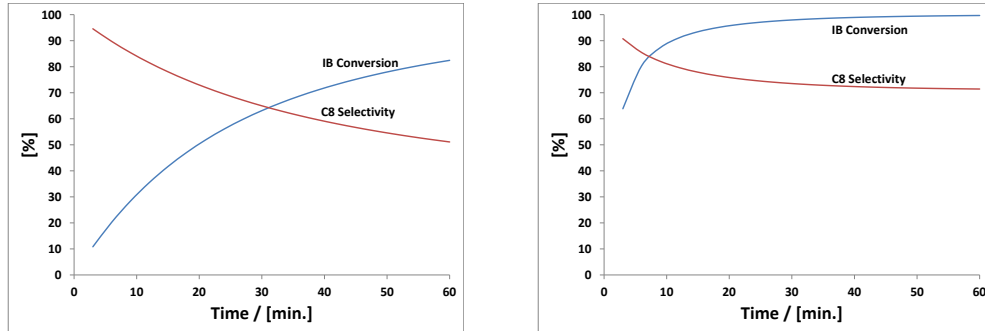
Fig. 2. Conversion of *IB* and selectivity towards C8 at: a) 363 K and b) 393 K.

Based on the closed match between the experimental data [1] and the prediction of the discontinuous reactor model, the kinetic model is further used for assesing the isobutene oligomerization reaction in other types of reactors.

4. Continuous Stirred Tank Reactor (CSTR)

The continuous stirred tank reactor (CSTR) model is analyzed based on the stoichiometry and kinetics previously presented. Since the reaction mixture is well mixed, the effects of the resistance to mass and heat transfer to/from the catalyst are negligible. Moreover, according to the experimental data [1], the catalyst size does not have a significant effect on the reaction rate either, and the internal diffusion could be neglected. The material balance is expressed by the following nonlinear system of equations:

$$F_{i,in} - F_{i,out} = m_{cat} \cdot \sum_{j=1}^{R} v_{i,j} \cdot r_j(x) \tag{9}$$

$$x_i = F_{i,out} \Big/ \sum_{i=1}^{NC} F_{i,out} \tag{10}$$

The feed flowrate is 117 kmol/h, with the composition listed in the Table 2. The catalyst load is m_{cat} = 29 kg. The results (Table 3) show the favourable effect of high reaction temperature. However, the lower CSTR performance, compared to DC reactor, should be remarked.

Table 3

CSTR Results

Temperature, K	IB Conversion, %	C8 Selectivity, %
363	65	47
393	88	56

5. Plug Flow Reactor (PFR)

Initial data

The analysis of the reaction system in a PFR is done based on the reactions and kinetics presented in section 2. The reactor geometry is presented in Table 4, while Table 5 presents the feed condition.

Table 4

Input Data

Tube diameter (*d*), mm	50
Tube length (*L*), m	50
Number of tubes	662
Catalyst diameter (d_p), mm	2
Cooling water temperature (T_c), °C	100
Amount of catalyst (m_{cat}), kg	112
Feed temperature, °C	100

Reactor Feed

Component	Mole flow, kmol/h	Mole fraction	Mass flow, kg/h	Mass fraction
IB	173.16	0.482	9697	0.479
1BU	91.73	0.255	5137	0.253
2BU	47.34	0.132	2651	0.131
Inert	47.22	0.131	2644	0.136

The pseudo-homogeneous model

The pseudo-homogeneous PFR model ignores the heat and mass transfer resistances in the liquid film around the catalysts, therefore assumes that the mole fractions and temperature at catalyst surface are identical to the ones in the bulk liquid. It consists of the following mass and energy balance equations:

$$\frac{d\xi_j}{dz} = S \cdot r_j \cdot \rho_{cat} \tag{11}$$

$$\frac{dT}{dz} = \frac{1}{u_0 \cdot \rho_0 \cdot c_p} \cdot \sum_{j=1}^{R} (r_j) \cdot (-\Delta H_{R,j}) - \frac{\frac{4}{d_t} U}{u_0 \cdot \rho_0 \cdot c_p} \cdot (T - T_c) \tag{12}$$

$$\xi_j (z=0) = 0; \; T(z=0) = T_0 \tag{13}$$

The mole fractions necessary to calculate the reaction rates are computed by relationships (14) and (15).

$$F_i = F_{0,i} + \sum_{j=1}^{R} \upsilon_{i,j} \cdot \xi_j \tag{14}$$

$$x_i = F_i \Big/ \sum_{i=1}^{NC} F_i \tag{15}$$

The overall heat transfer coefficient (*U*) from the bulk liquid (reaction mixture) to the cooling water is calculated by summation of thermal resistances, as shown by relation (16).

$$\frac{1}{U} = \frac{1}{\alpha_s} + \frac{\delta_p}{\lambda_p} + \frac{1}{\alpha_t} \tag{16}$$

The partial heat transfer coefficient on the cooling water side α_s is assumed to be constant $\alpha_s = 1000$ W/m$^2\cdot$K. The film transfer coefficient on the tube side α_t is determined from the following relationship [6]:

$$Nu = 2.26 \cdot Re_p^{0.8} \cdot Pr^{0.33} \cdot \exp\left(\frac{-6 \cdot d_p}{d_t}\right) \qquad (17)$$

Fig. **3** presents the variation of temperature, conversion and selectivity along the reactor. Although the reactor achieves high conversion and selectivity, the temperature peak exceeding the maximum allowable value of 130 °C should be observed. It should be noted that the temperature peak increases to almost 200 °C when the same amount of catalyst is used in a shorter reactor ($L = 5$ m).
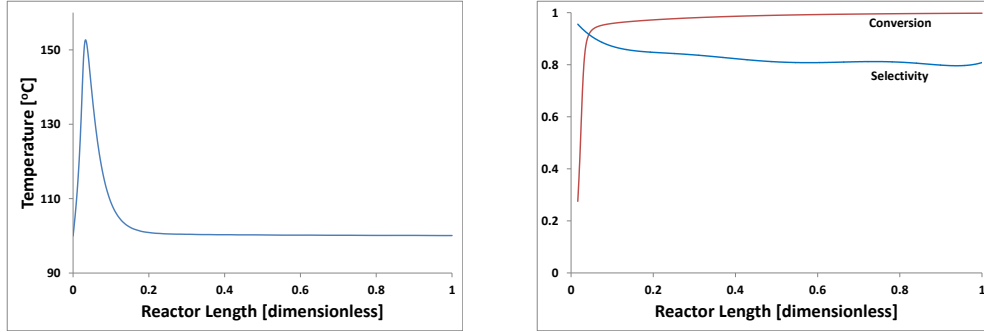
Fig. 3. Temperature (left) and conversion and selectivity profiles (right) along the PFR, as predicted by the pseudo-homogeneous model.

In order to elucidate the large temperature increase, the model is written in the following dimensionless form:

$$\frac{d\xi_{n,j}}{dl} = Da_j \cdot \exp\left(\frac{\gamma_j \cdot \theta}{1+\theta}\right) \cdot \prod_{i=1}^{NC} x_i^{\alpha_{i,j}} \qquad j = 1, R \qquad (18)$$

$$\frac{d\theta}{dl} = \sum_{j=1}^{R}\left(Da_j \cdot B_j \cdot \exp\left(\frac{\gamma_j \cdot \theta}{1+\theta}\right) \cdot \prod_{i=1}^{NC} x_i^{\alpha_{i,j}}\right) - \beta \cdot (\theta - \theta_C) \qquad (19)$$

$$\xi_{n,j}(l=0) = 0; \ \theta(l=0) = 0 \qquad (20)$$

The dimensionless model variables are the axial position, $l = z / L$, the reaction extents $\xi_{n,j} = \xi_j / F_{IB,0}$ and the temperature $\theta = \dfrac{\left(T - T_{ref}\right)}{T_{ref}}$. The dimensionless parameters represent the adiabatic temperature rise $B_j = \dfrac{c_{IB_0} \cdot \left(\Delta H_{r,j}\right)}{\rho_0 \cdot c_p} \cdot \dfrac{1}{T_{ref}}$, the heat transfer capacity $\beta = \dfrac{4 \cdot U \cdot c_{IB_0}}{\rho_0 \cdot c_p \cdot d_t \cdot \rho_{cat} \cdot k_1\left(T_{ref}\right)}$, Damköhler number, $Da_j = \rho_{cat} \cdot k_j\left(T_{ref}\right) \dfrac{V}{F_{IB_0}}$ and the activation energy, $\gamma_j = \dfrac{E_{a,j}}{R \cdot T_{ref}}$

For a 5 m reactor, the ratio between the adiabatic temperature rise B_1 and the heat transfer capacity β has a large value, $T_T = B_1 / \beta = 1.5$ which explains the difficulty of maintaining low temperature of the reaction mixture.

The heterogeneous model

The external heat and mass transfer resistances are important factors that should be considered in the model, due to their influence on the concentrations and temperature at catalyst surface. For exothermic reaction, the temperature at the catalyst surface T_s is higher than in the bulk, which can compromise the catalyst. Moreover, the higher concentration of the product (*DIB*) at catalyst surface enhances the secondary reactions, which can lead to lower selectivity. Therefore, including resistance to mass and heat transfer is essential for a realistic prediction of reactor performance.

While the model equations (11) - (15) still apply, the reaction rates must be calculated using the surface temperature T_s and mole fractions $x_{i,s}$. These values can be found by solving, at each point along the reactor, the following set of algebraic equations [4]:

$$k_{L,i} \cdot A_{cat} \cdot c_T \cdot \left(x_{i,s} - x_{i,L}\right) = \sum \left(v_{i,j} \cdot r_{j,s}\right) \cdot m_{cat} \qquad i = 1, N \qquad (21)$$

$$\sum_{j=1}^{R} r_{j,s} \cdot \left(-\Delta H_{r,j}\right) = k_T \cdot A_{cat} \cdot \left(T_s - T\right) \qquad (22)$$

The mass and heat transfer coefficients in the liquid film around the catalyst are determined from following relationships:

$$Nu = 2 + 0.6 \cdot Re^{0.5} \cdot Pr^{0.33} \qquad (23)$$

$$Sh = 2 + 0.6 \cdot Re^{0.5} \cdot Sc^{0.33} \qquad (24)$$

The physical parameters necessary to calculate the dimensionless numbers were taken from Aspen database. The diffusion coefficient is obtained from the Wilke-Chang equation [5]:

$$D_{AB}\Big/\left[cm^2 s^{-1}\right] = 7.4 \times 10^{-8}\left(\left(\varphi \cdot M_B\right)^{0.5} \cdot \frac{T}{\mu_B \cdot V_{\mu A}{}^{0.6}}\right) \qquad (25)$$

Table 6 presents typical values of the heterogeneous model parameters:

Table 6

Typical values of the heterogeneous model parameters

	IB	DIB	TIB	2BU	1BU
$D_A \cdot 10^5$, cm^2/s	9.9	7.2	5.4	10.9	10.7
k_L, cm/s	0.0095	0.0072	0.0059	0.0096	0.0096
k_T, W/mK			$400 \div 430$		
α_t, kW/m^{2}K			$0.133 \div 0.149$		
U, kW/m^{2}K			$0.116 \div 0.128$		

Fig. 4 shows the reaction extents (left), and the conversion and selectivity profiles (right) along the reactor. Fig. 5 presents the bulk and catalyst surface temperatures (left) and isobutene mole fraction profiles (right). Compared to the pseudo-homogeneous model, the heterogeneous model predicts a much smaller temperature increase. There is a large difference between the isobutene mole fraction in bulk and at the catalyst surface, which leads to a lower conversion and, more important, to a lower selectivity.
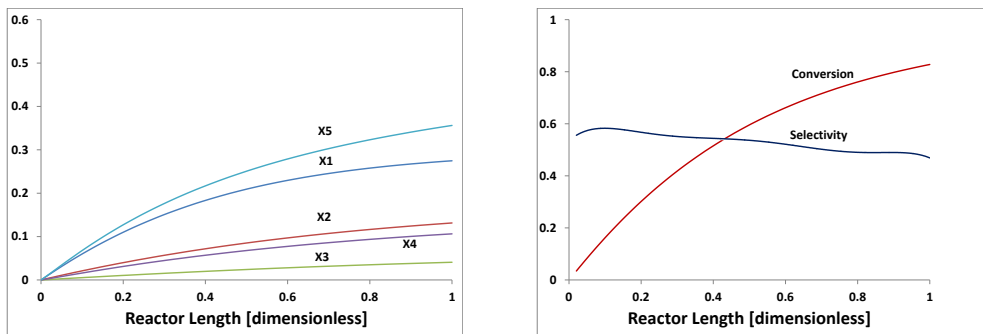
Fig. 4. Profiles along the plug-flow reactor
(left - reaction extents, right - conversion and selectivity).
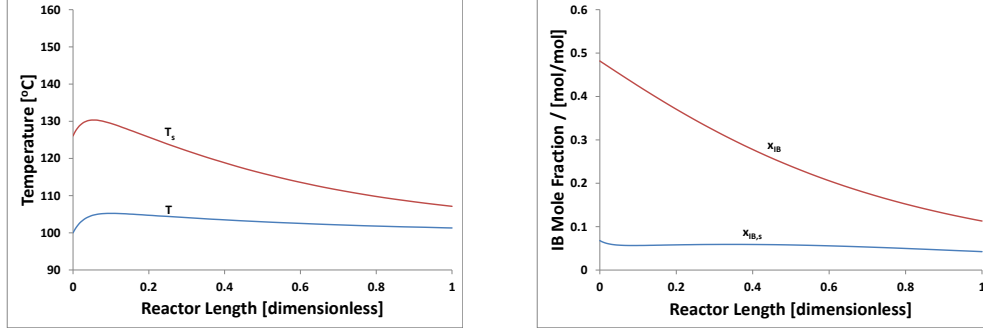
Fig. 5. Profiles along the plug-flow reactor (left - bulk and catalyst surface temperature, right - bulk and catalyst surface IB mole fraction).

6. Discussions

For the purpose of analyzing the influence of heat and mass transfer resistances in the liquid film around the catalyst, two models were investigated: the pseudo-homogeneous model in which the mass and heat transfer resistances between the liquid phase and solid (catalyst) were ignored and the heterogeneous model, in which the rates of mass and heat transfer between the bulk and the catalyst surface were explicitly calculated.

The pseudo-homogeneous model predicted a higher reaction rate. Due to exothermic character of the process, the temperature increased rapidly, reaching the peak around 150°C. Therefore, the conversion of *IB* was almost complete. Moreover, since the formation of *DIB* was favored by high temperature, the selectivity was also high. The heterogeneous model, which accounted for the resistance to mass transfer, predicted a lower *IB* concentration at catalyst surface (Fig. **5.** Profiles along the plug-flow reactor (left - bulk and catalyst surface temperature, right - bulk and catalyst surface IB mole fraction). . right) and therefore a lower reaction rate. Consequently, the *IB* conversion was also lower. Lower reaction rates also determined a lower temperature, which favored the side reactions. Moreover, as the *DIB* product accumulated on the catalyst surface, the rates of the secondary reactions increased with the result of lower selectivity towards C8. Those effects were evident from the plot of effectiveness factors defined, for each reaction, by equation (26) and presented in Fig. 4.

$$\eta_{j} = \frac{r_{j}\left(x_{s}, T_{s}\right)}{r_{j}\left(x, T\right)} \tag{26}$$
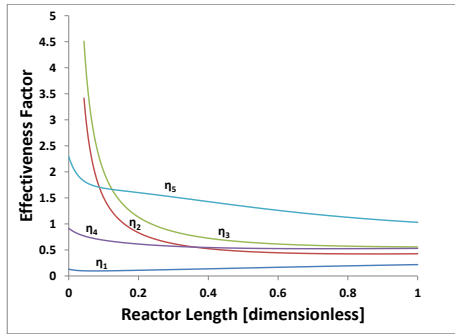
Fig. 4. Effectiveness Factor.

7. Conclusions

High temperature improves *IB* conversion and the selectivity towards C8; the best reactor would be an isothermal PFR operated at the maximum temperature allowed by the catalyst;

The control of temperature below the maximum catalyst allowable temperature is difficult in short tubes reactors (high catalyst density); long tubes reactors, where the catalyst is diluted by a suitable inert, are needed for good temperature control;

There are significant temperature and concentration gradients between the bulk liquid and the catalyst surface;

Low temperature favors the secondary reactions and decreases the selectivity.

8. Nomenclature and Abbreviations

A_{cat} = catalyst area, m^2
c_p = heat capacity, J/(kg·K)
D_A = diffusion coefficient, m^2/s
d_p = catalyst particle diameter, m
E_a = activation energy, J/kmol
ΔH_r = heat of reaction J/kmol
k_0 = pre-exponential factor, kmol/(kg·s)
k_L = mass transfer coefficient, m/s
k_T = heat transfer coefficient, W/(m^2·K)
M = molecular mass, kg/kmol
R = ideal gas constant, J/(kmol·K)
T = temperature, K
u = velocity, m/s
U = overall heat transfer coefficient, W/(m^2·K)
V = reactor volume, m^3
V_μ = molecular volume, m^3/kmol

Greek symbols

ρ = feed density, kg/m^3

ρ_{cat} = bulk catalyst density, kg/m^3

Φ = association parameter

η = effectiveness factor

μ = dynamic viscosity, N·s/m^2

λ = thermal conductivity, W/(m·K)

Dimensionless numbers

$$Re = \frac{\rho \cdot u \cdot d}{\mu}$$ - Reynolds number

$$Nu = \frac{k_T \cdot d_p}{\lambda}$$ - Nusselt number

$$Pr = \frac{c_p \cdot \mu}{\lambda}$$ - Prandtl number

$$Sh = \frac{k_L \cdot d_p}{D_A}$$ - Sherwood number

$$Sc = \frac{\mu}{\rho \cdot D_A}$$ - Schmidt number

REFERENCES

[1] Talwalkar S., Mankar S., Katariya A., Aghalayam P., Ivanova M., Sundmacher K., Mahajani S., Selectivity engineering with reactive distillation for dimerization of C4 Olefins: Experimental and theoretical studies. *Industrial & Engineering Chemistry Research*, 46, (2007), 3024–3034.

[2] Honkela M.L., Krause A.O.I., Kinetic Modeling of the Dimerization of Isobutene. *Industrial & Engineering Chemistry Research*, 43, (2004), 3251–3260.

[3] Talwalkar S., Chauhan M., Aghalayam P., Qi Z., Sundmacher K., Mahajani S., Kinetic Studies on the Dimerization of Isobutene with Ion-Exchange Resin in the Presence of Water as a Selectivity Enhancer. *Industrial & Engineering Chemistry Research*, 45, (2006), 1312–1323.

[4] Levenspiel O., *Chemical Reaction Engineering*. John Wiley & Sons, 1999.

[5] Bratu E.A., *Operatii si Utilaje in Industria Chimica*. Editia II, Editura Tehnică, Bucuresti, 1970.

[6] Dimian A.C., Bîldea C.S., *Chemical Process Design*. Wiley-VCH Verlag GmbH & Co. KGaA, 2008.

Saccharomyces cerevisiae YEAST IMMOBILIZATION IN NATURAL SUPPORT - TESTING IN A REACTOR WITH RECIRCULATION

Ioan CALINESCU, Petre CHIPURICI[*], Bogdan MIRICA, Sorina PRODAN-RADU

Department of Bioresources and Polymer Science, University Politehnica of Bucharest

Abstract

Immobilized yeast in natural supports was evaluated for the production of ethanol using molasses as carbon source in a fixed bed reactor. This paper will focus on marrow stem sunflower and volcanic rock supports.
The activation of the supported yeast before use is of great importance. The natural supports were tested to investigate the immobilization, growth and proliferation of Saccharomyces cerevisiae yeast cells for different periods of activation. For this study gravimetric and scanning electron microscopy methods were used. The activity of the immobilized yeast was tested in a fermentation reactor with recirculation to underline the influence of the molasses concentration over the fermentation process.

Keywords: bioethanol, *Saccharomyces cerevisiae*, yeast immobilization, natural support, marrow stem sunflower, volcanic rock

1. Introduction

Energy has always been the primary resource that people have relied on for survival and it provided us the opportunity to perform productive activities, making industrialization and technological advances of modern society possible [1]. Bioethanol is an important alternative combustible due to its potential to replace the fossil fuels that are limited and soon to be depleted, its use presenting also advantages, the most important of them being of environmental nature: it is biodegradable, nontoxic and it reduces particulate emissions in compression–ignition engines.
During the last few decades the immobilization of the microorganisms used in the fermentation process has been investigated using different natural and synthetic supports. These studies showed improvements in cell concentrations and thereby in reaction rates and productivity, leading to shorter residence time and smaller reactor size.

---

[*]Corresponding author –E-mail address: petre.chipurici@pub.ro (Petre Chipurici)

Most of the natural supports tested in the immobilization processes are lignocellulose materials such as sawdust, wood chips, rice husk, and straw [2]. Finding new, low-cost, abundant and non-destructive immobilization systems that can also be used at an industrial level is of great interest. Agriculture residues are mostly considered due to their availability. Corn cobs, grape pomace [3], sorghum bagasse [2], brewer's spent grains [4], maize stem ground tissue [5] and even shell silk cocoons [6] are some examples of wastes that have been successfully tested nowadays as natural supports.

Other materials that don't present any particular industrial interest such as Kissiris, an inexpensive mineral glass foam derived from lava, are also being used in cell immobilization processes [7].

Due to high concentrations of fermentable sugars (40-60%), molasses, the main by-product from the sugar industry, is a renewable substrate used in the fermentation process and it satisfies 90% of the ethanol production in some countries [5], due to its high availability and low cost.

Saccharomyces cerevisiae is the most common species of yeast used for the bioethanol production, also with a role in wine making, baking and brewing since ancient times [5].

In this present work two natural porous materials, marrow stem sunflower and volcanic rock, were used as supports for the immobilization of *Saccharomyces cerevisiae* yeast in the fermentation process of molasses derived from sugar beet to ethanol.

2. Experimental

2.1. *The immobilization of yeast using natural support*

The marrow stem sunflower (MSS) and volcanic rock (VR) were used as supports for immobilization of the *Saccharomyces cerevisiae* yeast (Ethanol Red from Fermentis, 94-96 % dry weight; $>20\times10^9$ living cells/g).

The volcanic rock support used was procured from the lava fields situated between volcano Laki and town Kirkjubaejarklaustur (Iceland), formed as a result of the volcanic eruption called "Fires Skafta" from 1783.

The natural supports were cut into cubes with the thickness of approximately 5 mm (MSS) and 10 mm (VR), and these were sterilized by boiling for 30 min.

For both types of support the amount of yeast used represented 2% of the support's weight.

For the growth of yeast cells on the support a nutrient standard solution containing molasses (120 g L^{-1}), $(NH4)_2SO_4$ (5 g L^{-1}), KH_2PO_4 (3 g L^{-1}), $MgSO_4\times7H_2O$ (5 g L^{-1}), citric acid (5.4 g L^{-1}) and Na_2HPO_4 (7 g L^{-1}) was used. The molasses had a content of 56.6% fermentable sugars.

The solution was sterilized by reflux for 30 min prior to use.

The immobilization of the yeast was carried out in a thermo shaker at 35°C for 8 h.

The activation of the yeast took place as it follows:

- After the immobilization of the yeast the molasses solution was replaced with fresh solution and the support was left for another 10h at 31-32°C. Again the solution was changed and the yeast was left to activate for another 6h at 35°C under agitation, obtaining a total of 24h of activation (MSS1-24, VR1-24, and VR2-24).
- MSS2-48 / MSS3-48 / VR1-48 / VR2-48: in a similar manner the activation time was 48h (16h at 31-32°C, 8h at 35°C under agitation and another 16h at 31-31°C - the molasses solution being replaced each time).
- MSS2-72 / MSS3-72 / VR1-72: 72h of yeast activation was obtained.
- MSS3-96: the yeast was activated for 96h.

A water jacketed bioreactor with a working volume of 60 mL and a total volume of 70 mL was used for the fermentation. It was comprised of a plug flow glass tubular column (16 mm i.d., 185 mm length).

After sterilization, the thermostated reactor was filled with support containing immobilized yeast and fermentation medium. A micro-dose pump type 335A Unipan was used to transfer the feed medium (45-65 mL) from a cylinder serving as reservoir into the bioreactor. The exhaust gas and effluent solution were removed via an outlet located at the top of the bioreactor. The effluent from the column was recirculated with the micro-dose pump. A glassware device was installed between the column and feed pump to provide a continuous supply for the fermentation. The temperature was kept constant at 35^{0}C by circulating water from the thermostat through the reactor jacket. The CO_2 flow was also measured during the fermentation. The schematic of the experimental setup is shown in fig.1.

2.2. *Bioethanol analysis*

Bioethanol concentration in the fermentation mixture was determined by gas chromatography, after an extraction in dichloromethane, using a HP 6890 chromatograph equipped with flame ionization detector and an Agilent GNW Scientific (30m×0.250 mm×0.5μ, DB1) capillary column. Helium was used as a carrier gas. Pentan-1-ol was used as an internal standard.
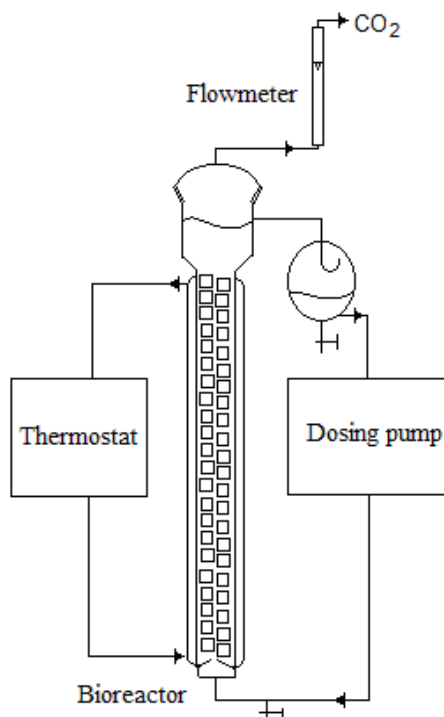
Fig.1. The laboratory setup.

2.3. Textural characterization

For the electronic microscopic scanning (SEM) micrographs, samples were taken consisting of fresh support, sterilized support and after immobilization and activation. The lyophilization step is necessary before performing the scanning electron microscopy analysis. The samples were frozen in a freezer at -20°C for 24h, and then freeze-dried in a Labconco FreeZone freeze-dryer, at 0.470 mBar for 48h. The temperature of the drying chamber was -50°C.

The inner and the outer surfaces of the fresh and immobilized structures with yeast cells were scrutinized by High Resolution Scanning Electron Microscope (HRSEM), FEI Inspect F 50 (field emission gun). A 5kV voltage was used and fracture surfaces were examined after gold sputter coating.

3. Results and discussions

To analyze and compare the experimental results obtained, the average fermentation rates and the average fermentation rates for periods of time were determined (eq. 1, 2). The ethanol concentration was calculated with eq. 3 and the transformation yield of sugars into ethanol were determined (eq.4).

$$Fermentation\_rate_1 = \frac{C_{ethanol}(g/L)}{time(h)} \tag{1}$$

$$Fermentation\_rate_2 = \frac{C_{ethanol_{i+1}}(g/L) - C_{ethanol_i}(g/L)}{t_{i+1} - t_i} \tag{2}$$

$$C_{ethanol}(g/L) = C_{ethanol}(\%) \times \rho_{ethanol} \times 10 \tag{3}$$

$$Yield = \frac{C_{ethanol}(g/L)}{C_{sugars}(g/L) \times 0.5111} \tag{4}$$

Experimental conditions and results are shown in tables 1-5 and figures 2-10.

Table 1

Experimental conditions used for testing the immobilized yeast on natural support and results - the molasses solution used had a concentration of 120g/L, and the volume of the fermentation medium was 45mL

Exp.	Type of support	Time, (h)	$C_{ethanol}$, (%)	*Fermentation_ rate₁*, (g_{EtOH}/L×h)	*Fermentation_ rate₂*, (g_{EtOH}/L×h)
1	MSS1-24	1	1.66	13.09	13.09
		2	1.89	7.44	1.80
		4	3.11	6.14	4.83
		6	3.25	4.28	0.55
2	MSS2-48	1	2.39	18.88	18.88
		2	3.39	13.36	7.84
		3	3.62	9.53	1.86
		3.5	3.71	8.36	1.38
		4	3.80	7.50	1.45
		5	3.67	5.79	-1.05
3	MSS2-72	0.5	1.57	24.83	24.83
		1	1.75	13.79	2.75
		1.5	1.94	10.21	3.06
		2	2.26	8.91	4.98
		3	3.18	8.36	7.26
		4	3.66	7.23	3.84
		5	3.80	6.00	1.10
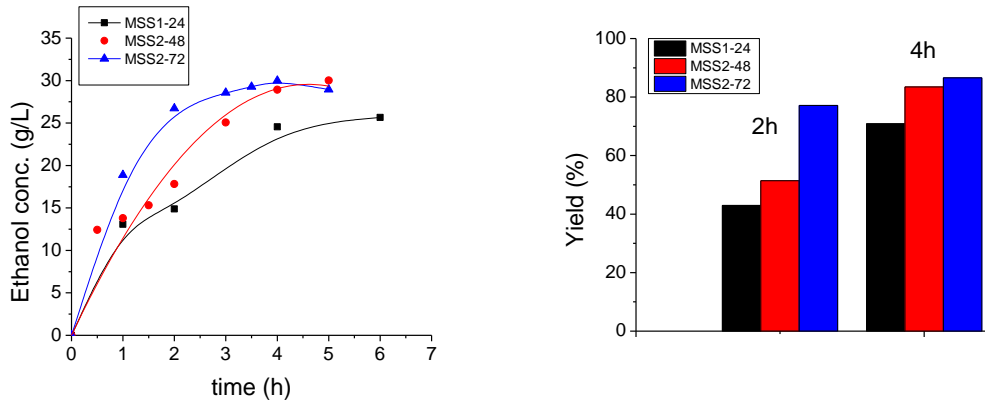
Fig. 2. The ethanol concentration and yield for the yeast immobilized on natural support (MSS1-24, MSS2-48, MSS2-72)

It can be noticed from fig. 2 that for the supports with a longer activation time of the yeast the alcohol concentration increases faster. An increased time of activation for the immobilization of the yeasts on natural support led to an increased yield in ethanol.
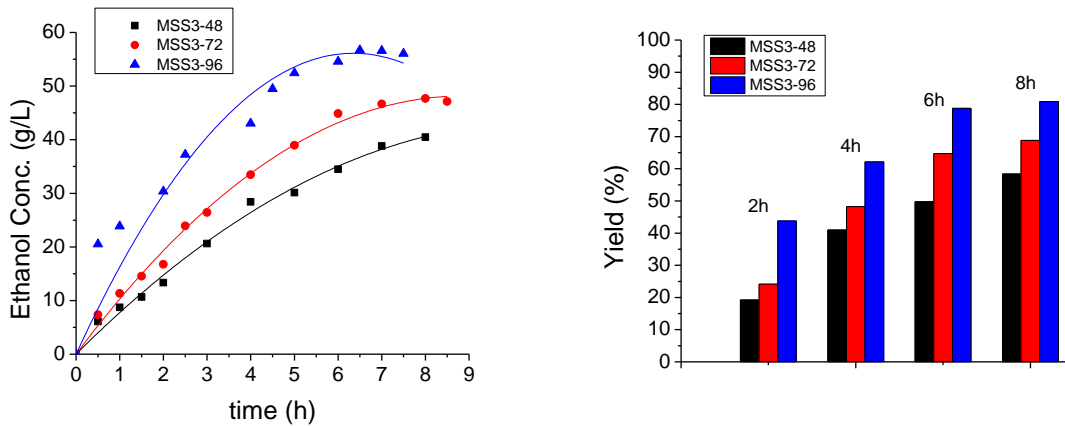
Fig.3. The ethanol concentration and yield for the second set of supports (MSS3-48, MSS3-72 an MSS3-96)

It can be observed from fig. 3 that in the case of MSS3-72 the activation of the yeast for 72h led to an improvement in the fermentation process. The maximum values were obtained between 7 and 8h.
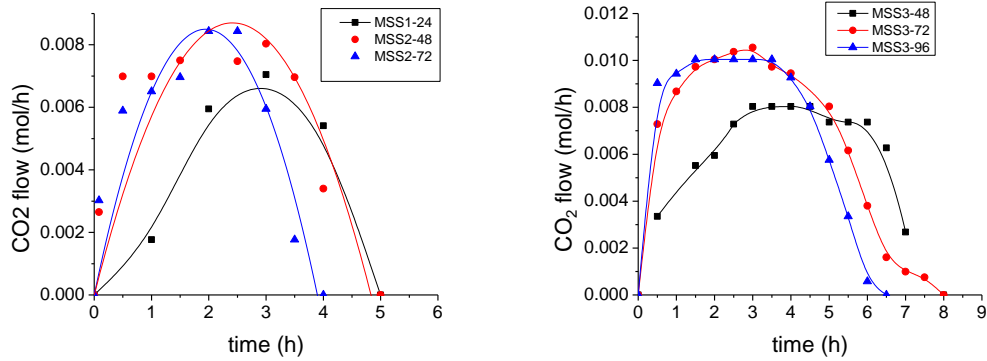
Experimental conditions used for testing the immobilized yeast on MSS3 and results – the solution of molasses that was used had a concentration of 240g/L

Exp.	Type of support	Vol. medium fermentation, (mL)	Time, (h)	$C_{ethanol}$, (%)	Fermentation_ rate$_1$, (g$_{EtOH}$/L×h)	Fermentation_ rate$_2$, (g$_{EtOH}$/L×h)
4	MSS3-48	44	0.5	0.77	12.19	12.19
			1	1.11	8.73	5.27
			1.5	1.35	7.11	3.88
			2	1.69	6.67	5.33
			3	2.62	6.88	7.30
			4	3.60	7.10	7.76
			5	3.82	6.02	1.73
			6	4.37	5.75	4.35
			7	4.92	5.55	4.34
			8	5.13	5.06	1.66
5	MSS3-72	46	0.5	0.93	14.70	14.70
			1	1.43	11.31	7.93
			1.5	1.84	9.70	6.47
			2	2.12	8.38	4.41
			2.5	3.03	9.57	14.35
			3	3.35	8.80	4.97
			4	4.24	8.36	7.04
			5	4.94	7.79	5.51
			6	5.69	7.48	5.90
			7	5.91	6.66	1.78
			8	6.04	5.96	1.03
			8.5	5.97	5.54	-1.11
6	MSS3-96	47	0.5	2.60	41.05	41.05
			1	3.02	23.85	6.66
			2	3.85	15.18	6.50
			3	4.72	12.41	6.88
			4	5.46	10.76	5.81
			4.5	6.27	10.99	12.85
			5	6.65	10.49	5.92
			6	6.92	9.10	2.16
			6.5	7.19	8.72	4.22
			7	7.17	8.08	-0.25
			7.5	7.11	7.48	-1.01

Fig.4. The CO_2 measured flow – MSS

Fig. 4 shows the CO_2 values measured in time, and these can be related with the activity of the yeast and the availability of the substrate. It is obvious that for the supports with 48h and 72h of activation the fermentation is more intense and begins almost instantaneously. The end of CO_2 formation is equivalent to the end of the fermentation process.

The molasses concentration of 240g/L did not inhibit the yeast, the sugars being transformed by the yeast within 8h in the case of MSS3-48, MSS3-72 and within 6.5h in the case of MSS3-96 showing that with the right activation time the productivity of the microorganisms can increase.

Fig.5 The ethanol concentration and yield respectively in time for VR1-24, VR1-48 and VR1-72

Fig. 5 shows the results obtained for VR1-24, VR1-48 and VR1-72. It can be noted that the maximum yield for the support with 24h yeast activation time is 92.2%, for the support with 48h activation time is 90.9% and for the support with

72h of activation time the maximum yield obtained is 99.9% after 4h of fermentation.

Table3

Experimental conditions used for testing the immobilized yeast on VR1 and results - the molasses solution that was used had a concentration of 120 g/L
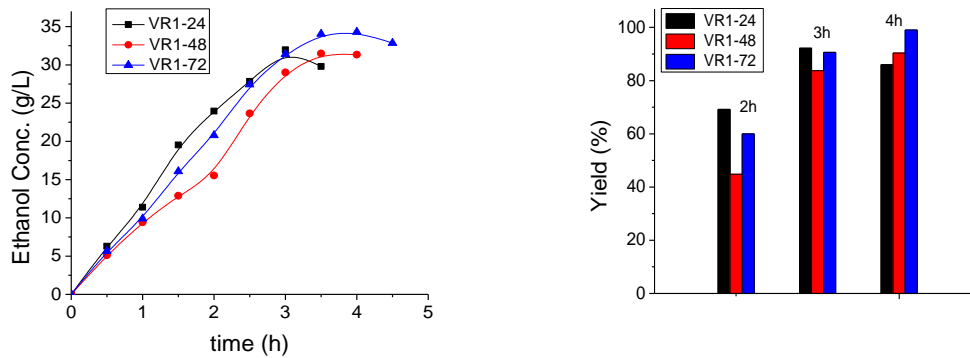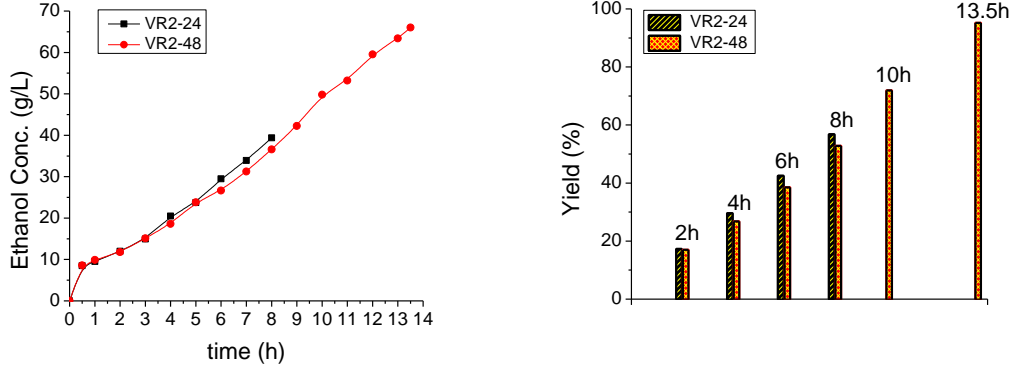
Exp.	Type of support	Vol. medium fermentation, (mL)	Time, (h)	$C_{ethanol}$, (%)	Fermentation_ $rate_1$, (g_{EtOH}/L×h)	Fermentation_ $rate_2$, (g_{EtOH}/L×h)
7	VR1-24	55	0.5	0.80	12.61	12.61
			1	1.44	11.39	10.17
			1.5	2.48	13.03	16.31
			2	3.04	11.98	8.84
			2.5	3.53	11.14	7.76
			3	4.05	10.65	8.24
			3.5	3.78	8.51	-4.32
8	VR1-48	58	0.5	0.65	10.23	10.23
			1	1.19	9.42	8.60
			1.5	1.64	8.60	6.97
			2	1.97	7.77	5.28
			2.5	3.00	9.46	16.22
			3	3.68	9.67	10.73
			3.5	3.99	9.00	4.95
			4	3.97	7.83	-0.32
9	VR1-72	61	0.5	0.72	11.33	22.67
			1	1.26	9.90	8.47
			1.5	2.04	10.73	12.38
			2	2.63	10.39	9.37
			2.5	3.48	10.98	13.32
			3	3.98	10.47	7.94
			3.5	4.32	9.73	5.28
			4	4.35	8.58	0.51
			4.5	4.16	7.30	-2.93

Fig.6. The ethanol concentration and yield for VR2-24 and VR2-48

Fig. 6 shows that for higher concentration of the molasses solution (240g/L) the fermentation process takes much longer, even though satisfactory yields are also obtained, suggesting that the yeast was inhibited by the substrate.
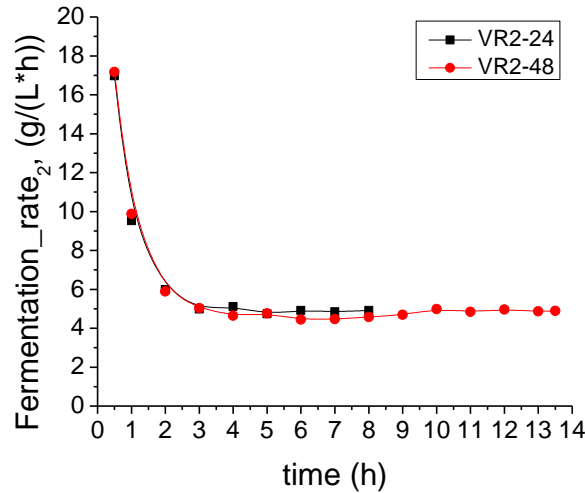
Fig. 7 The medium fermentation rates for VR2-24 and VR2-48

The mean fermentation rates for the supports VR2-24 and VR2-48 are shown in fig. 7. In both cases a maximum was obtained at the beginning of the fermentation process but afterward a sudden drop was recorded followed by stabilization due to the metabolism regulation of the yeast that depends on its ability to adapt to the environment conditions.
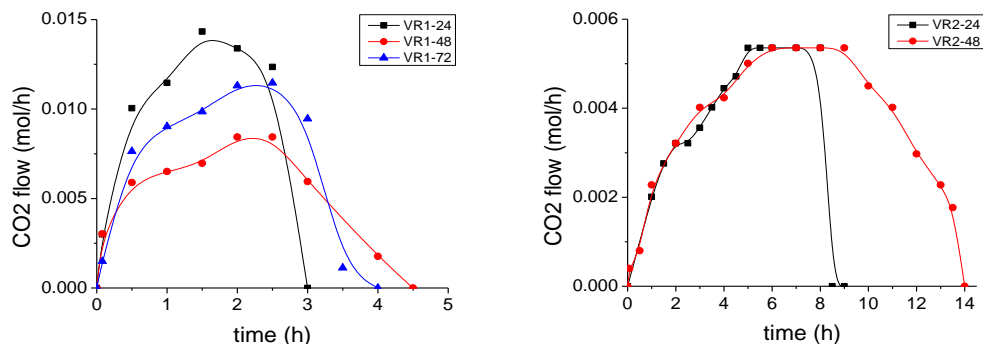
Fig. 8. The CO_2 flow rates for VR

Fig.8. shows the CO_2 flow rates for the VR supports suggesting how the sugar content of the molasses was transformed by the yeast at different activation times.

Table 4

Experimental conditions used for testing the immobilized yeast on VR2 and results - the molasses solution concentration was 240g/L and the fermentation medium volume was 61mL

Exp.	Type of support	Time, (h)	$C_{ethanol}$, (%)	Fermentation _ rate$_1$, (g_{EtOH}/L×h)	Fermentation _ rate$_2$, (g_{EtOH}/L×h)
10	VR2-24	0.5	1.08	16.97	16.97
		1	1.21	9.53	2.09
		2	1.52	5.98	2.44
		3	1.89	4.98	2.97
		4	2.60	5.12	5.54
		5	3.01	4.74	3.24
		6	3.74	4.91	5.76
		7	4.30	4.85	4.43
		8	4.99	4.92	5.45
11	VR2-48	0.5	1.09	17.17	17.17
		1	1.25	9.88	2.59
		2	1.49	5.89	1.89
		3	1.91	5.03	3.32
		4	2.36	4.65	3.51
		5	3.02	4.76	5.21
		6	3.38	4.44	2.85
		7	3.96	4.47	4.60
		8	4.63	4.57	5.31
		9	5.35	4.69	5.68
		10	6.31	4.98	7.56

## *Gravimetric study of the yeast activation on the MSS support*

The yeast activation was gravimetrically studied in order to determine the growth rate. Four samples were prepared, each containing 5 cubes of 5mm thickness. Probe 1 consisted of fresh support, probe 2 consisted of sterilized support, probe 3 consisted of sterilized support with 24h activated yeast (0.1g yeast and 12mL molasses solution of 120g/L concentration were used) and probe 4 was prepared in the same conditions as probe 3, but with an activation time of 48h. These were then freeze-dried and weighted. The results are presented in Table 5.

Table 5

The gain in weight of the supports due to yeast activation

Probe	Initial weight (g)	Final weight (g)	Difference in weight	
			(g)	(%)
1	0.023	0.021	-	-
2	0.023	0.0194	-0.0036	-15.65%
3	0.023	0.0493	0.0227[*]	98.69%[*]
4	0.023	0.0743	0.0477[*]	207.39%[*]

[*]the values were calculated taking into account the weight loss caused by the sterilization process
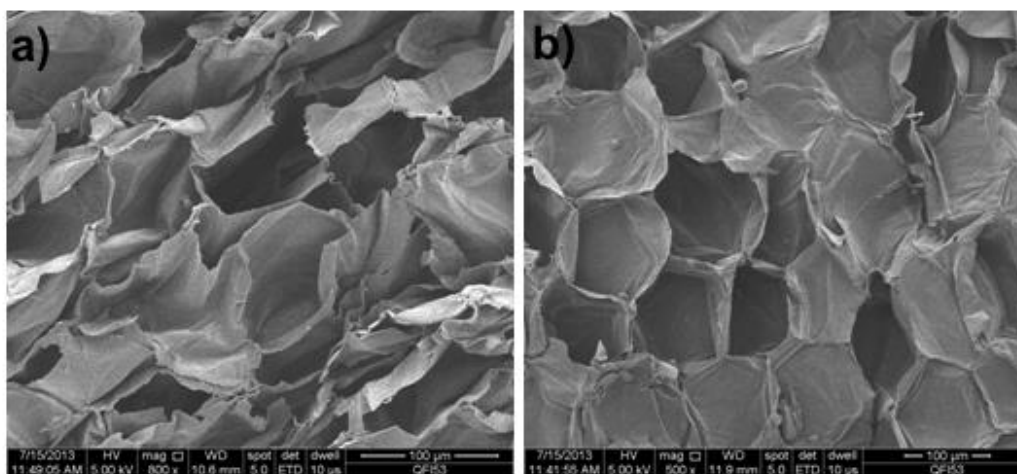
Fig. 9. SEM images of the fresh support MSS (a) surface and (b) cross-section

Saccharomyces cerevisiae yeast immobilization in natural support - testing in a reactor with recirculation
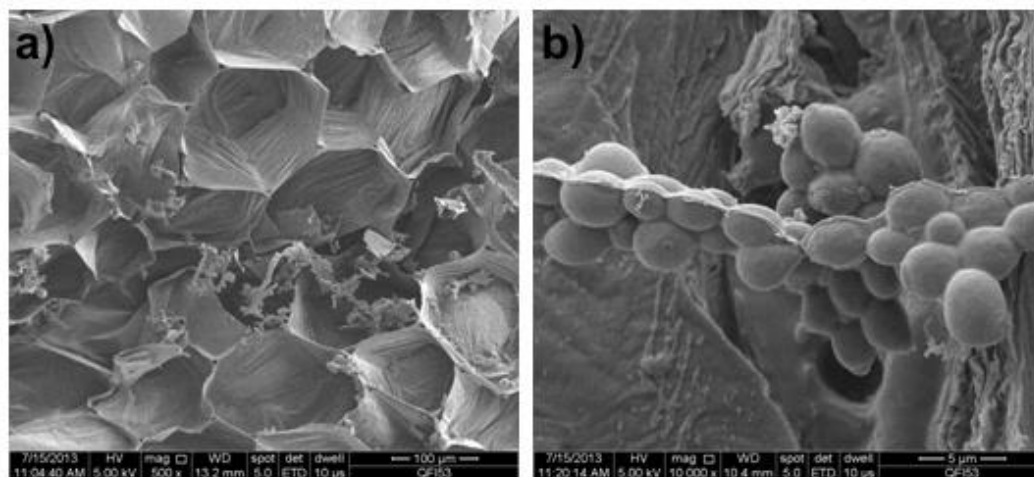
Fig. 10. SEM cross-section images of the structures on which yeast developed for 48 h

Fig. 9 shows that the MSS fresh structure has uniform pores with an average pore diameter of 100 µm. Cross section images of the MSS structure after 48 h incubation time show cell growth inside these pores (fig.10).

6. Conclusions

➢ The immobilization of the yeast *Saccharomyces cerevisiae* on marrow stem sunflower and volcanic rock supports was efficient due to their internal structures and high porosity.
➢ Both supports can be reused in several fermentation processes.
➢ The yeast maintains its grip on the natural support showing activity over a long period of time. The activation time of the yeast has a great importance in the fermentation process. Higher concentrations of ethanol were obtained when the yeast was allowed to grow for more than a day.
➢ In the case of the volcanic rock supports, increasing the concentration of the molasses solution led to the inhibition of the yeast and thus a longer fermentation time.

REFERENCES

[1] Olsen H. S., Rosgaard L., Johansen K. S., Schagerlöf U., Kaasgaard S. G., Bioethanol and Green Energy. Bioethanol- a description of 1st and 2nd generation processes, *Bioscience Explained*, 4(2), (2008), 1–2.

[2] J. Yu, X. Zhang, T. Tan, An novel immobilization method of *Saccharomyces cerevisiae* to sorghum bagasse for ethanol production, *Journal of Biotechnology*, 129, (2007), 415–417.

[3] Genisheva Z., Mussatto S. I., Oliveira J. M., Teixeira J. A., Evaluating the potential of wine-making residues and corn cobs as support materials for cell immobilization for ethanol production, *Industrial Crops and Products*, 34(1), (2011), 979–982.

[4] Kopsahelis N., Bosnea L., Bekatorou A., Tzia C., Kanellaki M., Alcohol production from sterilized and non-sterilized molasses by *Saccharomyces cerevisiae* immobilized on brewer's spent grains in two types of continuous bioreactor systems, *Biomass and Bioenergy*, 45, (2012) 86-87.

[5] R. Razmovski, V. Vučurovic, Bioethanol production from sugar beet molasses and thick juice using *Saccharomyces cerevisiae* immobilized on maize stem ground tissue, *Fuel*, 92, (2012), 1–2.

[6] Rattanapan A., Limtong S., Phisalaphong M., Ethanol production by repeated batch and continuous fermentations of blackstrap molasses using immobilized yeast cells on thin-shell silk cocoons, *Applied Energy*, 88, (2011), 4400–4402.

[7] Nigam P., Banat I.M., Singh D., A.P. McHale, R. Marchant, Continuous ethanol production by thermotolerant Kluyveromyces marxianus IMB3 immobilized on mineral Kissiris at 45 °C, *World Journal of Microbiology & Biotechnology*, 13, (1997), 283-284.

MATHEMATICAL MODELING OF ANAEROBIC DIGESTORS FOR BIOGAS PRODUCTION PLANTS

Paul S. AGACHI[1], Mircea CRISTEA[1], Cecilia ROMAN[2], Abhilash NAIR[3], Alexandrina ZUZA[1*], Marius BREHAR[4]

[1] Chemical Engineering Department, Babes-Bolyai University, Cluj-Napoca, Romania
[2] Research Institute for Analytical Instrumentation, Cluj-Napoca
[3] Erasmus Mundus Program, India
[4] Compania de Apă Someş SA, Cluj-Napoca, Romania

Abstract

This paper summarizes the most important aspects in developing a mathematical model of anaerobic digestion process with applications for biogas production plants, along with the most fundamental and representative already existing generic models. The most significant mathematical models of anaerobic digestion are reviewed. It also identifies the critical stoichiometric parameters that have been varied in order to fit the model at an industrial scale reactor. The paper also enumerates the sequential order in which the parameters have to be varied to obtain an accurate data fit. Application of the model needs to be further researched and evaluated in the future, as to optimize and enhance design and operation of wastewater treatment plants.

Keywords: mathematical models, ADM1 model, plants, waste activated sludge, anaerobic digestion, biogas

1. Introduction

Anaerobic digestion has become an increasingly important industrial process. It has been used for many years to treat and sanitize sewage sludge waste from municipal wastewater and industrial wastewater, reduce its odor and volume, and produce useful biogas [1]. Because of its complex nature, the optimization and further process development of this technology go hand in hand with the availability of mathematical models for both simulation and control purposes [2]. Anaerobic digestion is a subject of intensive research, specifically focused on novel digester design, substrate pretreatment to improve the biodegradability of the biomass, hence enhancing the biogas production and upgrading of the biogas. Also, only recently developed advanced culture independent molecular techniques

---

[*]Coressponding author–E-mail address: alexandrinazuza@chem.ubb.cluj.ro (A. Zuza)

for identification of the microbial communities have paved the way for obtaining more fundamental insights in the process [3,4].

2. Conversion processes in anaerobic digestion

The metabolic pathway and process microbiology of anaerobic digestion is shown in Fig. 1. Generally, the anaerobic digestion process consists of four stages; the first one is called hydrolysis, consisting in the transformation of complex organic matter such as proteins, carbohydrates and lipids into simple soluble products like sugars, LCFA, AA and glycerin. In the second step, called the acidogenic stage fermentative bacteria use the hydrolysis products to form intermediate compounds like organic acids, leading to volatile fatty acids (VFAs, including acetic, butyric, propionic and valeric acid). These VFA along with ethanol are converted to acetic acid, hydrogen and carbon dioxide. Finally, in the fourth stage, both acetic acid and hydrogen are the raw material for the growth of methanogenic bacteria, converting acetic acid and hydrogen to biogas composed mainly of methane, carbon dioxide and hydrogen sulfide [5]. The resulting biogas composition depends on several factors: (I) the oxidation state of carbon in the substrate, (II) the residence time, (III) the reactor set-up and (IV) the temperature [6].
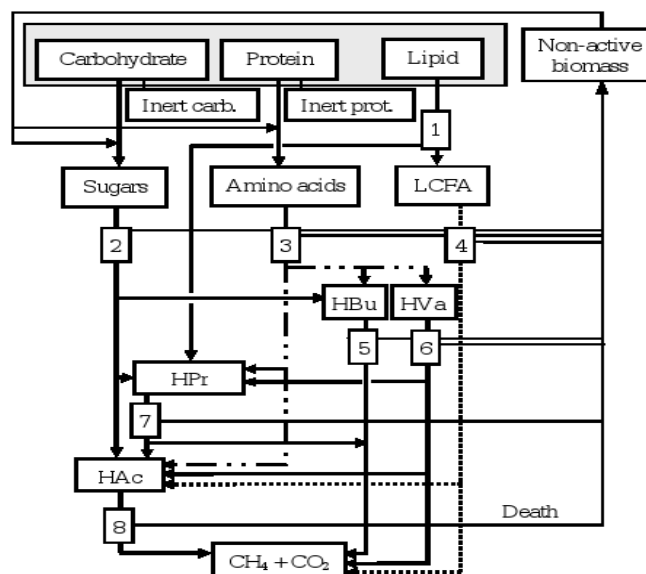
Fig. 1. Conceptual model for ADM1 of the biochemical conversion processes:

1) LCFA and HPr from Lipids; 2)Acidogenesis from Amino Acids; 3)Acetogenesis from Long Chain Fatty Acids; 4)Acedogenesis from Propionate; 5)Acedogenesis from Butyrate and Valerate; 6)AceticlasticMethanogenesis; 7)Hydrogenotrophic Methanogenesis; 8) Methane and carbon dioxide production [5].

3. ADM1 model description

Anaerobic digestion models

The first anaerobic digestion models date back to the mid-sixtieswith the model proposed by Andrews and Pearson [7]. The substrateof the digestion was assumed to consist of dissolved organicsubstances, which were converted to methane by microbialacidogenesis and acetoclasticmethanogenesis. Because the latter is rate-limiting for solutes, several models have been developed, that estimate biogas production using only the methanogenesis step[8,9]. Denac et al. [10] extended these models by including acetogenesis for the conversion of propionate into acetate. The kinetics of these steps is traditionally expressed by Monod type kinetics, which considers a single growth-limiting substrate (Eq.1):

$$\mu = \mu_{max} \frac{[S]}{[S] + K_S} \tag{1}$$

with μ (d^{-1}) the specific growth rate, μ_{max} (d^{-1}) the maximum specific growth rate, [S] (g L^{-1}) the substrate concentration, and K$_S$ (g L^{-1}) the substrate saturation constant (i.e. substrate concentration at half μ_{max}). It was found, however, that the acetoclastic methanogenesis step exhibited inhibition at high concentration of acetate [8]. Accordingly, a kinetic equation was proposed, based on Haldane kinetics (Eq. 2) as given in Eq. 3. The latter is sometimes referred to as "Andrews's kinetics" [11],

$$\mu = \frac{\mu_{max}}{1 + \frac{K_S}{[S]} + \frac{[S]}{K_l}} \tag{2}$$

$$\mu = \frac{\mu_{max}}{1 + \frac{K_S}{[S]} + \frac{[VFA]}{K_l}} \tag{3}$$

where [VFA] (g L^{-1}) is the unionized VFA concentration, and K_l (g L^{-1}) the inhibition constant. As knowledge of anaerobic digestion has increased, it has been clear that a range of factors can influence digestion efficiency, such as digester overloading or the occurrence of toxic components such as sulphide, ammonia or heavy metals [12]. The inhibition effects on the process are included in more recent models. Sanders et al. [13] proposed a surface-based kinetic expression, describing the coverage of particles with bacteria that secrete hydrolytic exo-enzymes. With this the hydrolysis constant per unit area remains constant in order to account for the variable concentrations of enzyme (Eq. 4).

$$\mu = k_{SBK} A \tag{4}$$

According to Vavilin et al. [14], hydrolysis is a two phase process. In the first phase the particulates are colonized by bacteria, which subsequently excrete the hydrolytic enzymes. When a surface is covered with bacteria, it degrades at a constant depth, per unit of time. This type of behavior can be modeled effectively employing Contois-kinetics (Eq. 5).

$$\mu = \mu_{max} X \frac{[S]}{K_S[X] + [S]} \tag{5}$$

The modeling of anaerobic wastewater treatment closely follows the evolution of the models that describe the digestion of dissolved organics and particulates. However, it became necessary to distinguish between the substrate components (carbohydrates, proteins and lipids) fed to the digester. In previous models these were lumped together and simply expressed as the COD. Each particulate type is then described by their specific kinetics and stoichiometry[15,16,17]. Although the feed is considered liquid, suspended particulates are included, with accompanying hydrolysis kinetics. For readily degradable substrates (monosaccharide rich water), lactic acid may be generated and is therefore included in some models [18]. Pavlostathis and Gosset [19] included a cell death/lysis step prior to hydrolysis. Eastman and Ferguson [20] model accounted that during digestion of sludge hydrolysis/cell death and lysis are the rate-limiting steps for methane production. Shimizu et al. [21] included nucleic acids as a variable. The model that specifically addresses the digestion of wastewaters is reviewed by Batstone et al. [22].

ADM1

The ADM1 is a structured, mathematical model based on COD as a common base unit in wastewater characterization. It describes the anaerobic digestion process in a batch as well as a continuous-flow stirred tank reactor. Biochemical processes included in the ADM1 are the disintegration of composites, hydrolysis of particulate COD, such as carbohydrates, proteins and lipids, six substrate degradation processes together with their six specific biomass growth and decay processes [23].

Table1

List of mechanistically inspired models including intermediate components (COMP), hydrolysis kinetics (HYDR), acidogenesis kinetics (ACID) acetogenesis kinetics (ACET), or VFA (VFA ACET), methanogenesis kinetics (METH), either acetogenotrophic (ACET METH) or hydrogenotrophic (HYDMETH), Specific characteristics and field of application. Other abbreviations: Acetic acid (C_2), Propionic acid (C_3), Butyric acid (C_4), Valeric acid (C_5), Caproic acid (C_6), Monod kinetics (M), 1st order kinetics (1st), Acetate (AC), Propionate (PA), Carbohydrates (CH), Lipids (LI) [2]

Authors	Comp	Hydrolysis	Acid	ACET.	METH	Specific characteristics	Application
Andrews and Pearson	C_2	-	M	88 VFA	(ACET METH) M	Yield and kinetics estimated from steady-state condition	Dissolved organics
Eastman and Ferguson	-	1st	-	-	(ACET METH) M	Hydr rate-limiting. No distinction in fermentation products, i.e. the final product is total COD originating from acids, CH_4, CO_2, proteins	Particulate
Denac et a.l	C_2-C_4	-	M	M (VFA)	(ACET METH) M	Biofilm diffusion model	Dissolved organics
Costello et al.	C_2-C_4 Lactic acid, CH, PROT, LI	- 4/3st order (enzyme concentration)	M(pH, H_2, AC)	M(pH,H_2,AC)	M(pH, H_2, AC)	Acid production stoichiometry is hydrogen regulated and inhibited. Hydrolysis by soluble enzymes	Wastewater
Shimizu et al.	C_2-C_6, CH, NA, LI,	1st	1st	1st	1st (ACET METH) 1st (HYD METH)	Separate decomposition kinetics of different VFA. Nucleic acid degradation	Sludge
Batstone et al.	C_2-C_5 Lactic acid, CH, PROT, LI	4/3st order	M(pH, H_2)	M(pH)	M(pH)(ACET METH) M(pH) (HYD METH	Hydrolysis by soluble enzymes. Acid production stoichiometry is hydrogen regulated and inhibited.	Sludge
Vavilin et al.	C_2-C_3	Limited 1st or M	-	M(NH_3,pH, PA)	M(NH_3,pH,H_2S, PA)	SO_4^{2-} reduction to H_2S by consumption of C_2 and C_3 (M). Phosphorous (PO_4^{3-}). Non-degradable solids Minerals (Ca^{2+}, Na^+)	Various
Pavlostathis and Gosset	C_2	1st	M	-	M(ACET METH)	Viable cells/lyse (1st order) into an intermediate particulate requiring hydrolysis	Sludge

Dynamic state variables

The model consists of 32 dynamic state concentration variables and involves19 biochemical rate processes, three gas–liquid transfer processes andadditionally 6 acid–base kinetic processes. In order to characterize the acid–base dissociation in aquatic systems, the dynamic states for VFAs, inorganic carbon (IC) and inorganic nitrogen (IN) are split into two components each.

Rate equation matrix

Appendix 1 shows the 32 state variables structured in the modified process rate and stoichiometric matrix for biochemical and acid/baseequilibria reactions.

Calculation of the derivatives

The calculation of the state variables in a continuous stirred tank reactor is shown in Eq. 6 provided that the bulk volume (V_{liq}) in the reactor remains constant.

$$\frac{dS_{liq,i}}{dt} = \frac{qS_{in,i}}{V_{liq}} - \frac{qS_{liq,i}}{V_{liq}} + \frac{dS_{liq,i}}{V_{liq}} + \sum_{j=1-19} \rho_j v_{i,j} \tag{6}$$

Where the term $\sum_{j=1-19} \rho_j v_{i,j}$ is the sum of the specific kinetic rates for process j, multiplied by the stoichiometric coefficient $v_{i,j}$, q is the volumetric flow rate (see Appendix 1) [23].

4. Modifying reaction parameters to fit industrial data

The kinetic parameters in the ADM1 model have been obtained by lab scale experiments the ADM1 model has also been tested to give acceptable results for pilot scale operations. The model can also be applied to an industrial scale with minor modifications in either the kinetic or stoichiometric parameters. It is important to perform a sensitivity analysis of these parameters on the biogas production as well as methane concentration. The kinetic parameters showed minor variation in the biogas production rate and methane concentration, the stoichiometric parameters are considered to vary largely with the scale of production and the difference in feedstock composition. Hence these values have to be adjusted to fit in an industrial scale.

The stoichiometric parameter is classified into three groups, to identify the sensitivity of these parameters to variation in processes and types of substrates. The group with the highest sensitivity is taken up first and the parameters are

sorted in a descending order of their sensitivity. Each stoichiometric parameter is varied as within the acceptable range and the biogas flow rate and the methane concentration in the biogas has been recorded.

List of Stoichiometric Parameters

Parameter Description	Symbol	Hydrolysis	Acid
Soluble inert from Composites	$f_{sI,xc}$	0.1	0.7-1.2
Carbohydrates from Composites	$f_{ch.xc}$	0.2	0.16-0.23
Proteins from Composites	$f_{pr,xc}$	0.2	0.16-0.23
Lipids from Composites	$f_{li,xc}$	0.25	0.20-0.30
Nitrogen content of Composites	N_{xc}	0.002	0.0015-0.0023

Most of the industrial anaerobic digesters work on continuous mode. The continuous stirred tank reactor (CSTR) model would be the best configuration to model them. A mathematical model has been developed in Simulink to model the reactor in CSTR configuration. The percentage change in the concentrations of methane and the total flow rate of biogas has been presented to analyze the sensitivity of each parameter.
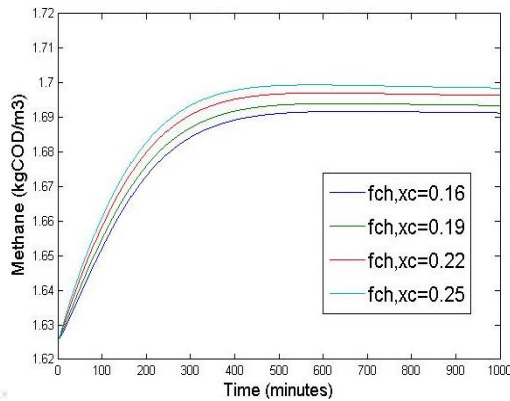
Fig 2. Effects of Carbohydrate yield on methane
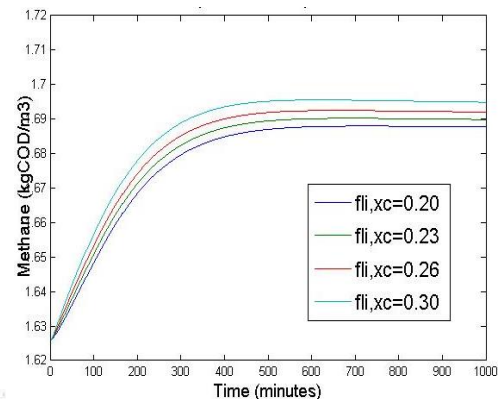
Fig 3. Effects of Lipids yield on methane

47
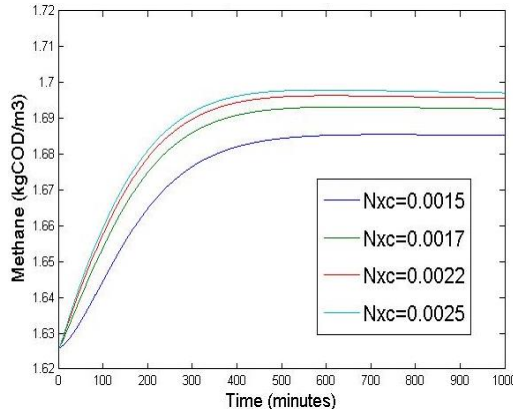
Fig. 4. Effects of Nitrogen yield on methane

Fig. 5. Effects of Protein yield on methane

Fig. 6. Effects of Inhibitors yield on methane
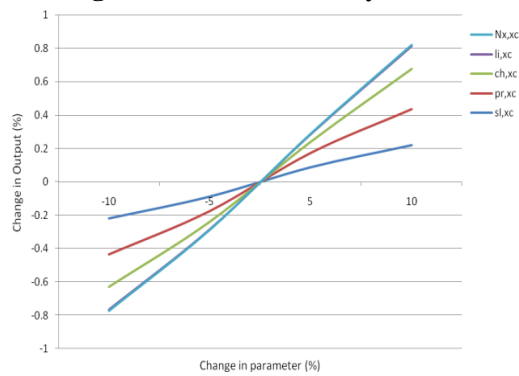
Fig. 7. Parameter Sensitivity chart

5. Discussions

Simulations have shown that there is not much of a difference in the biogas generation rate with the change in the selected stoichiometric parameters, but the concentration of methane gas showed significant variation with the change in the stoichiometric parameters. The Fig.2 to Fig.6 clearly shows this var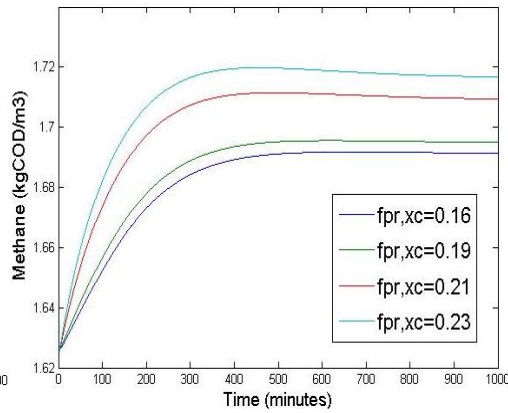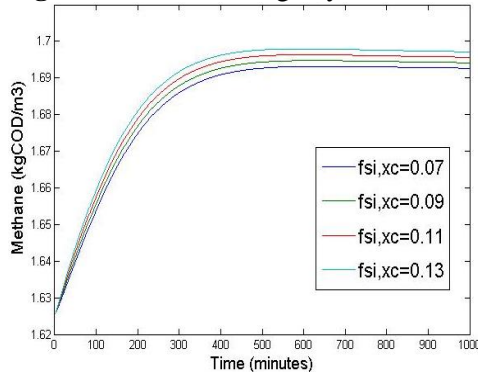iation with time. To have a better understanding of this variation the final steady state value have been recorded and presented in Fig 7. The slope of each line provides the quantitative value of parameter sensitivity. The plot clearly indicates that each of these parameters has a different percentage variation for the same percentage change in the input concentration. The exact percentage of change has been presented in the Fig. 7.

From the results of the simulations, it is clear that the maximum deviation in the output is shown by the variation in the stoichiometric ratios of nitrogen and protein, followed by carbohydrates and lipids and the least with the inhibitor concentration. This priority order can help us gain an important insight on the extent and order of change made to fit the ADM1 model to the industrial data.

6. Conclusions

Optimizing the industrial process and providing an effective control strategy is the key factor of economical generation of biogas. The ADM1 with a minor change in parameters can accurately fit the industrial data. By generating the sensitivity plot for the variation in stoichiometric parameters, we have a clear understanding of its effects in methane concentration. The simulation results provide us a sequential order for the parameters to be varied to fit the model to the industrial data. The sensitivity study showed the flowing priority order $f_{li,xc}$, N_{xc}, $f_{ch,xc}$, $f_{pr,xc}$, $f_{sI,xc}$. After the successful generation of a mathematical model, it is possible to proceed to the next step in optimizing the process and also develop a control strategy for the digesters.

REFERENCES

[1]. Yu L, Wensel PC, Ma J, Chen S,Mathematical Modeling in Anaerobic Digestion (AD), *Journal of Bioremediation and Biodegradation*, 4(3), (2013) 1–4.

[2]. Lauwers J., et al, Mathematical modelling of anaerobic digestion of biomass and waste: Power and limitations, *Progress in Energy and Combustion Science*, 39, (2013) 382–402.

[3]. Lier J., High-rate anaerobic wastewater treatment: diversifying from end-of-the-pipe treatment to resource-oriented conversion techniques. *Water Science Technology*, 57(8), (2008) 1137–1138.

[4]. Talbot G, Topp E, Palina M, Massé D., Evaluation of molecular methods used for establishing the interactions and functions of microorganisms in anaerobic bioreactors, Water Resources, 42(3), (2008), 513–537.

[5]. Khanal S. H.,Anaerobic Biotechnology for Bioenergy Production, Wiley-Blackwell, (2009).

[6]. Deublein D, SteinhauserA., Biogas from waste and renewable resources. An introduction,Weinheim: Wiley-VCH Verlag GmbH and Co., (2009).

[7]. Andrews J, Pearson E.A,.Kinetics and characteristics of volatile fatty acid production in anaerobic fermentation processes, *International Journal of Air and Water Pollution*, 9,(1965) 439–461.

[8]. Andrews J., Dynamic model of the anaerobic digestion model, *Journal of Sanitary Engineering Division Process of the American Society of Civil Engineering*, 1, (1969) 95–116.

[9]. Andrews J, Graef S., Dynamic modeling and simulation of the anaerobic digestion process, *Advanced Chemistry*, 105, (1971),126–162.

[10]. Denac M, Miguel A, Dunn I., Modeling dynamic experiments on the anaerobic degradation of molasses wastewater, *Biotechnology Bioengineering*, 31(1), (1988), 1–10.

[11]. Lyberatos G, Skiadas I., Modelling of anaerobic digestion, *Global Nest Journal*, 18(1), (1999), 63–76.

[12]. Duarte A, Anderson G., Inhibition modelling in anaerobic digestion, *Water Science Technology*, 7(14), (1982), 746–763.

[13]. Sanders W, Geerink M, Zeeman G, Lettinga G., Anaerobic hydrolysis kinetics of particulate substrates, *Water ScienceTechnolgy*, 41(3), (2000),17–24.

[14]. Vavilin V, Fernandez B, Palatsi J, Flotats X,. Hydrolysis kinetics in anaerobicdegradation of particulate organic material: an overview, *Waste Management*, 28(6), (2008), 939–951.

[15]. Costello D, Greenfield P, Lee P., Dynamic modeling of a single-stage high-rateanaerobic reactor : model derivation, *Water Resources*, 25(7), (1991), 847–858.

[16]. Batstone D, Keller J, Newell B, Newland M., Modelling anaerobic degradationof complex wastewater : model development, *Bioresources Technology*, 75(1), (2000), 67–74.

[17]. Batstone D, Keller J, Newell B, Newland M., Anaerobic degradation of complex wastewater: parameter estimation and validation using slaughter house effluent, *Bioresources Technology*, 75, (2000), 75–85.

[18]. Costello D, Greenfield P, Lee P., Dynamic modelling of a single-stage high-rate anaerobic reactor. Model verification, *Water Resource*, 25(7), (1991), 859–871.

[19]. Pavlostathis S, Giraldo-Gomez E., Kinetics of anaerobic treatment, *Water Science Technology*, 24 (8), (1991), 35–39.

[20]. Eastman J, Ferguson J., Solubilization of particulate organic carbon during the acid phase of anaerobic digestion, *Journal of Water Pollution*, 53(3), (1981), 352–366.

[21]. Shimizu T, Kudo K, Nasu Y,. Anaerobic waste-activated sludge digestion e abio conversion mechanism and kinetic model, *Biotechnology Bioengineering*, 41(11), (1993) 1082–1091.

[22]. Batstone D.,Mathetmaical modelling of anaerobic reactors treating domestic wastewater: rational criteria for model use, Review *Environmental Science Biotechnolgy*, 5, (2006), 57–61.

[23]. Blumensaaft F., Keller J., Modelling of two-stage anaerobic digestion using the IWA Anaerobic Digestion Model No. 1 (ADM1), *Water Research*, 39, (2005), 171–183.

[24]. Ficara E., et al, Anaerobic Digestion Models: a Comparative Study, Mathematical Modelling, 7(1), (2012), 1052–1057.

Appendix 1

Biochemical rate coefficients and kinetic rate equations [23]

Component →	1 S_{su}	2 S_{aa}	3 S_{fa}	4 S_{va}	5 S_{va}	6 S_{bu}	7 S_{bu}	8 S_{pro}	9 S_{pro}	10 S_{ac}	11 S_{ac}	12 S_{h2}	13 S_{ch4}	14 S_{co2}	15 S_{hco3}	Rate (ρ_j, kg COD m^{-3} d^{-1})
Process ↓	Monosaccharides (kg COD m^{-3})	Amino Acids (kg COD m^{-3})	L. chain fatty acids (kg COD m^{-3})	Valeric Acid (kg COD m^{-3})	Valerate (kg COD m^{-3})	Butyric Acid (kg COD m^{-3})	Butyrate (kg COD m^{-3})	Propionic Acid (kg COD m^{-3})	Propionate (kg COD m^{-3})	Acetic Acid (kg COD m^{-3})	Acetate (kg COD m^{-3})	Dissolved Hydrogen gas (kg COD m^{-3})	Dissolved Methane gas (kg COD m^{-3})	Dissolved Carbon-Dioxide (kg-mole C m^{-3})	Bicarbonate (kg-mole C m^{-3})	

(The full matrix is a rotated ADM1 Petersen-matrix of biochemical rate coefficients and kinetic rate equations; individual process rows include Disintegration, Hydrolysis of Carbohydrates, Hydrolysis of Proteins, Hydrolysis of Lipids, Uptake of Sugars, Uptake of Amino Acids, Uptake of LCFA, Uptake of Valerate, Uptake of Butyrate, Uptake of Propionate, Uptake of Acetate, Uptake of Hydrogen, Decay of biomass fractions, and Acid–Base processes.)

Inhibition factors:

$I_1 = I_{pH,aa} \cdot I_{IN,lim}$

$I_2 = I_{pH,aa} \cdot I_{IN,lim} \cdot I_{h2,fa}$

$I_3 = I_{pH,aa} \cdot I_{IN,lim} \cdot I_{h2,c4}$

$I_4 = I_{pH,aa} \cdot I_{IN,lim} \cdot I_{h2,pro}$

Appendix 1

Continued

Component → / Process ↓	i	16 Inorganic nitrogen (kg-mole N m⁻³) S_{IN}	17 Ammonia (kg-mole N m⁻³) S_{NH_3}	18 Soluble inerts (kg COD m⁻³) S_I	19 Composites (kg COD m⁻³) X_c	20 Carbohydrates (kg COD m⁻³) X_{ch}	21 Proteins (kg COD m⁻³) X_{pr}	22 Lipids (kg COD m⁻³) X_{li}	23 Sugar degraders (kg COD m⁻³) X_{su}	24 Amino acid degraders (kg COD m⁻³) X_{aa}	25 LCFA degraders (kg COD m⁻³) X_{fa}	26 Valerate and butyrate degraders (kg COD m⁻³) X_{c4}	27 Propionate degraders (kg COD m⁻³) X_{pro}	28 Acetate degraders (kg COD m⁻³) X_{ac}	29 Hydrogen degraders (kg COD m⁻³) X_{h2}	30 Particulate inerts (kg COD m⁻³) X_I	31 Cations (kg-mole m⁻³) S_{cat}	32 Anions (kg-mole m⁻³) S_{an}	Rate (ρ_j kg COD m⁻³ d⁻¹)
1 Disintegration		S_{IN}		$f_{SI,xc}$	-1	$f_{ch,xc}$	$f_{pr,xc}$	$f_{li,xc}$								$f_{xI,xc}$			$k_{dis} \cdot X_c$
2 Hydrolysis Carbohydrates						-1													$k_{hyd,ch} \cdot X_{ch}$
3 Hydrolysis of Proteins							-1												$k_{hyd,pr} \cdot X_{pr}$
4 Hydrolysis of Lipids								-1											$k_{hyd,li} \cdot X_{li}$
5 Uptake of Sugars		$-(Y_{su})N_{bac}$							Y_{su}										$k_{m,su} \cdot \dfrac{S_{su}}{K_S + S_{su}} \cdot X_{su} \cdot I_1$
6 Uptake of Amino Acids		$N_{aa} - (Y_{aa})N_{bac}$								Y_{aa}									$k_{m,aa} \cdot \dfrac{S_{aa}}{K_S + S_{aa}} \cdot X_{aa} \cdot I_1$
7 Uptake of LCFA		$-(Y_{fa})N_{bac}$									Y_{fa}								$k_{m,fa} \cdot \dfrac{S_{fa}}{K_S + S_{fa}} \cdot X_{fa} \cdot I_2$
8 Uptake of Valerate		$-(Y_{c4})N_{bac}$										Y_{c4}							$k_{m,c4} \cdot \dfrac{(S_{va}+S_{bu})}{K_S+(S_{va}+S_{bu})} \cdot X_{c4} \cdot \dfrac{1}{1+(S_{va}+S_{bu})/(S_{va}+S_{bu})} \cdot I_2$
9 Uptake of Butyrate		$-(Y_{c4})N_{bac}$										Y_{c4}							$k_{m,c4} \cdot \dfrac{(S_{va}+S_{bu})}{K_S+(S_{va}+S_{bu})} \cdot X_{c4} \cdot \dfrac{1}{1+(S_{va}+S_{bu})/(S_{va}+S_{bu})} \cdot I_2$
10 Uptake of Propionate		$-(Y_{pro})N_{bac}$											Y_{pro}						$k_{m,pro} \cdot \dfrac{(S_{pro}+S_{bu})}{K_S+(S_{pro}+S_{bu})} \cdot X_{pro} \cdot I_3$
11 Uptake of Acetate		$-(Y_{ac})N_{bac}$												Y_{ac}					$k_{m,ac} \cdot \dfrac{(S_{pro}+S_{bu})}{K_S+(S_{va}+S_{bu})} \cdot X_{ac} \cdot I_3$
12 Uptake of Hydrogen		$-(Y_{h2})N_{bac}$													Y_{h2}				$k_{m,h2} \cdot \dfrac{S_{h2}}{K_S + S_{h2}} \cdot X_{h2} \cdot I_4$
13 Decay of X_{su}		$\sum X_{j,1,18}$			1				-1										$k_{dec,Xsu} \cdot X_{su}$
14 Decay of X_{aa}		$-\sum X_{j,1,18}$			1					-1									$k_{dec,Xaa} \cdot X_{aa}$
15 Decay of X_{fa}		$-\sum X_{j,1,18}$			1						-1								$k_{dec,Xfa} \cdot X_{fa}$
16 Decay of X_{c4}		$-\sum X_{j,1,18}$			1							-1							$k_{dec,Xc4} \cdot X_{c4}$
17 Decay of X_{pro}		$-\sum X_{j,1,18}$			1								-1						$k_{dec,Xpro} \cdot X_{pro}$
18 Decay of X_{ac}		$-\sum X_{j,1,18}$			1									-1					$k_{dec,Xac} \cdot X_{ac}$
19 Decay of X_{h2}		$-\sum X_{j,1,18}$			1										-1				$k_{dec,Xh2} \cdot X_{h2}$
A4 Valerate Acid-Base																			$k_{A/Bva} \cdot (S_{va^-} \cdot S_{H^+} - K_{a,va} \cdot S_{va})$
A5 Butyrate Acid-Base																			$k_{A/Bbu} \cdot (S_{bu^-} \cdot S_{H^+} - K_{a,bu} \cdot S_{bu})$
A6 Propionate Acid-Base																			$k_{A/Bpro} \cdot (S_{pro^-} \cdot S_{H^+} - K_{a,pro} \cdot S_{pro})$
A7 Acetate Acid-Base																			$k_{A/Bac} \cdot (S_{ac^-} \cdot S_{H^+} - K_{a,ac} \cdot S_{ac})$
A10 Inorganic Carbon Acid-Base			-1																$k_{A/Bco_2} \cdot (S_{HCO_3^-} \cdot S_{H^+} - K_{a,co_2} \cdot S_{IC})$
A11 Inorganic Nitrogen Acid-Base		1	-1																$k_{A/Bin} \cdot (S_{NH_3} \cdot S_{H^+} - K_{a,IN} \cdot S_{IN})$

Inhibition factors:

$I_1 = I_{pH} \cdot I_{IN,lim}$

$I_2 = I_{pH} \cdot I_{IN,lim} \cdot I_{H_2,fa}$

$I_3 = I_{pH} \cdot I_{IN,lim} \cdot I_{H_2,c4} \cdot I_{H_2,pro}$

$I_4 = I_{pH} \cdot I_{IN,lim} \cdot I_{nh3}$

TRANSITION TO LOW CARBON ECONOMY: CARBON CAPTURE APPROACHES TO BE APPLIED IN ENERGY-INTENSIVE INDUSTRIAL APPLICATIONS

Calin-Cristian CORMOS[1*], Cristian DINCA[2]

[1]Faculty of Chemistry and Chemical Engineering, Dept. of Chemical Engineering, Babes-Bolyai University, Cluj-Napoca, Romania
[2]Faculty of Power Engineering, Dept. of Energy Generation and Use, Politehnica University, Bucharest, Romania

Abstract

Reducing greenhouse gas emissions and transition to a low carbon economy for climate change mitigation represent key issues of modern society. The paper presents various carbon capture approaches to be applied in energy-intensive industrial applications based on fossil fuels (e.g. power generation, petro-chemistry, cement, metallurgy etc.). Fossil fuels are predicted to remain the backbone of energy sector in the years to come. To make acceptable the fossil fuels from environmental point of view, carbon capture, utilization and storage (CCUS) technologies must be implemented. The detailed examples presented in the paper make use of various assessment methods (e.g. mathematical modeling, simulation, thermal integration, techno-economic and environmental evaluations).

Keywords: carbon capture, utilization and storage (ccus), energy-intensive industrial applications, low carbon economy

1. Introduction

The increase of world energy demand put significant pressure on available energy sources (both fossil and renewable). Since the renewable energy sources have severe limitations in terms of availability, the fossil fuels are predicted to remain the backbone of energy sector in the decades to come. For instance, the latest statistical review of world energy resources indicates that at the current level of production, natural gas reserves will last about 56 years, oil about 53 years and coal about 109 [1]. The carbon intensity of fossil fuels varies widely, the liquid (oil) and solid (coal) fuels having the highest carbon footprint. To make acceptable, from environmental point of view, the continuous utilization of fossil fuels, new energy conversion technologies must be developed and deployed at

---

[*] Corresponding author - E-mail: cormos@chem.ubbcluj.ro, (C.L. Cormos)

industrial scale. Two important conditions must be met: improved energy conversion efficiency and low greenhouse gas emissions (especially CO_2).

Carbon Capture and Storage (CCS) or Carbon Capture, Utilization and Storage (CCUS) represent a diverse technology portfolio which imply that CO_2 resulted from the fossil fuel energy conversion is captured and then is either used for various applications (e.g. enhanced oil recovery, enhanced coal bed methane recovery, food industry etc.) or stored in proper geological locations (e.g. depleted oil and gas fields, saline aquifers etc.). Energy Technology Perspectives 2012 released by International Energy Agency (IEA) consider that for 2030 - 2050 timeline, CCS technologies are a key approach be used to meet deep emissions reduction goals [2]. For instance, as technology portfolio to reduce CO_2 emissions, CCS is predicted to account 20 - 25% having the highest contribution.

At EU level, several targets has been set for the whole community block for the period up to 2020 [3]: cutting greenhouse gases by at least 20% of 1990 levels; reducing energy consumptions by 20% of projected 2020 levels by improving energy efficiency and increasing use of renewable to 20% of total production. The long term target is to reduce the greenhouse gas emissions by 80 - 90% by 2050. Such ambitious targets require strong actions. For instance, in EU power generation sector, where coal contribution is about 60%, the deployment of CCS technologies is critical in the following years.

This paper has as aim to present various carbon capture approaches to be applied in fossil fuel-based energy-intensive industrial applications (e.g. power generation, oil and gas, cement, iron and steel etc.). Several detailed examples are given and evaluated covering various CO_2 capture methods and configurations (e.g. pre- and post-combustion capture using gas-liquid and gas-solid systems). For the evaluated cases, various assessment tools have been used: simulation using dedicated software (ChemCAD and Thermoflex) to produce the overall mass and energy balances; pinch method was used for thermal integration in view of energy efficiency optimization; key techno-economic and environmental performance indicators were calculated based on mass and energy balances.

2. Carbon capture approaches

There are three conceptual options for carbon capture to be implemented in fossil fuel energy conversion technologies: (i) pre-combustion capture which involves CO_2 capture from combustible gas (syngas) resulted from fossil fuels partial oxidation processes (e.g. hydrocarbons catalytic reforming, solid fossil fuels gasification); (ii) post-combustion capture is which CO_2 is captured from the flue gases resulted from fossil fuels total oxidation (combustion) and (iii) oxy-combustion in which the fossil fuel is burnt in oxygen environment to produce CO_2 and water and after water condensation the CO_2 is already captured. A good

overview of CO_2 capture processes is given by "Carbon Dioxide Capture and Storage" report of Intergovernmental Panel on Climate Change - IPCC [4]. Figure 1 presents the general carbon capture and storage (CCS) approaches to be used in fossil fuel energy conversion for power & heat applications [5].
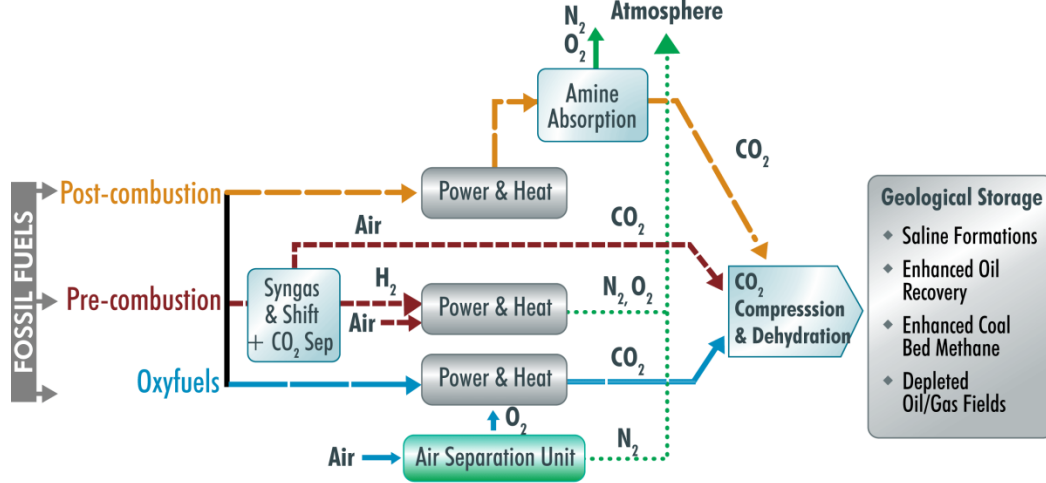
**Fig. 1.** CO_2 capture approaches in fossil fuel energy conversion for power & heat applications

In terms of contacting systems for CO_2 capture, various options are under consideration ranging from classical gas-liquid absorption (chemical and physical absorption) to complex biochemical or ionic liquid systems. Considering the stringent time considerations for developing and large scale deployment of carbon capture, utilization and storage technologies, the present paper is focused primarily on technologically and commercially mature options based on gas-liquid absorption as well as on promising under development methods such as chemical looping and calcium looping.

Gas-liquid absorption is a mature technology in petro-chemical applications including CO_2 capture from hydrogen production based on methane catalytic steam reforming [4]. Although from chemical engineering point of view this is a mature technology, its applications for carbon capture from energy conversion sector is rather new. Both pre- and post-combustion capture configurations can be use but the solvent selection criteria are different. For post-combustion CO_2 capture, only chemical absorption can be used due to the low CO_2 partial pressure in the treated flue gases (0.05 - 0.15 bar depending on fuel used and energy conversion technology). For pre-combustion capture configuration, the syngas resulted from reforming or gasification processes is first catalytically shift converted with steam to convert CO into CO_2.

$$CO_{(g)} + H_2O_{(g)} \Leftrightarrow CO_{2(g)} + H_{2(g)} \tag{1}$$

Both chemical and physical absorption can be used for CO_2 capture from shifted syngas due to high CO_2 partial pressure (10 - 15 bar depending on fuel used and operating parameters of reforming / gasification stage). There is a tendency to use more physical absorption because of lower heat consumption for solvent regeneration (pressure flash can be used for physical solvents regeneration in contrast with thermal regeneration for chemical solvents), higher absorption capacity and lower solvent degradation ratio. Figures 2 and 3 presents the conceptual process topology of chemical and physical gas - liquid absorption in pre-combustion CO_2 capture configuration [6].

Various physical, chemical and mixed solvents can be used for CO_2 capture. The most evaluated chemical solvents are alkanolamines, e.g. mono-ethanol-amine (MEA), diethanol-amine (DEA), methyl-diethanol-amine (MDEA). One of the main drawbacks of chemical absorption using alkanolamines is the heat duty for solvent regeneration (in the range of 3 MJ/kg CO_2). This solvent regeneration duty implies an energy penalty for the whole (including CO_2 capture) energy conversion design of at least 10 net electricity percentage points [6]. As physical solvents the most targeted commercial solvents are: Selexol^{TM} (mixture of dimethil-ethers of poly-ethylene-glycol), Rectisol (methanol in cryogenic conditions), Purisol (N-methl-2-pyrolidone) etc.
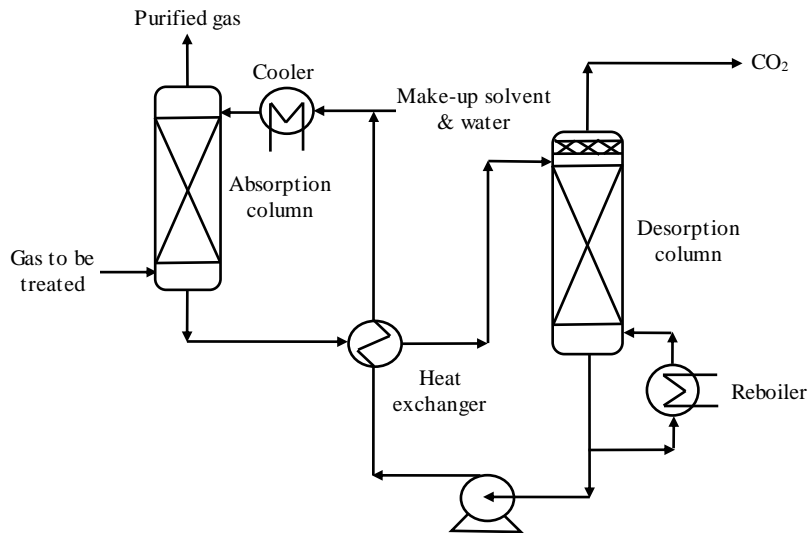
Fig. 2. CO_2 capture by chemical absorption (thermal regeneration of the solvent)
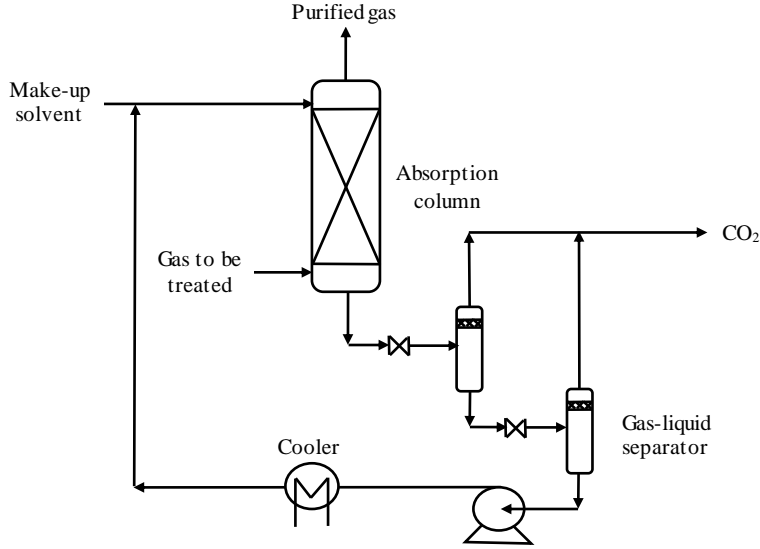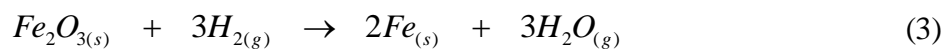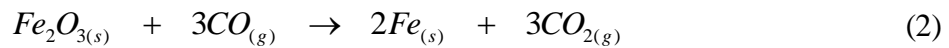
Fig. 3. CO_2 capture by physical absorption (pressure flash for solvent regeneration)

The heat duty for solvent regeneration is significantly lower for physical solvents
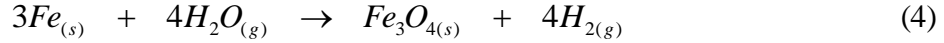being in the range of 0.2 - 0.5 MJ/kg CO_2 [7].

The lower heat duty of physical absorption implies an energy penalty for whole
energy conversion of about 8 - 9 net electricity percentage points. One of the main
aims of research and development activities in absorption-based carbon capture
was directed to reducing the energy penalty.

One of the most promising carbon capture method to reduce the energy penalty
for carbon capture is chemical looping [8]. These methods are still in the
development phase (laboratory and pilot installations up to 1 MW_{th}). In chemical
looping, an oxygen carrier (e.g. iron oxide) is used to oxidize the fuel. The gas
leaving the fuel reactor contains mainly CO_2 and H_2O. After water condensation,
captured CO_2 is ready to be sent to utilization or storage. The reduced oxygen
carrier is oxidized back with air, steam or a combination of both. When hydrogen
production is targeted steam is used. When heat and power generation is targeted
air is used (Chemical Looping Combustion - CLC). As an illustrative example,
when syngas is used as fuel, iron oxide is used as oxygen carrier and hydrogen
production is targeted, the chemical reactions are:
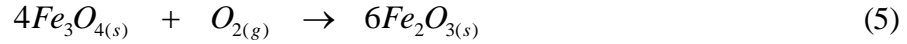 - Fuel reactor:

$$Fe_2O_{3(s)} \quad + \quad 3CO_{(g)} \quad \rightarrow \quad 2Fe_{(s)} \quad + \quad 3CO_{2(g)} \qquad (2)$$

$$Fe_2O_{3(s)} \quad + \quad 3H_{2(g)} \quad \rightarrow \quad 2Fe_{(s)} \quad + \quad 3H_2O_{(g)} \qquad (3)$$

- Steam reactor:

$$3Fe_{(s)} \;+\; 4H_2O_{(g)} \;\rightarrow\; Fe_3O_{4(s)} \;+\; 4H_{2(g)} \tag{4}$$

- Air reactor:
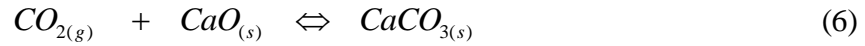
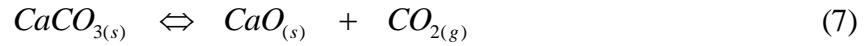$$4Fe_3O_{4(s)} \;+\; O_{2(g)} \;\rightarrow\; 6Fe_2O_{3(s)} \tag{5}$$

Metallic oxide-based chemical looping cycles can be used only in pre-combustion capture configurations.

A particular chemical looping option is based on calcium oxide / calcium carbonate cycle to capture CO_2 [8-9]. The plant concept uses two interconnected fluidized bed reactors for carbonation and calcination according to the following chemical reactions:

- Carbonation reactor:

$$CO_{2(g)} \;+\; CaO_{(s)} \;\Leftrightarrow\; CaCO_{3(s)} \tag{6}$$

- Calcination reactor:

$$CaCO_{3(s)} \;\Leftrightarrow\; CaO_{(s)} \;+\; CO_{2(g)} \tag{7}$$

Calcium looping (CaL) cycle can be used in both pre- and post-combustion capture configurations. Figure 4 presents the conceptual layout of CaL for post-combustion carbon capture.
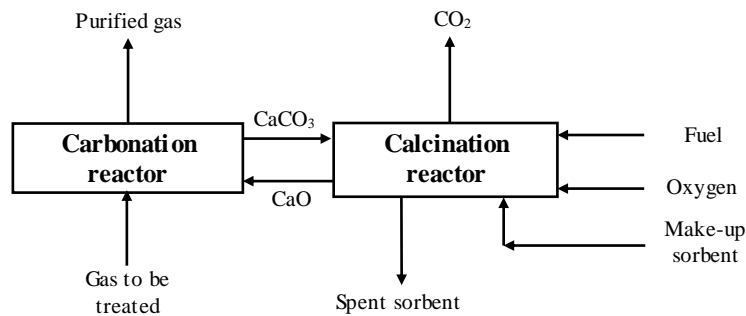


Fig. 4. CO_2 capture by calcium looping (CaL)

A distinct advantage of all chemical looping cycles compared to gas-liquid absorption is the high temperature heat recovery potential which significantly reduces the energy penalty for carbon capture. In the next chapter, some

illustrative case studies of these carbon capture options applied to various industrial processes (especially energy conversion sector) are presented.

### 3. Case studies of CO_2 capture applied to various industrial processes

3.1 Power generation based on coal gasification with CO_2 capture

This example considers power generation based on coal gasification using a dry fed syngas quench gasifier (Shell). The syngas is cooled, the ash removed then carbon monoxide is shift converted with steam. The pre-combustion carbon capture is done by physical absorption using Selexol^{TM} solvent. The power block is based on hydrogen-fuelled combined cycle gas turbine (M701G2 gas turbine was used). The process topology of the power plant is presented in Figure 5 [10].
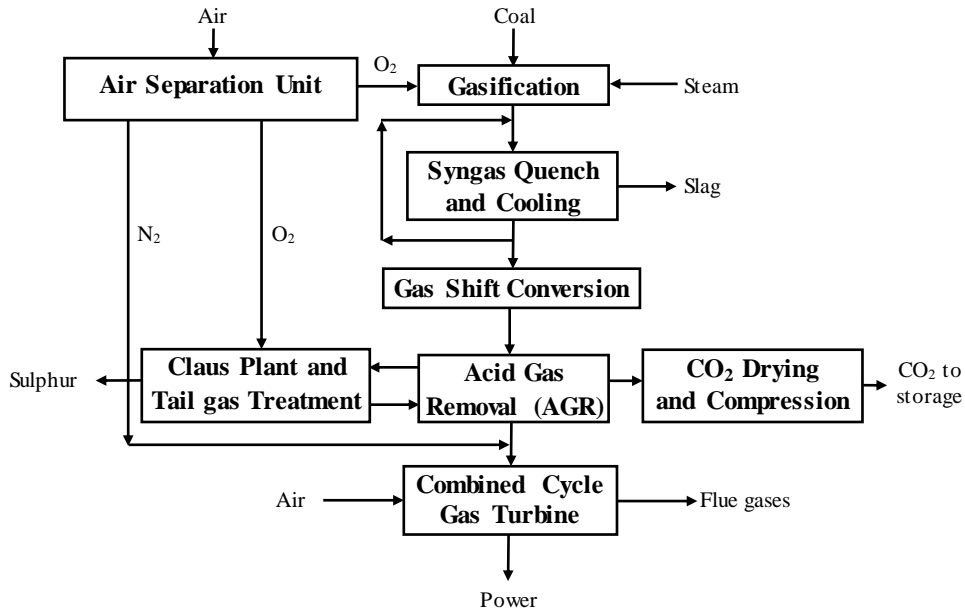
Fig. 5. Power generation based on coal gasification with pre-combustion CO_2 capture

The whole power plant concept was modeled and simulated using a commercial process simulator (ChemCAD). The simulation results were validated by comparison to literature data [11-12]. After simulation, the mass balance was used to perform the thermal integration using pinch method as presented in [6]. Figure 6 presents the composite curves (HCC - hot composite curve; CCC - cold composite curve) for the two most important plant sub-systems: the gasifier and syngas conditioning train (including shift conversion) and the power block.
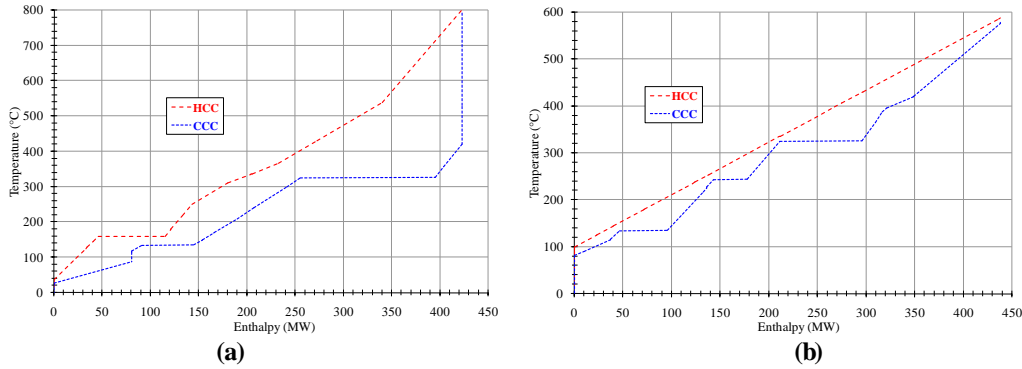
Fig. 6. Heat integration analysis for coal gasification with pre-combustion CO_2 capture:
(a) - gasifier and syngas conditioning train; (b) - combined cycle gas turbine

The simulation results were used for evaluation of plant performances. Table 1 presents the main results of technical and environmental evaluation in comparison with the corresponded design without carbon capture [10].

Table 1

Plant performances for power generation based on coal gasification

Main Plant Data	Units	No CCS	CCS
Coal thermal energy	MW_{th}	1055.00	1180.00
Gross power output	MW_e	558.14	554.25
Ancillary power consumption	MW_e	78.35	118.16
Net power output	MW_e	479.79	436.09
Net electrical efficiency	%	45.47	36.95
Carbon capture rate	%	0.00	90.55
Specific CO_2 emissions	kg / MWh	760.10	89.05

Comparing the two gasification-based evaluated cases, one without and one with CCS, the carbon capture energy penalty is about 8.5 net efficiency percentage points. The CCS design has a carbon capture rate of about 90% and the specific CO_2 emissions are reduced from 760 kg/MWh to about 89 kg/MWh.

3.2 Hydrogen production based on methane reforming with CO_2 capture

This example considers hydrogen production based on natural gas catalytic steam reforming. The generated syngas is cooled, and then CO is shift converted with steam to maximize the hydrogen production. The pre-combustion carbon capture is done by chemical absorption using Methyl-Diethanol-Amine (MDEA). The process topology of the plant is presented in Figure 7 [13].
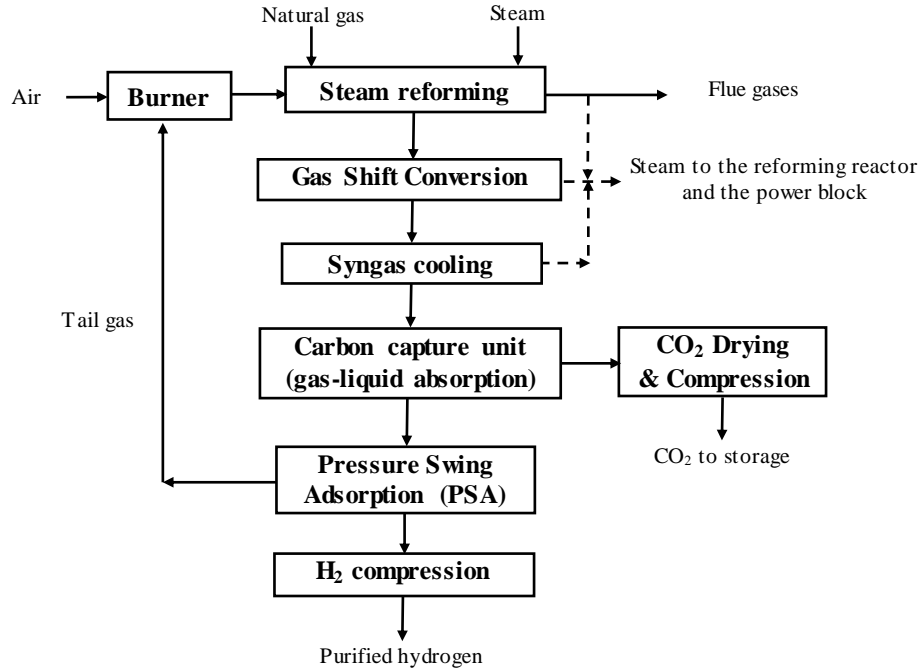
Fig. 7. Hydrogen production based on natural gas catalytic steam reforming (NGCSR)
with pre-combustion CO_2 capture

As main design assumption, an output hydrogen stream of 300 MW_{th} was
considered (purity 99.95% vol.). The whole power plant concept was modeled and
simulated using a commercial process simulator (ChemCAD). The simulation
results were validated by comparison with literature data [13]. The simulation
results were used for evaluation of plant performances. Table 2 presents the main
results of technical and environmental evaluation in comparison with the
corresponded design without carbon capture. Comparing the two NGCSR-based
evaluated cases, one without and one with CCS, the carbon capture energy penalty
is about 2.6 net cumulative energy efficiency percentage points. The CCS design
has a carbon capture rate of about 70% and the specific CO_2 emissions are
reduced from 270 kg/MWh to about 84 kg/MWh. The reason for lower carbon
capture rate of reforming case in comparison to gasification case is the un-reacted
methane from the syngas. Another important conclusion is that reforming case has
lower carbon capture energy penalty than gasification case (mainly due to lower
plant complexity and lower carbon content of the fuel).

Plant performances for hydrogen production based on NGCSR

Main Plant Data	Units	No CCS	CCS
Natural gas thermal energy	MW_{th}	410.00	410.00
Hydrogen output	MW_{th}	300.00	300.00
Gross power output	MW_e	18.25	12.15
Ancillary power consumption	MW_e	6.55	11.01
Hydrogen efficiency	%	73.17	73.17
Net power efficiency	%	2.85	0.27
Cumulative energy efficiency	%	76.02	73.44
Carbon capture rate	%	0.00	70.00
Specific CO_2 emissions	kg / MWh	270.10	83.95

3.3. Calcium looping applied for CO_2 capture

This example considers CO_2 capture using calcium looping from the flue gases resulted from a combustion-based power plant. The steam power plant considered in this example uses a super-critical steam cycle (290 bar / 582°C with two steam reheats at 75 bar / 580°C and 20 bar / 580°C). The flue gases are desulphurised in a conventional wet limestone-based unit and then they are treated for carbon capture in a calcium looping cycle. The CO_2 is captured in the carbonation reactor and then it is released in the calcination reactor. Since, the limestone decomposition is heavily endothermic; an additional coal has to be oxy-combusted in the calcination reactor. Both hot gas streams resulted from carbonation and calcination reactors are used for steam generation which is then integrated in the steam cycle of the main power plant. Part of the calcium-based adsorbent is deactivated in the process, and then a fresh make-up has to be provided. The conceptual layout of the power plant is presented in Figure 8 [14].
As main design assumption, a steam-based power plant generating about 1000 MW net power was considered. The whole power plant concept was modeled using ChemCAD process simulator. The simulation results were used for evaluation of plant performances. Table 3 presents the main results of the evaluation in comparison with the corresponded design without CO_2 capture [14].
Comparing the two combustion-based evaluated cases, one without and one with CCS, the carbon capture energy penalty is about 7.6 net efficiency percentage points. The CCS design has a carbon capture rate of 92% and the specific CO_2 emissions are reduced from 800 kg/MWh to about 70 kg/MWh. As can be noticed, calcium looping implies a lower energy penalty for carbon capture than gas-liquid processes (especially using chemical absorption). The economic factors of calcium looping are also favorable compared to gas-liquid absorption.
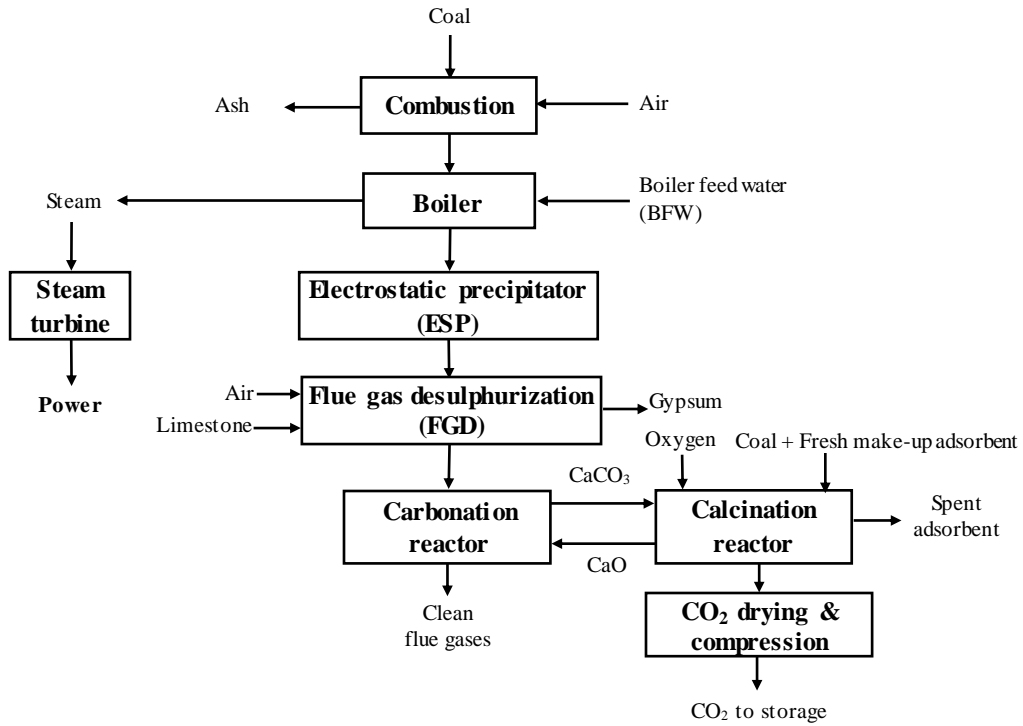
Fig. 8. Calcium looping used for post-combustion CO_2 capture in a steam-based power
plant.

Table 3

Plant performances for calcium looping used in combustion-based power plants

Main Plant Data	Units	No CCS	CCS
Coal thermal energy	MW_{th}	2184.48	3022.58
Gross power output	MW_e	1008.75	1300.55
Ancillary power consumption	MW_e	58.50	215.14
Net power output	MW_e	950.25	1085.41
Net electrical efficiency	%	43.50	35.91
Carbon capture rate	%	0.00	92.50
Specific CO_2 emissions	kg / MWh	800.58	70.24

Calcium looping cycle has the particular advantage that can be integrated also in
other industrial applications for instance in cement manufacture where limestone

decomposition takes part of the production process. In this way the spent sorbent resulted from the calcination reactor can be easily used.

3.4. Comparison of techno-economic and environmental performances

To summarize the main techno-economic and environmental performances of various carbon capture options, Table 4 presents the results of the key performances indicators considering various carbon capture options applied to the same coal-based gasification process as benchmark case [6-7,9-10,14-15].

Table 4

Comparison of main techno-economic and environmental performances

Main Plant Data	Units	Pre-combustion (solvents)	Post-combustion (solvents)	Calcium looping	Iron looping
Net power efficiency	%	33 - 37	33 - 35	35 - 37	36 - 38
Carbon capture rate	%	~90	~90	90 - 95	>95
Specific CO_2 emissions	kg / MWh	80 - 100	90 - 110	30 - 70	<30 - 35
Specific investment cost	€ / kW net	2400 - 2800	2800 - 3200	2300 - 2600	2200 - 2600
O&M costs	€ / MWh	35 - 40	38 - 45	34 - 36	32 - 35
Cost of electricity	€ / MWh	75 - 85	80 - 90	75 - 80	70 - 80
CO_2 removal cost	€ / t	22 - 25	25 - 30	20 - 25	20 - 25
CO_2 avoided cost	€ / t	25 - 30	30 - 35	25 - 30	25 - 28

As can be noticed from the illustrative example of gasification process, there are a distinct energy efficiency, carbon capture rate and cost advantages of innovative chemical looping methods over the gas-liquid absorption options.

4. Conclusions

The present paper presents, through various examples, the conceptual approaches to be follow when carbon capture technologies having economic potential are to be implemented in energy-intensive industrial applications (e.g. power generation, petro-chemical, metallurgy etc.). The gas-liquid absorption options (both chemical and physical absorption) are commercially and technologically mature processes. The main drawback of these technologies being the high energy penalty for carbon capture (especially chemical absorption). One of the most promising

carbon capture option to reduce both energy and cost penalties is based on chemical looping. However, these technologies require substantial development and scale-up in order to be applied at industrial scale.

Acknowledgements

REFERENCES

[1]. BP*, Statistical Review of World Energy*, June 2013 (www.bp.com).

[2]. International Energy Agency*,* Energy Technology Perspectives 2012, Pathways to a Clean Energy System, Paris, France, 2012 (www.iea.org).

[3]. European Commission*,* Communication from the Commission. 20 20 20 by 2020: Europe's climate change opportunity, Brussels, Belgium, 2008.

[4]. Metz, B., Davidson, O., de Coninck, H., Loos, M., Meyer, L*, Carbon Dioxide Capture and Storage*, Intergovernmental Panel on Climate Change (IPCC), Zurich, Switzerland, 2005.

[5]. Cooperative Research Centre for Greenhouse Gas Technologies, 2014 (www.co2crc.com.au).

[6]. Cormos, C. C., *Decarbonizarea combustibililor fosili solizi prin gazeificare*, Cluj University Press, Cluj-Napoca, Romania, 2008.

[7]. Padurean, A., Cormos, C. C., Agachi, P. S., Pre-combustion carbon dioxide capture by gas-liquid absorption for Integrated Gasification Combined Cycle power plants, *International Journal of Greenhouse Gas Control*, 7, (2012), Elsevier B.V.

[8]. Fan, L.S., Chemical looping systems for fossil energy conversions, Wiley-AIChE, 2010.

[9]. Cormos, C. C., Economic implications of pre- and post-combustion calcium looping configurations applied to gasification power plants, *International Journal of Hydrogen Energy*, (2014), (accepted, in press).

[10]. Cormos, C. C., Techno-economic and environmental evaluations of large scale gasification-based CCS project in Romania, *International Journal of Hydrogen Energy,* 39, (1), (2014), Elsevier B.V.

[11]. Higman, C., van der Burgt, M., *Gasification*, 2nd ed., Burlington: Gulf Professional Publishing, Elsevier Science, 2008.

[12]. International Energy Agency (IEA) - Greenhouse Gas R&D Programme (GHG), Potential for improvement in gasification combined cycle power generation with CO_2 capture, (2003), Report PH4/19.

[13]. International Energy Agency (IEA) - Greenhouse Gas R&D Programme (GHG), Decarbonisation of fossil fuels, Report PH2/2, 1996.

[14]. Cormos, C. C., Petrescu, L., Evaluation of calcium looping as carbon capture option for combustion and gasification power plants, 7th Trondheim CCS Conference - TCCS-7, Trondheim, (2013), Norway.

[15]. Cormos, C. C., Integrated assessment of IGCC power generation technology with carbon capture and storage (CCS), *Energy*, 42 (1), (2012), Elsevier B.V.

REMOVAL OF ZINC IONS AS ZINC CHLORIDE COMPLEXES USING PUROLITE A103S RESIN

Emilia GÎLCĂ, Andrada RUŞOLAN, Andrada MĂICĂNEANU[*], Petru ILEA

Department of Chemical Engineering, Babeş-Bolyai University, Faculty of Chemistry and Chemical Engineering, 11 Arany Janos, 400028 Cluj Napoca, Romania

Abstract

The aim of this study was to investigate the capacity of Purolite A103S to remove zinc as chloride complexes from hydrochloric acid solutions (2M). Influence of the zinc initial concentration on the removal process, was estimated. The experimental data were analysed using Langmuir, Freundlich, and Temkin isotherm models. The Temkin isotherm model indicates that zinc sorption is characterized by a physisorption process.

Keywords: zinc; isotherm models; hot-dip galvanizing

1. Introduction

Effluents contaminated by heavy metals are commonly produced from many kinds of industrials processes [1]. Zinc is widely used in various fields, *e.g.* galvanization, paint, batteries, smelting, pesticides, fossil fuel combustion, polymer stabilizers [2].

In the case of zinc hot-dip galvanizing process, the pickling step generates effluents containing high concentrations of $ZnCl_2$, $FeCl_2$, and HCl [3]. Taking into consideration that an anion exchanger can separate the main components, iron and zinc, of the raw solution from hot-dip galvanizing [4], we studied removal of zinc-chloride complexes formed in hydrochloric acid solution using anion exchanger resins [3].

In our previous paper, we tested four anion exchangers to remove zinc as chloride $[ZnCl_3]^-$ from hydrochloric solutions (1 M) and the best results were obtained on Amberlite IRA 410 followed by Purolite A103S resin with almost similar efficiency [3]. This study has aimed at investigating the capacity of Purolite A103S resin to remove zinc chloride complexes from 2 M HCl solutions.

---

[*] Corresponding author - E-mail address: andrada@chem.ubbcluj.ro, (A. Măicăneanu)

2. Experimental

2.1. Reagents

Analytical reagents, HCl and ZnCl$_2$, were purchased from Merck Co. Initial zinc solutions (500 − 1100 mg/L) were prepared by dissolving ZnCl$_2$ salt in a 2 M HCl solution.
A weak basic anion exchanger resin, *i.e.* Purolite A103S, was employed for investigation and its characteristics are summarized in our previous paper [3]. Before its use, the resin was soaked in double distilled water for 24 h and then washed several times.

2.2. Apparatus and analytical procedure

The sorption experiments were performed in batch conditions, using 5 g Purolite A103S resin contacted with zinc solutions (100 mL) at different initial concentrations at room temperature. The stirring rate was maintained at 300 rpm using a magnetic stirrer for 300 min. Samples of 1 mL were taken at established time intervals and the concentration of zinc in solutions was determined using an atomic absorption spectrophotometer Avanta PM GBC (Australia) [3].
The amount of sorbed zinc per unit mass of anion exchanger (ionic exchange capacity) was calculated using equation:

$$q_e = \frac{(C_o - C_e)}{m} \cdot \frac{V}{1000} \tag{1}$$

where C_o, C_e are the initial and equilibrium zinc ion concentrations (mg/L), q_e is the ionic exchange capacity (mg/g), V is the volume of zinc ion solution (mL), and m is the mass of resin (g) [3,5].

3. Results and discussions

3.1. Effect of the initial concentration

The results obtained for the sorption of zinc by Purolite A103S starting from different initial concentrations are presented in Fig. 1. In the considered range of concentration, *i.e.* 500 - 1100 mg/L, zinc sorption was rapid in the first minutes and further the sorption rate decreased. It was noted that zinc ionic exchange capacity at 500 mg/L was 10.07 mg/g and 21.36 mg/g at 1100 mg/L.
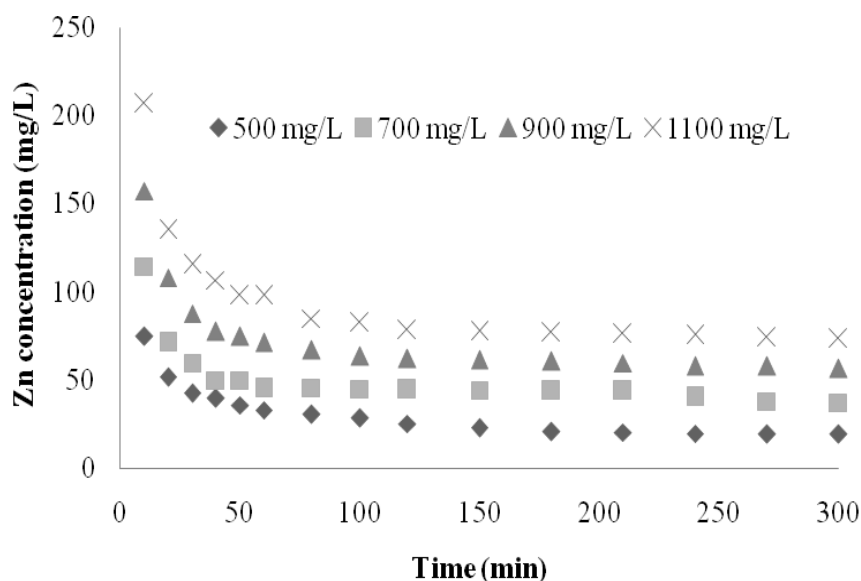
Fig. 1. Effect of the initial zinc concentration on sorption by Purolite A103S.

3.2. Isotherm models

The equilibrium data were analysed using three isotherm models, *i.e.* Langmuir, Freundlich, and Temkin.

Langmuir isotherm

The linear form of Langmuir isotherm, valid for monolayer adsorption onto specific homogenous sites, is given by correlation [5]:

$$\frac{1}{q_e} = \frac{1}{q_{max} \cdot K_L \cdot C_e} + \frac{1}{q_{max}} \tag{2}$$

where, K_L is the Langmuir adsorption constant (L/mg), q_{max}, q_e are the maximum and equilibrium adsorption capacities (mg/g), and C_e is the equilibrium zinc concentration in the solution (mg/L) [3,5].
The isotherm parameters, q_{max} and K_L, obtained from the slope and intercept of the plot $1/q_e$ vs. $1/C_e$ (Fig. 2) are presented In Table 1.
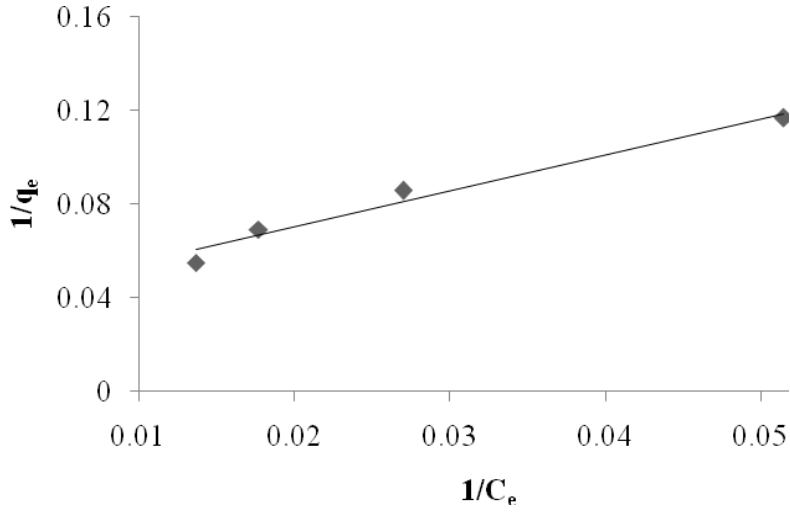
Fig. 2. Langmuir adsorption isotherm for zinc sorption on Purolite A103S.

Table 1

Isotherm constants for zinc sorption on Purolite A103S

| Langmuir	q_m (mg/g)	K_L (L/mg)	R^2
	25.64	0.64	0.969
Freundlich	n	K_F ($mg^{(1-1/n)}L^{1/n}/g$)	R^2
	1.82	1.65	0.983
Temkin	A_T (L/g)	B (J/mol)	R^2
	2.01	1.23	0.942

Freundlich isotherm

The Freundlich isotherm describes the adsorption characteristics for the heterogeneous surface and it can be expressed as follows [5]:

$$\log q_e = \log K_F + \frac{1}{n}\log C_e \tag{3}$$

where K_F and n are isotherm constants, indicating the capacity and intensity of the adsorption, and 1/n is a function of the strength of adsorption [3,5].

Isotherm constant K_F and n (Table 1) were obtained from the slope and the intercept of the linear plot $\log q_e$ vs. $\log C_e$ (Fig. 3).
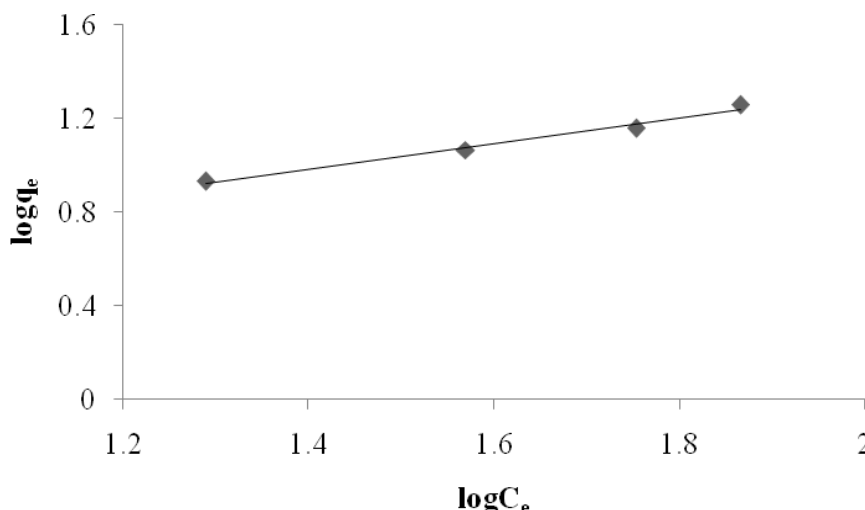
Fig. 3. Freundlich adsorption isotherm for zinc sorption on Purolite A103S.

From the data presented in Tabel 1, n value was determined to be 1.82, indicating that zinc sorption on Purolite A103S was cooperative. The same result was obtained on Amberlite IRA410 resin [3].

Temkin isotherm

The Temkin isotherm assumes that the heat of adsorption of each molecules in the layer decreases linearly rather than logarithmically with the coverage. The equations of this model are expressed as follows[3,5]:

$$q_e = B \ln A_T + B \ln C_e \tag{4}$$

$$B = \frac{RT}{b_T} \tag{5}$$

where A_T is the Temkin isotherm equilibrium constant (L/g), b_T is Temkin isotherm constant, and B is a constant related to heat of adsorption (J/mol) [3,5]. A_T and B constants were determined from a q_e vs. $\ln C_e$ plot (Fig. 4).
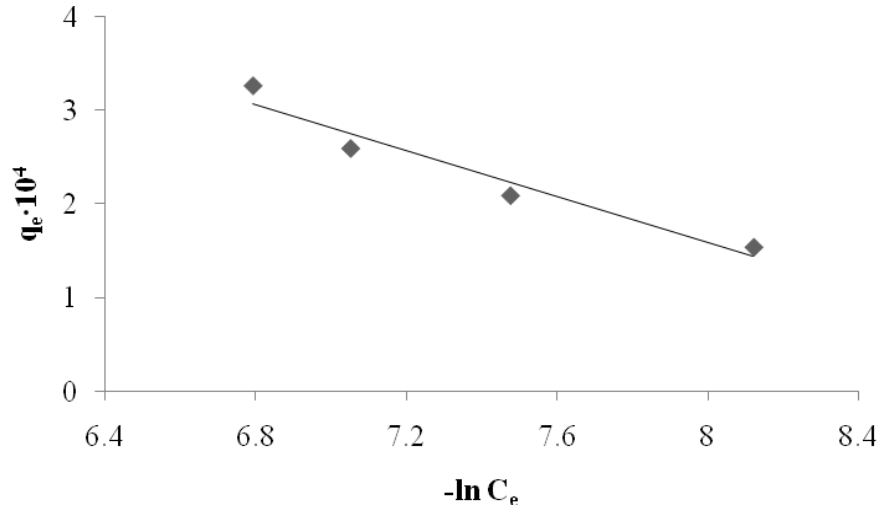
Fig. 4. Temkin adsorption isotherm for zinc sorption on Purolite A103S.

Taking into consideration that the calculated value (Tabel 1) of the constant related to heat of sorption (B) had a value smaller than 20 kJ/mol [6], we concluded that the sorption process takes place as physisorption. The same result was obtained on Amberlite IRA410 resin [3].

3.3. Kinetics studies

Pseudo-first-order and pseudo-second-order reaction kinetics models were applied to determine the reaction order and rate constant of the ion exchange process [3,7].

Pseudo-first-order

Mathematical expression for pseudo-first-order suggested by Lagergren is:

$$\ln(q_e - q_t) = \ln q_e - k_1 t \tag{6}$$

where q_e and q_t (mg/g) are the amount of zinc adsorbed at equilibrium and time t (min) and k_1 is the first-order rate constant (1/min) [3,7].
Pseudo-first-order parameters and correlation coefficients (R^2) obtained by plotting $\ln(q_e - q_t)$ vs. time are presented in Table 2. Based on the results obtained in Table 2, the pseudo-first-order cannot be used to describe the sorption

process because the calculated q_e values are different from the experimental values.

Pseudo-first-order and pseudo-second-order reaction kinetics constants for zinc sorption on Purolite A103S.

C_0 (mg/L)	$q_{e,exp}$ (mg/g)	Pseudo-first-order			Pseudo-second-order		
		k_1 (1/min)	$q_{e,calc}$ (mg/g)	R^2	k_2 (g/mg·min)	$q_{e,calc}$ (mg/g)	R^2
500	10.07	0.027	2.05	0.889	0.053	10.14	1
700	13.68	0.013	1.02	0.632	0.061	13.69	1
900	16.97	0.017	1.51	0.782	0.045	17.03	1
1100	21.36	0.019	2.17	0.830	0.033	21.45	1

Pseudo-second-order

The pseudo-second-order kinetic model proposed initially by Ho and McKay [3,7] is given by correlation (7):

$$\frac{t}{q_t} = \frac{1}{k_2 q_e^{\,2}} + \frac{1}{q_e} t \qquad (7)$$

where k_2 is the second-order rate constant (g/mg ·min) [7].

The values of pseudo-second-order equation parameters were calculated from the slope and intercept of t/q_t vs. time and are given in Table 2. Based on the fact that $q_{e,calc}$ and $q_{e,exp}$ values are almost similar, sorption of zinc as chloride complexes on Purolite A103S is described by the pseudo-second-order model. In our previous paper [3] we obtained the same result on Amberlite IRA410 resin.

4. Conclusions

Based on the obtained results it was noted that the ionic exchange capacity at equilibrium increased with the initial zinc concentration.

The results reveal that the isotherm models fitted the experimental data in the order: Freundlich > Langmuir > Temkin. The Freundlich isotherm indicated that zinc sorption on Purolite A103S was cooperative and the parameter calculated from Temkin isotherm predicted a physisorption process.

Kinetics studies suggested that zinc removal as zinc chloride complexes on Purolite A103S, a weak basic anion exchanger resin, was best described by pseudo-second-order kinetic model.

REFERENCES

[1] Abbas M., Kaddour S., Trari M., Kinetic and equilibrium studies of cobalt adsorption on apricot stone activated carbon. *Journal of Industrial and Engineering Chemistry*, 20, (2014), 745–751.

[2] Gakwisiri C., Raut N., Al-Saadi A., Al-Aisri S., Al-Ajmi A., A critical review of removal of zinc from wastewater. Proceedings of the World Congress on Engineering , (2012), Vol. I.

[3] Gîlcă E., Măicăneanu A., Ilea P., Removal of zinc ions as zinc chloride complexes from strongly acidic aqueous solution by ionic exchange. *Central European Journal of Chemistry*, 12 (8), (2014), 821–828.

[4] Csicsovszki G., Kékesi T., Török T.I., Selective recovery of Zn and Fe from spent pickling solutions by the combination of anion exchange and membrane electrowinning techniques. *Hydrometallurgy*, 77, (2005), 19–28.

[5] Dada A.O., Olalekan A.P., Olatunya A.M., Dada O., Langmuir, Freundlich, Temkin and Dubinin–Radushkevich isotherms studies of equilibrium sorption of Zn^{2+} onto phosphoric acid modified rice husk. *Journal of Applied Chemistry*, 3, (2012), 38–45.

[6] Itodo A.U., Itodo H.U., Sorption energies estimation using Dubinin-Radushkevich and Temkin adsorption isotherms. *Journal or Life Sciences*, 7, (2010), 31–39.

[7] Sarı A., Tuzen M., Biosorption of Pb(II) and Cd(II) from aqueous solution using green alga (*Ulva lactuca*) biomass. *Journal of Hazardous Materials*, 152, (2008), 302–308.

KINETIC MODELLING OF COPPER LEACHING PROCESS USING FeCl₃ FOR RECYCLING WASTE ELECTRICAL AND ELECTRONIC EQUIPMENTS

Ioana A. POPESCU[1*]**, Tamas VARGA**[2]**, Attila EGEDY**[2]**, Szabolcs FOGARASI**[1]**, Petru ILEA**[1]

[1]Babeş-Bolyai University, Department of Chemical Engineering, 11 Arany Janos Street, 400028 Cluj Napoca, Romania
[2] University of Pannonia, Department of Process Engineering, 10 Egyetem Street, H-8200 Veszprém, Hungary

Abstract

The process of copper leaching from waste electrical and electronic equipment (WEEE) was investigated by leaching in a ferric chloride environment. The factors affecting process performance, such as temperature and oxidant concentration were thoroughly scrutinized. Experimental data was used to determine the reaction rate parameters, such as the pre-exponential factor, activation energy and reaction order. We propose a new shrinking core model to define the exact geometrical changes that appear in the dissolution process. The values of the identified kinetic parameters indicate continues increase of copper leaching performances with the increase of operating temperature and oxidant concentration.

Keywords: waste electrical and electronic equipment, copper leaching, kinetic process, modelling

1. Introduction

Waste electrical and electronic equipment (WEEE) is a growing concern globally. The lifespan of electrical and electronic equipment (refrigerators, washing machines, mobile phones, computers, printers, TVs) is relatively short and decreases continuously as a result of rapid changes in the characteristics and performance. It thus generates a significant amount of waste [1, 2].

Copper is one of the most used materials in the production of electrical and electronic equipment. The copper recycling became more important lately as a result of resource depletion, as well as the continuous increase of copper demand. Also, the development of recycling processes is an important aspect of the efficient use of resources and minimizing copper negative effects of hazardous

---

* Corresponding author –E-mail address: alipopescu@yahoo.com, (Ioana Popescu)

materials on the environment [3, 4]. The processes used for copper recycling firstly depend on the copper content of raw materials. The distribution and the size of those materials and the presence of other constituents in those contents are other factors, which determine the development of a recycling process [2].

The methods used to recover copper from electronic waste are based on mechanical, pyrometallurgical and hydrometallurgical processes [5]. Mechanical and pyrometallurgical processes were commercially used in the recycling industry. Disadvantages posed by these processes are limited to air pollution and high energy consumption. Hydrometallurgical methods are more accurate, predictable and easier to control than pyrometallurgical processing, when used for recovery of metals from PCBs [6, 7]. Over time, metallic copper dissolution has been the subject of many investigations using aqueous ammonia oxidizing agent [8, 9]. Another strong oxidizer is nitric acid where copper is dissolved in the form of Cu $^{2+}$. Ferric ion is one of the most powerful oxidizing agents in the dissolution of metallic copper and is mostly found in ferric chloride or ferric sulphate. Ferric chloride plays a very important role in accelerating the dissolution of metallic copper, which tends to function both as an oxidant and a complexant [4].

This paper aims to estimate the copper leaching kinetic when ferric chloride is the active media, so that the measurements were carried out applying ferric chloride as oxidant. Kinetic models with redox systems were developed and validated using measurements data. To define the exact geometrical changes that appear in the leaching process we propose a new shrinking core model.

2. Experimental

Material

All copper samples used in the dissolution process were obtained from WEEE. A cylindrical copper sample with a weight in the interval of 2 − 4 g and a length ranging between 2.8 and 3.4 cm with a diameter of 0.24 − 0.27 cm was used for each experiment. The metallic copper wire had a purity of 99.99%. The composition of the samples was determined by dissolution in *aqua regia* and analysis with an atomic absorption spectrometer Avanta PM GBC Australia (AAS).

Leaching process

The experiments were performed in an isothermal stirred batch reactor. In each experiment a quantity of 100 ml of ferric chloride solution was introduced in the reactor. When the desired stirring speed and reaction temperature were reached, the solid sample was added into the reactor. At specific time intervals 1 mL

sample was taken out of the reactor. All samples were analyzed by AAS. After each experiment the copper sample was dried and weighted to check the reliability of the AAS measurements.

3. Kinetic modelling

The dissolution of metallic copper in acidic solutions of $FeCl_3$ is a heterogeneous reaction [10]. In literature there are multiple methods to calculate the reaction rate of copper leaching process [11-13]. The basic methods use Arrhenius-expressions, and single reaction rate as parameter. A more punctual method refers to multiple parameters identification for each reaction process [14, 15]. With the determination of pre-exponential constants (k_0), activation energies (E_a) and reaction orders, the concentration and temperature dependence can be examined. These methods, which consider a kinetic specific to homogene systems, are not specifics to leaching reactions, but they are widely used when it accepts that the reactions take place at leaching metal surface. Therefore, we use these assumptions despite of the fact that the dissolution (leaching) process of metal is basically a heterogeneous chemical reaction with multiple steps.

If ferric chloride is being used as an oxidant, two reactions can be identified. Both Fe^{3+} and Cu^{2+} ions can dissolve Cu, as seen in Eq. 1 and Eq. 2.

$$Cu + 2Fe^{3+} \rightarrow Cu^{2+} + 2Fe^{2+} \tag{1}$$

$$Cu + Cu^{+2} \rightarrow 2Cu^{+} \tag{2}$$

The kinetic model is characterized by two reaction rates as represented in Eq. 3 and Eq. 4.

$$r_1 = k_{01} \cdot \exp\left(-\frac{E_{a1}}{R \cdot T}\right) \cdot \left(C_{Fe^{3+}}\right)^{n_1} \tag{3}$$

$$r_2 = k_{02} \cdot \exp\left(-\frac{E_{a2}}{R \cdot T}\right) \cdot \left(C_{Cu^{2+}}\right)^{n_2} \tag{4}$$

The process rates represented in Eq. 1 and Eq. 2 are dependent on the area between the solid and the liquid phases. To calculate the changes in mass of copper wire we multiply the calculated reaction rates with the surface area (A) of the wire:

$$\frac{dm}{dt} = -A \cdot (r_1 + r_2) \cdot M_{Cu} \tag{5}$$

Eq. 6 to Eq. 9 represent the component balances for Fe^{3+}, Fe^{2+}, Cu^{2+} and Cu^{+}, where V_0 refers to the initial volume.

$$\frac{dC_{Fe^{3+}}}{dt} = -\frac{2 \cdot A \cdot r_1}{V_0} \tag{6}$$

$$\frac{dC_{Fe^{2+}}}{dt} = \frac{2 \cdot A \cdot r_1}{V_0} \tag{7}$$

$$\frac{dC_{Cu^{2+}}}{dt} = \frac{A \cdot (r_1 - r_2)}{V_0} \tag{8}$$

$$\frac{dC_{Cu^{+}}}{dt} = -\frac{2 \cdot A \cdot r_2}{V_0} \tag{9}$$

The balance switch is used to calculate the changes in concentration and solid phase mass in case of Cu leaching in ferric chloride. For our two reactions, six parameters must be calculated; two set of pre-exponential constants (k_0), activation energies (E_a) and reaction orders. We defined the objective function as the sum of square error between the measured and calculated concentration profiles. The experimental data, reported in figure 3 and 4, has been used for minimization of objective function in order to obtain the above-mentioned parameters. Table 1 shows the results of the identified reaction parameters.

Table 1

Identified reaction parameters

Parameter	Value	Unit
k_{01}	3.8E-3	$mol^{1-n_1} \cdot m^{3n_1-2} \cdot s^{-1}$
E_{a1}	18018	$J \cdot mol^{-1}$
n_1	1.43	-
k_{02}	31.92	$mol^{1-n1} \cdot m^{3n_1-2} \cdot s^{-1}$
E_{a2}	43834	$J \cdot mol^{-1}$
n_2	2.32	-

Shrinking core model

To define the exact geometry changes shrinking core model can be used. In our case a two dimensional method were created to calculate the diameter and length changes in time. The results were validated against measurements. The initial shape in the experiments was a cylinder, so the calculation of the length and diameter can be completed, and the kinetics can be extended to be a surface dependent one (see figure 1).
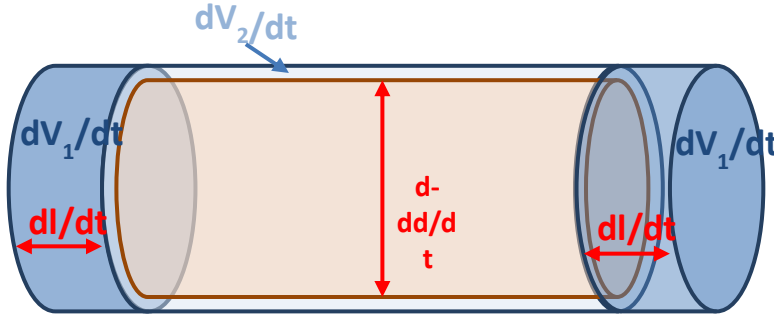
Fig. 1. Calculation of the geometry changes

The volume change from the length changes:

$$\frac{dV_1}{dt} = \frac{dl}{dt} \cdot \frac{d^2 \cdot \pi}{4} \tag{10}$$

The volume changes from the diameter changes:

$$\frac{dV_2}{dt} = (l - \frac{dl}{dt}) \cdot \frac{\left(2 \cdot d \cdot \frac{dd}{dt} - \left(\frac{dd}{dt}\right)^2\right) \cdot \pi}{4} \tag{11}$$

We can assume:

$$\frac{dV_1}{dV_2} = \frac{A_1}{A_2} \cdot \frac{\frac{d^2 \cdot \pi}{2}}{d \cdot \pi \cdot L} = \frac{d}{2 \cdot L} \tag{12}$$

The sample used presents a cylindrical geometry (diameter $-$ d, length $-$ l). The change in length is described by:

$$\frac{dl}{dt} = \frac{4 \cdot \frac{dm}{dt}}{\rho_{copper} \cdot \left(1 + \frac{2l}{dt}\right) \cdot d^2 \pi} \tag{13}$$

The change in diameter can be represented by:

$$\frac{dd}{dt} = d - d^{0.5} \cdot \left(l - \frac{dl}{dt}\right)^{-0.5} \cdot \left(d \cdot l - d \cdot \frac{dl}{dt} - 2 \cdot l \cdot \frac{dl}{dt}\right)^{0.5} \tag{14}$$

The relations (13) and (14), where dm/dt resulted from relation (5), can predict the time evolution of length and diameter of the cylindrical copper particle. As figure 2 shows this proposed approach is capable of calculating the changes in measures, and mass, so we can build it to the program, and use for further calculations. Continuous line represents the values obtained through modelling and points correspond to the experimental data.
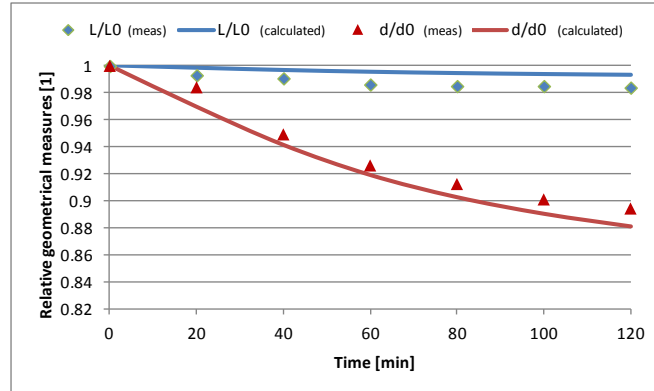
Fig. 2. The differences between the measured and model computed copper particle dimensions temperature:25°C, initial FeCl$_3$ concentration: 200 mol/m3, initial mass of copper particle:1.971g

4. Results and discussions

The experiments were conducted to separately investigate the performance and efficiency of the Fe$_3$Cl solution in the leaching of copper samples. As it has shown, the factors affecting the efficiency and performance of the leaching process are temperature and concentration of Fe$_3$Cl in the acid leaching solution. Based on experimental data the specific kinetic parameters were identified (see table 1)

Effect of temperature: The effect of temperature on the leaching process of copper was investigated for 30, 45 and 60 °C. We can observe that the dissolution of copper increases with the rise in temperature. If we compare the leaching state for 45 and 60 °C we have obtained, for the initial concentration of 0.4 M FeCl$_3$ and two hours leaching time, an increase of 18.4 % in dissolved copper.
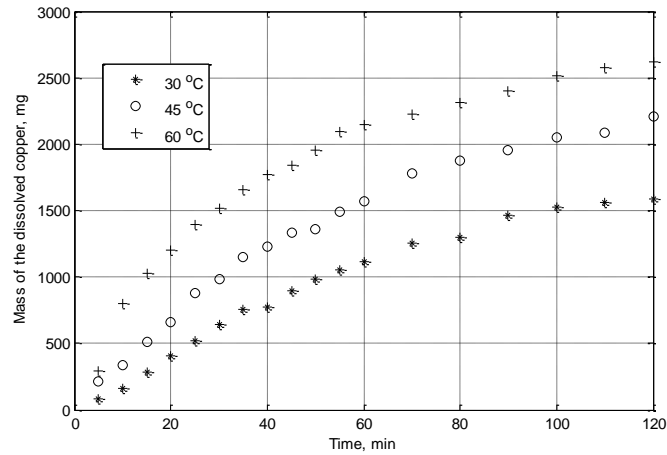
Fig. 3. Evolution of the dissolved copper mass at different temperatures for 0.4 M ferric chloride concentration

Effect of concentration: The effect of ferric chloride solution concentration was investigated for values of 0.1, 0.2 and 0.3 M and for an leaching time no more than 2 h. The increase in ferric chloride concentration produces an increase in the quantity of dissolved copper. An increase of oxidant concentration from 0.3 M to 0.4 M at 60 °C results in a rise of 69.5% of dissolved copper (figure 4). Figure 4 also contains process dynamics data in the form needed for reaction model parameters identification.
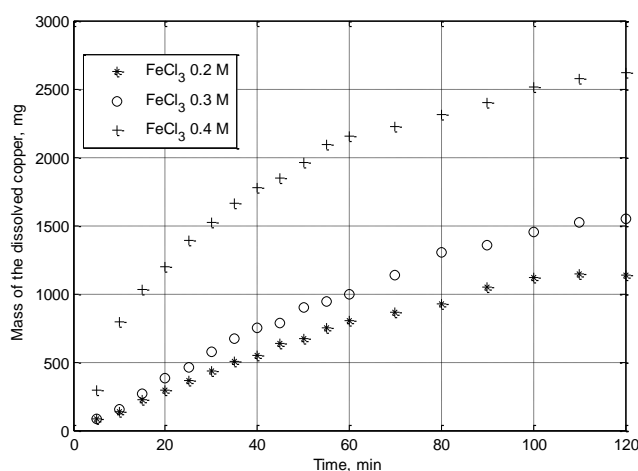
Fig. 4. Evolution of the dissolved copper mass at different concentrations at a temperature of 60 °C

Results of kinetic identification process of FeCl₃ model

Figure 5 shows a comparison between experimental and model computed dynamics of the dissolved copper mass. We mention that the parameters of processing two reactions (two set of pre-exponential constants (k_0), activation energies (E_a) and reaction orders) have been identified using experimental data from figures 3 and 4. The difference between the measurement and the calculated values are relatively small, however higher differences can be observed in some cases. In conclusions we can state, that with the identified model parameters the systems can be describe adequately.
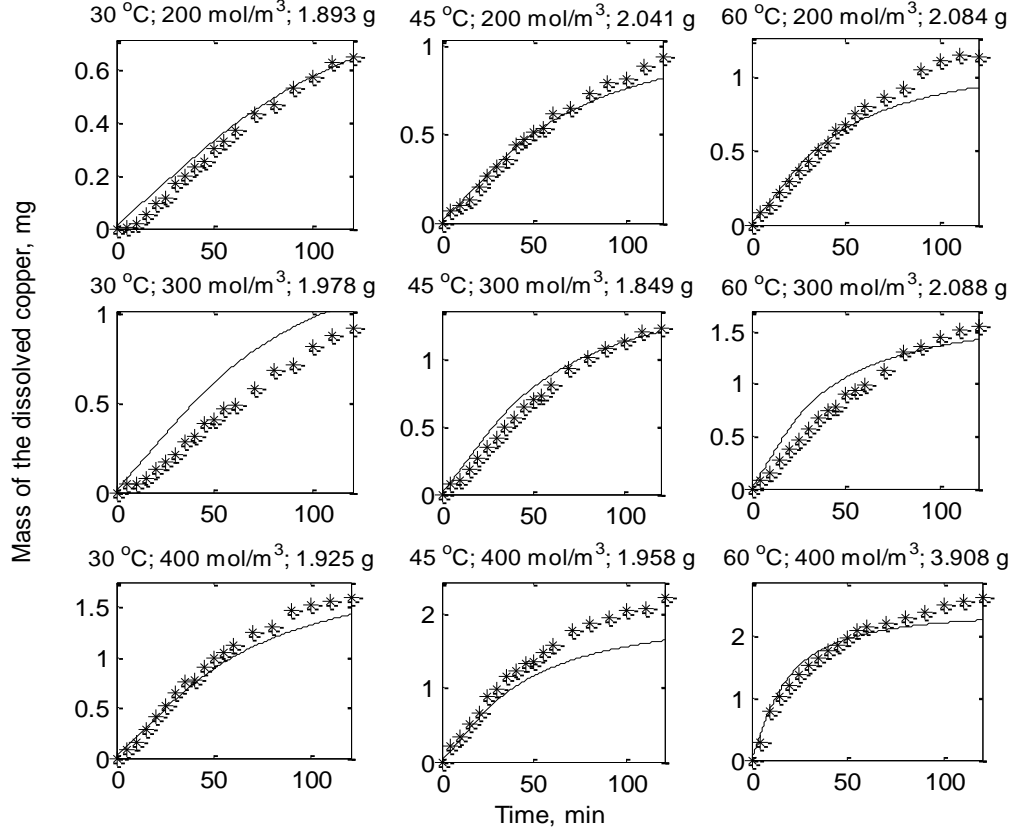
Fig. 5. Results of kinetic identification process of FeCl$_3$ model where the continuous line represents the values obtained through modelling and points correspond to the experimental data

5. Conclusions

Experimental study and modelling for copper dissolution in ferric chloride solution was investigated. Best performance can be obtained by using a high temperature and concentration of oxidant. The proposed mathematical model was used in order to identify the kinetic parameters characterizing the global surface reactions of the leaching process. The identified reaction parameters and kinetic model will be used for our next studies for recovery copper from WEEE. The model can be valued for describing similar products involving dissolution of metals or alloys.

Acknowledgement

REFERENCES

[1] Huisman, J. et al., *Review of Directive 2002/96 on Waste Electrical and Electronic Equipment* (WEEE), United Nations University, Bonn, Germany, 2007.

[2] Kang, H.I., Schoenung, J. M., Electronic waste recycling: A review of U.S. infrastructure and technology options, *Resources, Conservation and Recycling*, 45, (2005), 368–400.

[3] Fogarasi S., Imre-Lucaci F., Ilea P., A. Imre-Lucaci, The environmental assessment of two new copper recovery processes from Waste Printed Circuit Boards, *Journal of Cleaner Production*, 54, (2013), 264-269.

[4] Wang Z., Che J.,Ye C., Application of ferric chloride both as oxidant and complexant to enhance the dissolution of metallic copper, Hydrometallurgy, 105, (2010), 69–74.

[5] Schluep, M., Sustainable Innovation and Technology Transfer Industrial Sector Studies. Recycling from E-waste to resources, UN Environmental Programme, UN Univ., Bonn, 2009.

[6] Hansen U., Product cycles, *The key for sustainable development*. IRB Verlag, Stuttgart, 2000.

[7] Goosey, M., Kellner, R., Recycling technologies for the treatment of end of life printed circuit boards (PCBs). *Journal Circuit World*, 29 (2003) 33-37.

[8] Lane, R.W., Mcdonald, H.J., Kinetics of the reaction between copper and aqueous ammonia, *Journal of the American Chemical Society*, 68, (1946), 1699–1704.

[9] Zembura, Z., Piotrowski, A., Kolenda, Z., A mass transfer model for the autocatalytic dissolution of a rotating copper disc in oxygen saturated ammonia solutions, *Journal of Applied Electrochemistry*, 20, (1990) 365–369.

[10] Ma, R., *Principle on Hydrometallurgy*, Metallurgical Industry Press, Beijing, (2007).

[11] Demir, H., Özmetin, C., Kocakerim, M.M., Yapici, S., Çopur, M., Determination of semiempirical kinetic model for dissolution of metallic copper particles in HNO_3 solutions, *Chemical Engineering and Processing* 43 (8), (2004), 1095–1100.

[12] Popescu I.A, Egedy A., Fogarasi Sz., Varga T., Ilea P., Kinetic modelling and optimisation of copper leaching process from waste electrical and electronic equipments, Romanian International Conference on Chemistry and Chemical Engineering 18, (2013), Sinaia, Romania,

[13] Yang H., Liu J., Yang J., Leaching copper from shredded particles of waste printed circuit boards, *Journal of Hazardous Materials*, 187, (2011), 393–400.

[14] Ahmed I.M, Nayl A.A, Daoud J.A., Leaching and recovery of zinc and copper from brass slag by sulfuric acid, *Journal of Saudi Chemical Society*, DOI: 10.1016/j.jscs.2012.11.003, (2012), in press.

[15] Liu Z., Yin Z., Hu H., Chen Q., Leaching kinetics of low-grade copper ore containing calcium-magnesium, carbonate in ammonia-ammonium sulfate solution with persulfate, *Trans. Nonferrous Met. Soc.*, 22, (2012), 2822-2830.

ADOPT DIVIDING –WALL COLUMNS (DWC) FOR LIGHT ENDS PROCESSING

Cosmin COJOCARU, Cristian TOGAN and Claudia I. KONCSAG*

University "Ovidius" of Constanta

Abstract

This is a case study of light ends processing in an oil refinery by adopting the dividing-wall distillation columns (DWC). Simulations in CHEMCAD 6.3.1 were performed in three distillation sequences: the original sequence with simple columns, a sequence including a DWC with three products and another one including a DWC with four products. The simulations were performed with respect to the purity of products and with the main objective of energy savings. The DWC was modeled as a sequence of two columns: one pre-fractionator performing like the section before the dividing wall followed by a pump around column. The study demonstrated that DWC in Kaibel configuration can be adopted successfully with great energy savings.

Keywords: Dividing Wall Column, Three Product Specifications, Four Product Specifications, Kaibel Column Simulation, Energy Saving

1. Introduction

A multicomponent mixture with *n* components is conventionally separated into pure components in a sequence of *(n-1)* distillation columns, with one top product and one bottom product each. *E.g.* A ternary mixture needs a sequence of two distillation columns connected either in a direct way, by separating the compounds in order of decreasing volatilities, or in an indirect way, by separating first the heavier compound. More components lead to more separation variants. The old idea of Petlyuk [1] to change the conventional separation with two thermally completely integrated distillation columns was improved by G.Kaibel in 1987 [2] who designed the dividing-wall column with the advantages of a single compact column and developed by B.Kaibel *et al* in 2006 [3].

Since then, separation processes using dividing wall distillation columns (DWC) were investigated by simulation and proved to be energy efficient: separation of aromatics multicomponent mixtures [4-6], alcohols mixtures [7], bioethanol

---

* Corresponding author: E-mail address: ckoncsg@yahoo.com, (Claudia Koncsag)

purification through extractive and azeotropic distillation [8], reactive distillation [9,10] and C4-C7 alkanes distillation [11,12].

This is a case study of light ends processing in an oil refinery, separating the C2-C5 alkanes mixture. Starting from the original process, we propose and debate two other separation variants, each sequence including a dividing-wall column. The simulations are performed in CHEMCAD with the main objective to minimize energy requirements at fixed product purities or recovery degrees and to minimize plant cost in the same conditions.

2. Problem statement

The Light End Unit of an oil refinery processes at present 14143 kg/h fraction C2-C5 with the following composition, % wt: Methane(C1)-1.72; Ethane(C2)-4.58; Propane(C3)-9.29; i-Butane(i-C4)-10.17; n-Butane(n-C4)-23.62; i-Pentane(i-C5)-26.81; n-Pentane(n-C5)- 23.85. As long as the refinery processes the same oil, and this seems to be the situation, the feed composition will be always close to this. The separation requirements of different products are expressed in terms of purity or recovery degree as seen in table 1. Depending on the market's demand, the unit can produce LPG or pure isobutane and pure n-butane.
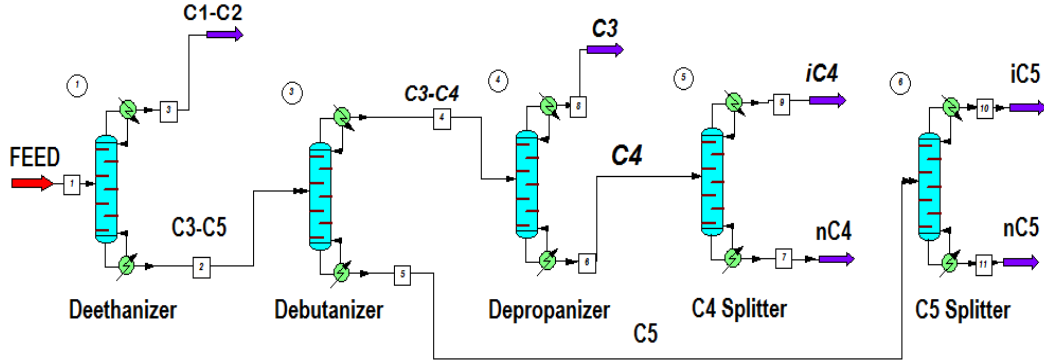
Table 1

Light Ends Unit. Products specifications and recovery degrees, %wt

Propane	Isobutane	n-Butane for rubber	LPG	Isopentane/ n-Pentane separation
C2-max. 5	C3-max.8	C3-max.0.2	C3- max.12% C4-min.87%	φ_{nC5}-0.98
C3-min. 92	i-C4-max.80	i-C4-max 4	C5-max.5%	
C4-max.2	n-C4-difference nC5-max. 0.5	n-C4-min.94 i-C5+n-C5-max 1		

The present sequence of columns is given in figure 1 and the equipment specifications and operating parameters are given in table 2.

In the present configuration, the direct sequence couldn't be adopted entirely because of the large flows of C4-C5 in the feed so, the debutanizer's position is before the depropanizer as a column with equilibrated internal flows and by consequence with a smaller diameter. The most difficult separations, iC4/nC4 and iC5/nC5, were left at the end of the separation train, because these require a large number of trays and lower pressure in the columns. However, the pressure in the C4 splitter is imposed at a higher value (p=10 bar) for condensation's feasability. By design, the pressure in the de-propanizer is 18 bar but simulations at 10 bar

proved that the column performs well at this pressure, so the debutanizer, the depropanizer and the C4 splitter can work all at approx. 10 bar with small differences due to the pressure drop in the transfer lines. This gave us the idea of including these columns in a Kaibel- type column with dividing wall (DWC).

Fig. 1. Present configuration of Light Ends Unit.

Columns specifications for the Light Ends Unit

			De-ethanizer	De-butanizer	De-propanizer	iC4-nC4 Splitter	iC5-nC5 Splitter
Equipment specifications	No. of stages	Design	24	30	30	59	59
	Feed Stage	Design	12	12	12	16	26
	Pressure (bar)	Design	34	9.5	18	10	1.9
		Simulation	25	10	10	10	2
Parameters	Top temperature (^{o}C)	Design	45	49	49	52	55
		Simulation	-2	57	25	65	48
	Bottom temperature (^{o}C)	Design	120	92	92	62	85
		Simulation	133	119	74	78	57

Data in table 2 refer to classical separation design (mentioned as Design) and simulation results using modified operating condition that can be applied when a dividing wall column is used (mentioned as Simulation)

85

In the present configuration, the direct sequence couldn't be adopted entirely because of the large flows of C4-C5 in the feed so, the debutanizer's position is before the depropanizer as a column with equilibrated internal flows and by consequence with a smaller diameter. The most difficult separations, iC4/nC4 and iC5/nC5, were left at the end of the separation train, because these require a large number of trays and lower pressure in the columns. However, the pressure in the C4 splitter is imposed at a higher value (p=10 bar) for condensation's feasability. By design, the pressure in the de-propanizer is 18 bar but simulations at 10 bar proved that the column performs well at this pressure, so the debutanizer, the de-propanizer and the C4 splitter can work all at approx. 10 bar with small differences due to the pressure drop in the transfer lines. This gave us the idea of including these columns in a Kaibel- type column with dividing wall (DWC).

The compact structure performing the same separations like two or three column, as seen in Figure 2, should be adopted as a new separation scheme using fully thermally coupled distillation columns, for energy savings.

(a)   (b)
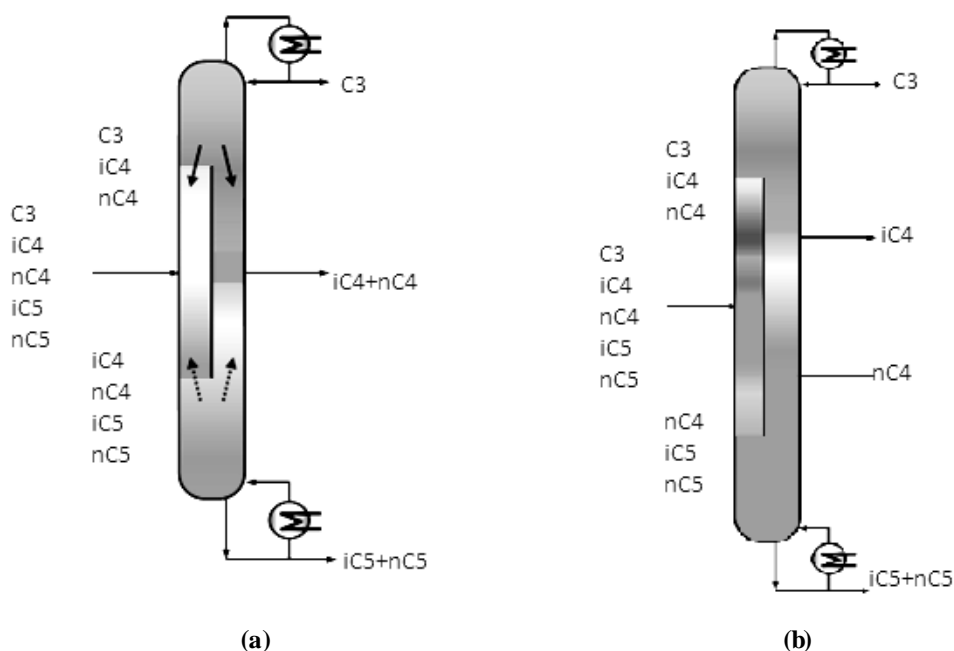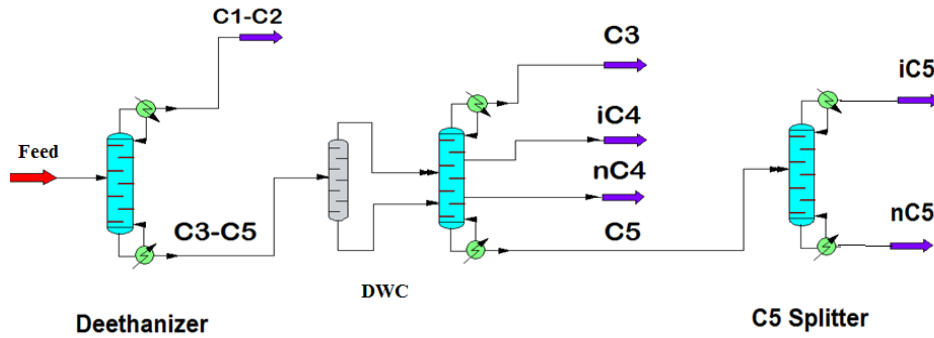
Fig. 2. Dividing- wall column DWC with (a) one side product and (b) two side products.

We performed the simulation of the Light Ends Unit in CHEMCAD 6.3.1, in three variants: the original sequence (figure 1), the sequence including one dividing-wall column with one side product (figure 3) and the sequence including one dividing-wall column with two side products (figure 4).
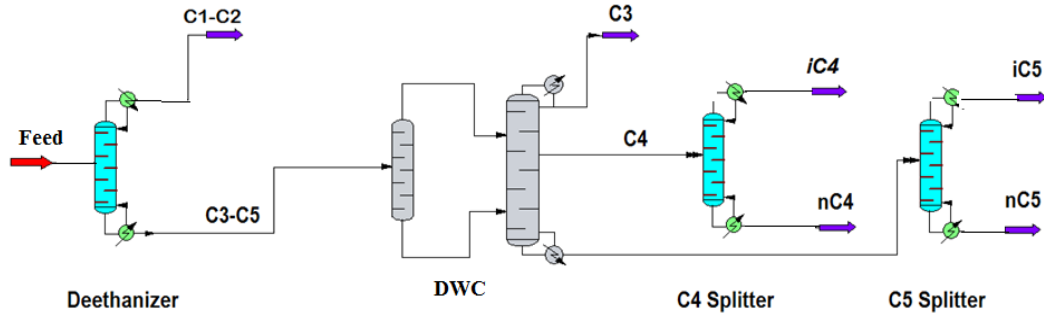
Fig. 3. Configuration of the Light End Unit including DWC with one side product.

Fig. 4. Configuration of the Light Ends Unit including DWC with two side products.

The commercial process simulators do not include yet the dividing wall column. For the modeling of the process in a DWC, the general approach is a sequence of simple columns with one top product and one bottom product each. Another approach is one column pump-around model [13]. Since one column pump around model has better convergence, the sequence of simple columns is easier to evaluate [14].

In this work, we adopted a model with pre-fractionator plus one column with side products. The pre-fractionator performs like the section before the dividing wall in the DWC. The dividing wall was considered in central position related to the trays (vertically). The specifications for the pre-fractionator included the number of stages, the partial condensation of vapors in the condenser, distillate mole flow rate and bottom product temperature. The specifications for the column with side products included the number of stages, the partial condensation in the condenser, the two feed positions, the position of side products trays, partial condensation of

side products, etc. The simulations were performed with respect to the purity or recovery degrees of products as mentioned in table 1. The condensers and reboilers duties resulted from calculations. Then the sizing of the columns including annexed equipment was performed and the cost of installed equipment resulted. The cost index was updated according to the Chemical Engineering's Plant Cost Index (CEPCI) in February 2014 [15]. The costs for low pressure steam and cooling water were considered local in 2013:$ 6.5 GJ^{-1} for cooling water and $18.32 GJ^{-1} for steam. The cost of the refrigerant at -20°C was considered following the guideline offered in [13] as $ 7.89 GJ^{-1}.

3. Results and discussions

The comparative results of the simulations in three variants (figures 1, 3 and 4) are presented in table 3 which summarizes the energy requirements for condensers and reboilers and the costs with the installed equipment.

Table 3

Summary of energy requirements and equipment costs in three variants

Separation sequence	Condensers duty, GJ h^{-1}	Reboilers duty GJ h^{-1}	Installed equipment costs (mil. $)
Original configuration	-90.7	+91.2	6.5
Sequence including DWC with one side product	-44.8	+44.2	10.15
Sequence including DWC with two side products	-65.2	+65.7	8.53

The calculations are not detailed, only major items such as columns and annexes (reboilers and condensers) were taken into account, this being a fair approach for this type of case study.

In the second configuration, the Kaibel column with one side product has 80 trays, the wall is on 30 trays height (from the tray # 26 to #55), and the extraction tray for the sideproduct is 30. In the second configuration, the cost of the installed equipment is the highest because the DWC is expensive and the two splitters remain in the sequence since in the third configuration, the DWC cost is comparable but only one splitter remains. The DWC in the third variant has 100 trays and a wall on 50 trays height, also central (from tray #26 to # 75), and extraction trays for iC4 and nC4 are 30 and 70 respectively.

As one can see in table 3, the condensers and reboilers duties are much lower in the second and in the third variants, which is the point of using DWC. In the second variant, the energy savings are more important (51.1%).

(a)   **(b)**
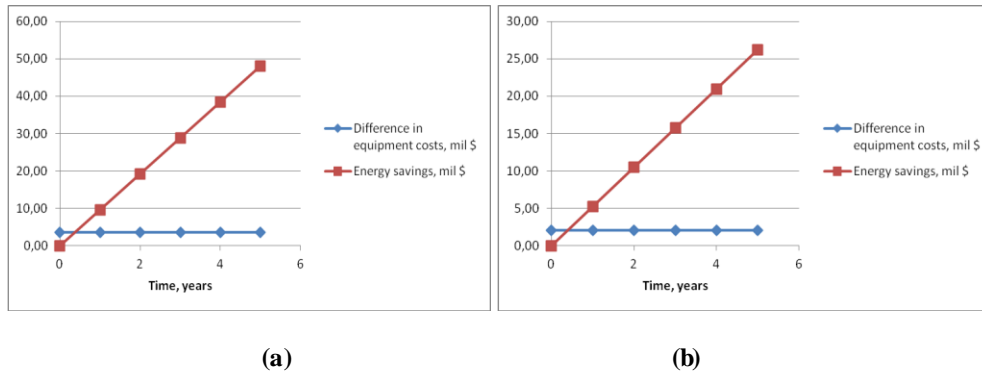
Fig. 5. Investment recovery and energy saving for sequence including DWC with one side product (a) and for sequence including DWC with two side products.

The costs with the utilities are \$2260 per hour in the original configuration, \$1100,6 h^{-1} for the configuration with DWC and one side product and \$1627 h^{-1} for the third variant. The differences in equipment costs can be recovered in a few months and after that, savings of \$9.6 mil a year proceed from adopting the DWC with one side product and \$5.24 mil a year for DWC with two side products. In figure 5, one can see that in a few months the differences in equipment costs can be recovered and during 5 years energy savings rise to \$ 48 mil in case of DWC with one side product and \$ 26.2 mil in case of DWC with two side products.

In conclusion, the column with two side products seems to be less efficient but its exact configuration could be changed for improving the energy savings. Besides the Kaibel column adopted here, there are other configurations: the Sargent arrangement [16], the Agrawal arrangement [17], the triangular wall structures [18] and other arrangements can be conceived and simulated.

4. Conclusions

The Kaibel column configuration can be applied successfully to light-ends processing in oil refineries, as demonstrated by simulations in this case study.

Despite higher costs with equipment, the investment can be recovered in short time due to important energy savings.

The separation sequence with Kaibel column with three products (one side product) seems to be more profitable than that with two side products in Kaibel configuration but further study will be performed for optimization of DWC configuration having in view more energy savings.

REFERENCES

[1] .Petlyuk F. B., Platonov V.M., Slavinskii D. M., Thermodynamically optimal method for separating multicomponent mixtures, *International Chemical Engineering*, 5, (1965), 555–561.

[2] ..Kaibel G., Distillation columns with vertical partitions, *Chemical Engineering Technology*, 10, (1987), 92–98.

[3] ..Kaibel B., Jansen H., Zich E. Olujic Z., Unfixed Dividing Wall Technology For Packed And Tray Distillation Columns, (2006), IChemE Symposium Series No. 152, Paper BK1126-Kaibel_R1_280906.

[4] ..Dejanovic I., Matijasevic Lj., Halvorsen I.J., Skogestad S., Jansen H., Kaibel B., Olujic Z., Designing four-product dividing wall columns for separation of a multicomponent aromatics mixture*, Chemical Engineering Research and Design*, 89, (2011), 1155–1167.

[5] .Kiss A.A., Rewagad R.R., Energy efficient control of a BTX dividing-wall column, *Computers and Chemical Engineering*, 35, (2011), 2896– 2904.

[6] ..Kiss A.A., Ignat R. M., Flores Landaeta S. J., de Haan A. B., Intensified process for aromatics separation powered by Kaibel and dividing-wall columns, *Chemical Engineering and Processing: Process Intensification*, 67, (2013) 39– 48.

[7] ..Ghadrdan M., Halvorsen I. J., Skogestad S., Optimal operation of Kaibel distillation columns, *Chemical Engineering Research and Design*, 89, (2011), 1382–1391.

[8] Kiss A A., Suszwalak D. J-.P.C., Enhanced bioethanol dehydration by extractive and azeotropic distillation in dividing-wall columns, *Separation and Purification Technology*, 86, (2012), 70–78,.

[9] ..Kiss A A., Suszwalak D. J.-P.C., Innovative dimethyl ether synthesis in a reactive dividing-wall column, *Computers and Chemical Engineering*, 38, (2012), 74– 81.

[10] Huang K., Wang S-J., Shan L., Zhu Q., Qian J., Seeking synergistic effect—A key principle in process intensification, *Separation and Purification Technology*, 57, (2007), 111–120.

[11] Halvorsen I. J., Skogestad S., Energy efficient distillation, *Journal of Natural Gas Science and Engineering*, 3, (2011), 571-580.

[12] Errico M., Tola G., Rong B-G., Demurtas D., Turunen I., Energy saving and capital cost evaluation in distillation column sequences with a divided wall column, *Chemical Engineering Research and Design*, 87, (2009), 1649–1657.

[13] Kiss A.A., *Advanced Distillation Technologies. Design and Applications*, Wiley, Chichester UK, 2013

[14] Dejanovic, I., Matijasevic, Lj., Olujic, Z. Dividing wall column – A breakthrough towards sustainable distilling. *Chemical Engineering and Processing: Process Intensification*, 49, (2010), 559–580.

[15] *** Chemical Engineering's Plant Cost Index, May Issue 2014, www.che.com

[16] Agrawal, R. Processes for multicomponent separation, (2001a *), US Patent No. 6286335*.

[17] Agrawal, R. Process for separation of multicomponent fluids using a multizone distillation column, describing a dividing wall column configuration with additional horizontal partition on product side, with side reboiler and side condenser above and below the horizontal partition wall, respectively, (2001b *), US Patent No. 6250106 B1*.

[18] Yildirim, O., Kiss, A.A., Kenig, E.Y. Dividing wall columns in chemical process industry: A review on current activities. *Separation and Purification Technology*, 80, (2011), 403–417.

CHARACTERIZATION OF THE CIRCULAR FLOW OF VISCOUS LIQUIDS THROUGH RING-SHAPED SECTIONS

Zeno GROPŞIAN , **Andra TĂMAŞ[*], Romulus MINEA[*], Nicu BORŞ**

Universitatea Politehnica Timişoara, Facultatea de Chimie Industrială şi Ingineria Mediului, Bld. Vasile Pârvan 6, 300223 Timişoara

Abstract

The assessment of fluids turbulence found in a liquid subjected to a circular motion through specific ring-shaped spaces can be expressed by the Taylor-Reynolds number (Ta_{Re}). It depends on the centrifugal and viscous friction forces that occur in close correlation with the geometry of the flow area, revolution and liquid properties, especially viscosity. Experimental determinations were performed on the mixtures ethylene glycol-water, glycerine-water, mineral oils (paraffin and transformer oil), magnetic fluids, castor oil mixed with different pyromellitic esters, surfactant-based fracturing fluids. It was used a rotational viscometer Rheotest-2 or a Couette type viscometer with glass cylinders for flow visualization. The measured shear stress and dynamic pressure created during liquid flow were correlated with the Ta_{Re} number.

Keywords: Circular motion, dynamic pressure, ring-shaped space, shear stress, Taylor-Reynolds number

1. Introduction

Reynolds number, expressed as the ratio of inertial forces and the viscous friction forces, is commonly invoked to characterize the hydrodynamic regime of linear fluids flow, being also used in the calculation of convective heat and mass transfer.

Circular movement of liquids through ring-shaped spaces, seen in some industrial equipment (evaporators, centrifuges, hydrocyclones) or at rotational viscometer, leads to the appearance of centrifugal force field determined by the geometry of ring-shaped space or the initial speed of the liquid and by the rotation of some parts of the device. The ring-shaped space is characterized by the radii of the inner and outer cylinder (r_i and r_o), by their difference ($\delta = r_o - r_i$) or ratio, as well as by the revolution (n) or angular velocities (Ω_i and Ω_o), that can be given to both
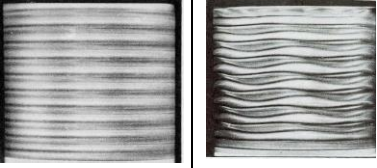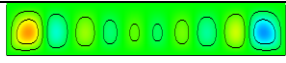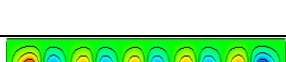
---

[*] Corresponding authors: r.minea@rdslink.ro; andra.tamas@upt.ro

cylinders or to just one. In such cases, the flow regime may be defined by the Taylor number (which represents the rate between the centrifugal force and the viscous drag force, rel.1) or Taylor-Reynolds (rel.2) number considering the geometrical customization and physical properties of the fluid respectively dynamic (η) or kinematic (ν) viscosity and the liquid density (ρ). The submitted relations are specific to Taylor-Couette flow, including the movement of fluid through the ring-shaped space of rotational viscometer Rheotest or Couette flow used for a wide range of liquids [1-4].

$$Ta = \text{Re}^2 \cdot \frac{\delta}{r} = \frac{\Omega^2 \cdot r_i \cdot \delta^3}{\nu^2} = \frac{4 \cdot \pi^2 \cdot n^2 \cdot r_i \cdot \delta^3 \cdot \rho^2}{\eta^2} \qquad (1)$$

$$Ta_{\text{Re}} = \frac{\Omega \cdot r_i \cdot (r_o - r_i)}{\nu} = \frac{2 \cdot \pi \cdot n \cdot r_i \cdot \delta \cdot \rho}{\eta} \qquad (2)$$

Based on these expressions, the critical regime for Taylor number is considered $Ta_{cr} = 1700$ [5-7], and for Taylor-Reynolds number $Ta_{\text{Re},cr} = 60$. By overcoming the critical regime, in liquid are formed toroidal or spiral vortices which increases with the increasing of turbulence (figure 1a,b), phenomenon called "instability of Couette-Taylor flow"[6]. The formation of these vortices is explained by the increase of the dynamic pressure of the fluid (p_{dyn}) which can be much higher than the shear stress of the layers (τ_f).

a. Toroidal vortices in ring-shaped space [5]		b. Evolution of toroidal vortices depending on the length of the ring-shaped space and the hydrodynamic regime [5]	
		Vortices in the end zone at overcoming critical regime	
		Vortices in evolution on the entire length of the ring-shaped channel	
		Vortices developed in turbulent flow	

Fig. 1. a, b. Illustration of the vortices when the liquid flows through ring-shaped spaces.

2. Experimental

Reagents

The main characteristics of the analyzed liquids as well as the operating conditions are given in table 1.

The characteristics of the analyzed samples

Sample	Liquid	Density (kg/m^3)	Viscosity (Pa.s)	Temperature (°C)	Ring-shaped space (mm)	
					r_i	δ
I	Ethylene glycol EG	1114	0.0171	25	19.6	0.5
II	Transformer oil TO	880	0.0168	25	19.6	0.5
III	Magnetic fluid-TO	1035	0.0380	20	19.6	0.5
IV	Magnetic fluid-petroleum	1080	0.0048	20	19.6	0.5
V	Glycerine	2120	0.0779	25	19.6	0.5
VI	Additivated castor oil[*]	921	0.1696	50	19.6	0.5
VII	Glycerine	2120	0.0779	25	40.0	2.0

[*] 7 wt.% pyromellitic ester

Methods

To assess the flow of liquids through ring-shaped spaces it was used a rotational viscometer Rheotest with metallic coaxial cylinders, respectively, a modified Couette type viscometer with glass cylinders. At Rheotest viscometer the inner cylinder with radius r_i=19.6 mm is rotatable and the outer cylinder is fixed and has the radius r_o=20.1 mm, so that the thickness of the ring-shaped space is δ=r_o-r_i=0.5 mm. Samples analyzed with Rheotest viscometer have been I-VI.
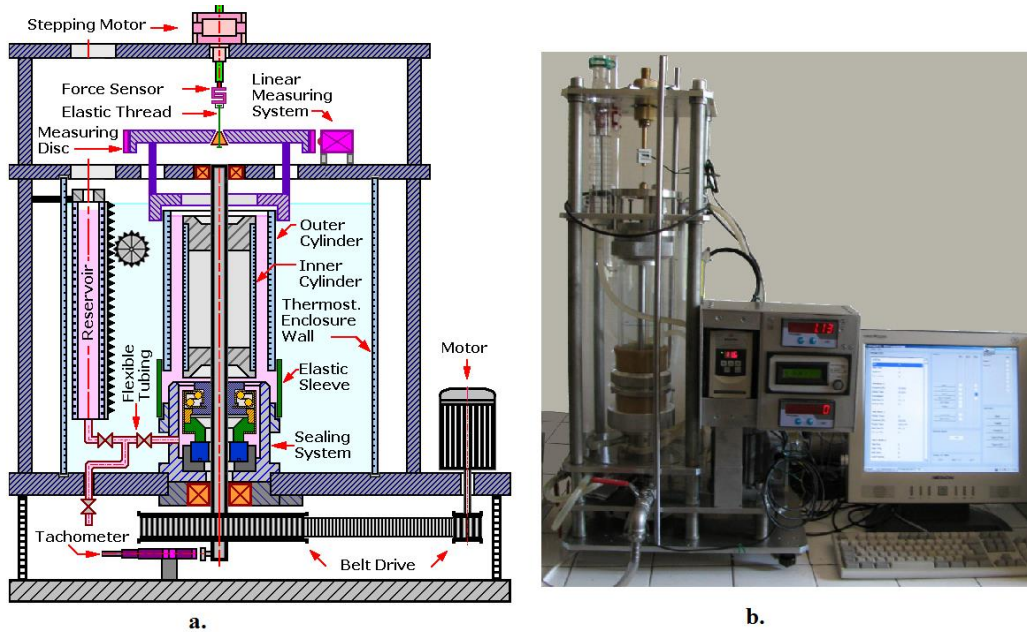

Fig. 2. a. The scheme of modified Couette viscometer, **b.** The experimental set up.

Couette-type viscometer, (fig. 2a, b), have radii of the cylinders r_i=40 mm and r_o=42 mm, respectively, the thickness of ring-shaped space δ=r_o-r_i=0.5 mm. The cylinders are made of Duran glass to enable viewing the flow phenomena. The inner cylinder rotates at a revolution that can be adjusted by means of a frequency converter in the range 1÷120 Hz, with the step 0.1 Hz. To measure the revolution, on the axis of rotation is mounted a cam plate (to amplify the number of pulses) which rotates in front of a proximity detector connected to a pulse counter with digital output signal and an interface that allows the connection to a computer. By means of the torsion moment it is calculated the shear rate [8-10].

3. Results and discussions

The study of fluid motion in ring-shaped space was carried out for liquids with different viscosities and Newtonian behavior (EG [11], aqueous solutions of glycerine [8-10], mineral and paraffin oil [11], magnetic fluids, castor oil additivated with pyromellitic esters [12]). Using the revolution of the inner cylinder it was calculated the dynamic pressure of the liquid, considering the average speed of layers in contact with the two cylinders, according to the relations (3):

$$w_{med} = \frac{1}{2} \cdot (w_i + w_o) \, ; \; w_i = \Omega_i \cdot r_i = 2\pi \cdot r_i \cdot n \, ; \; w_o = 0 \, ; \; p_{dyn} = \frac{\rho \cdot w_{med}^2}{2} \qquad (3)$$

The ratio of shear stress and dynamic pressure τ_f / p_{dyn} is a direct measure of the increase of centrifugal or inertial forces in correlation with the viscous friction force, depending on the Taylor-Reynolds number Ta_{Re}. In the graphical representation of rel. (4a) the dependence is parabolic (figure 3). Logarithmic representation of rel.(4b) is a right line whose slope tends to the unitary value, the dependence being inverse proportional (figure 4):

$$\tau_f / p_{dyn} = f(Ta_{Re}) \, ; \; \ln(\tau_f / p_{dyn}) = a \cdot \ln Ta_{Re} + b \, ; \qquad (4a, b)$$

$$\ln(\tau_f / p_{dyn}) = b^* - \ln Ta_{Re} \qquad (4c)$$

94
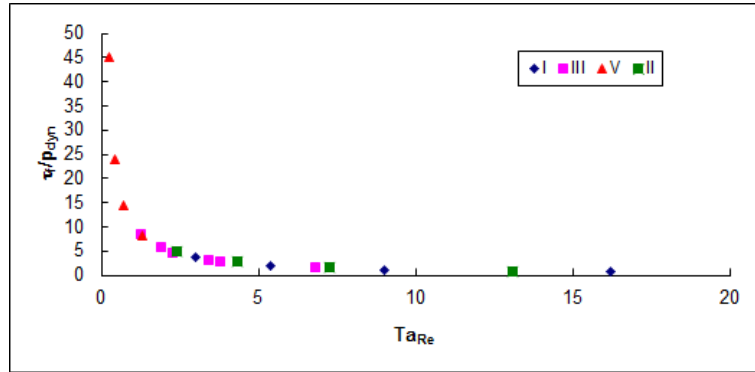
Fig. 3. $\tau / p_{dyn} = f(Ta_{Re})$ dependence for the analyzed samples.

Fig. 4. $\ln(\tau / p_{dyn}) = f(\ln Ta_{Re})$ dependence for the analyzed samples.

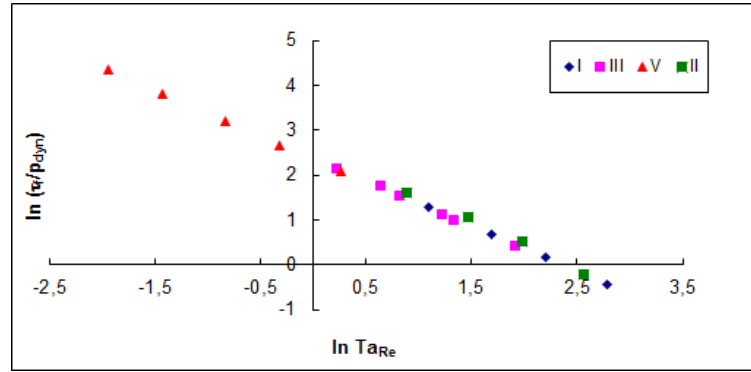Taking into account the condition of equality between shear stress and dynamic pressure ($\tau_f / p_{din} = 1$, or $\ln(\tau_f / p_{din}) = 0$) the equilibrium value of Taylor-Reynolds number, Ta_{Re}^*, can be determined. This ratio, that can be also deduced through calculation, is smaller than the critical value $Ta_{Re,cr}$ established, based on the observations related to the vortices appearance. Hydrodynamic ratio, Ta_{Re}, ranging between the equilibrium and the critical value, indicates that the dynamic pressure may exceed, with a certain threshold, the value of shear stress so that the appearance of vortices and turbulence might be possible.

In table 2 were exemplified these calculations for the flow of ethylene glycol (Sample I) into the ring-shaped space of the rotational viscometer Rheotest, at a temperature of 25 °C. For the studied liquids it is presented the range of variation of the main measures taken into account, as well as the obtained values for the number Ta_{Re}^*.

Table 2

Representative values measured and calculated for the ethylene glycol flow

n (s^{-1})	τ_f (Pa)	p_{dyn} (Pa)	τ_f/p_{dyn}	ln τ_f/p_{dyn}	Ta_{Re}	ln Ta_{Re}
0.75	4.3	1.18	3.64	1.29	3.01	1.10
1.35	7.4	3.83	1.93	0.66	5.41	1.69
2.25	12.5	10.6	1.18	0.16	9.02	2.20
4.05	22.5	34.4	0.65	-0.43	16.2	2.79

As it is shown in table 3, on the whole, the field of working/variation of range for Ta_{Re} number was between 0.02 and 57. It is also found out that representation in logarithmic coordinates (rel. 4b) is practically linear and the values of constant "a" for different samples are close to unit. It is proposed a general relationship (rel. 4c) in which the slope is established at -1 and the free term "b*" was recalculated according to this.

Table 3

The variation range of measures and the parameters of rel. (4b,c)

Sample	n (s^{-1})	τ_f (Pa)	p_{dyn} (Pa)	Ta_{Re}	Rel.4b		Rel.4c	Ta^*_{Re}
					a	b	b*	
I	0.75÷4.05	4.3÷22.5	1.1÷34.1	2.97÷16.0	-1.014	2.394	**2.36**	**10.6**
II	0.75÷4.05	4.7÷22.1	0.9÷27.2	2.42÷13.1	-1.079	2.608	**2.42**	**11.2**
III	0.75÷4.05	9.4÷48.2	1.1÷32.2	1.26÷6.80	-1.037	2.390	**2.34**	**10.4**
IV	1.35÷4.05	2.1÷6.3	3.7÷33.5	18.7÷56.1	-0.998	2.352	**2.36**	**10.6**
V	0.15÷1.35	4.0÷34.0	0.05÷4.2	0.14÷ 1.3	-1.027	2.345	**2.35**	**10.5**
VI	0.05÷1.35	2.71÷65.8	0.004÷3.17	0.02÷0.51	-1.024	2.399	**2.40**	**11.0**
VII	0.16÷0.85	2.25÷9.3	0.26÷5.4	1.1÷ 5.0	-1.073	2.240	**2.16**	**8.7**

Thus, for each substance it was obtained the equilibrium value of Taylor-Reynolds number in the range $10.4 < Ta^*_{Re} < 11.2$, for the ring-shaped space of Rheotest device (samples I-VI), the average value being 10.7. For the space of modified Couette rheometer, the value is slightly different, $Ta^*_{Re} = 8.7$.

To visualize the flow in the ring-shaped space of a modified Couette viscometer, equipped with glass cylinders, were used two miscible liquids (ethylene glycol and a colored solution) with near values for density, and, at certain revolution values and Taylor-Reynolds numbers, respectively, it was followed the evolution in time of the mixing/diffusion process. The colored solution was introduced at the top of the ring-shaped space (figure 5a) and was measured the height of mixing zone. For the revolutions corresponding to laminar regime and $Ta_{Re}=6.3$, the height dependence follows an exponential curve with decreasing tendency. Photos were made at intervals of 2 minutes. The total mixing of the two layers was achieved after eight minutes.
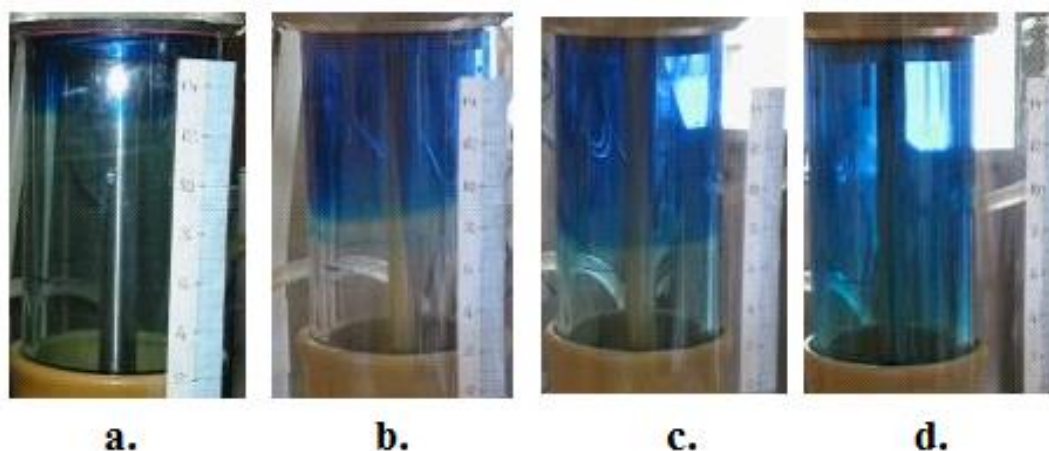
Fig. 5. a,b,c,d. Evolution of the diffusion process in time for Ta_{Re}=10.6 [8].

4. Conclusions

It was built a modified Couette rheometer for studying the flow in laminar regime, as well the visualization of the mixing of two liquids.

It was correlated the Taylor Renolds number with the ratio between shear stress and dynamic pressure for different substances.

For the equality between dynamic pressure and shear stress "Taylor-Reynolds number of equilibrium" was introduced.

REFERENCES

[1] Batten W.M.J., Bressloff N.W., Turnock S.R.*, Transition from vortex to wall driven turbulence production in the Taylor-Couette system with a rotating inner cylinder, *International Journal of Numerical Methods in Fluids*, 38, (2002), 207.

[2] Dou H.S., Khoo B.C., Yeo K.S., Instability of Taylor-Couette Flow between Concentric Rotating Cylinders, *International Journal of Thermal Science*, 47, (2008),1422.

[3] Lewis G.S., Swinney H.L., Velocity structure functions, scaling, and transitions in high Reynolds number Couette-Taylor flow*, Physical Revue E*, 59 (9), (1999), 5457.

[4] Lohse D., Crossover from high to low Reynolds number turbulence, *Physical Review Letters*, 73(24), (1994), 3223.

[5] http://en.wikipedia.org/wiki/Taylor%E2%80%93Couette_flow

[6] http://hmf.enseeiht.fr/travaux/CD0001/travaux/optmfn/hi/01pa/hyb72/tc/tc.htm

[7] McMillan D.E, Strigberger J., Utterback N.G, Blood's critical Taylor number and its flow behavior at supercritical Taylor numbers, *Biorheology,* 24(4), (1987), 401.

[8] Borş N., Contribuţii la studiul influenţei unor substanţe chimice asupra îmbunătăţirii curgerii lichidelor, Teză de doctorat, Universitatea Politehnica Timişoara, 2010.

[9] Borş N., Tămaş A., Minea R.*,* Contributions to Rheological Fluids Flow in Modified Couette Device, *Revista de Chimie*, 61(2), (2010), 218.

[10] Borş N., Tămaş A.,The testing and calibration of a rotating rheometer, *Studia Universitatis Babeş-Bolyai Chemia,* 55(3), (2010), 139.

[11] Tămaş A., Borş N., Minea R., The effect of some additives on the friction in liquids subject to rotational motion, *Buletinul Universităţii Petrol-Gaze Ploieşti, seria Tehnică*, LX (4B), 2008.

[12] Boran S., Tămaş A., Aspects of rheological behavior of castor oil additivated with mixed pyromellitic esters, *Journal of Serbian Chemical Society*, 79(2), (2014), 241.

MATHEMATICAL MODELLING OF MASS TRANSFER IN MOLECULARLY IMPRINTED POLYMERS WITH DIOSGENIN IN POLY(ACRYLONITRILE-METHACRYLIC ACID) MATRIX

Ştefan-Ovidiu DIMA[1,2], Tănase DOBRE[1*], Octavian FLOAREA[1]

[1] Depart. Chemical and Biochemical Engineering, POLITEHNICA University of Bucharest, 1-7 Gh. Polizu, 011061, Bucharest, Romania
[2] National Research and Development Institute for Chemistry and Petrochemistry ICECHIM, Bioresurses Department, 202 Splaiul Independentei, District 6, Bucharest, Romania.

Abstract

The present work is an interdisciplinary research that combines aspects from chemical engineering with aspects from polymer engineering, polymer chemistry, and analytical chemistry, all these aspects being characteristic to the field of molecularly imprinted polymers (MIPs). This work aims to complete the previous results regarding the molecularly imprinted polymers with diosgenin as template and three poly(acrylonitrile-methacrylic acid) (AN:MAA) systems as matrices. The previous studies of elemental analysis, Fourier-transform infrared spectroscopy, Raman spectroscopy, size exclusion chromatography, thermogravimetry, derivative termogravimetry, differential scanning calorimetry, and Scatchard analysis, which individually confirmed by specific means the molecular imprinting, are being completed with the current mathematical modelling studies of mass transfer in batch conditions. The adsorption dynamics data were described with the help of a phenomenological mathematical model, having the parameters k_a, k_d, and D_{ef}. The parameters identification evidenced a slowly dependence of these parameters on diosgenin concentration. These parameters are higher influenced by the type of copolymer that gets into the matrix structure. The adsorption process at equilibrium derived from the developed mathematical model led to the obtaining of Scatchard relation, equation frequently used to express the equilibrium in various adsorbents. The best agreement between experimental and computed data were obtained for the MIP-AN:MAA-80:20 system.

Keywords: mathematical modelling, molecularly imprinted polymers, MIPs, diosgenin, acrylic copolymers, molecular recognition.

---

* Corresponding author: E-mail address: tghdobre@gmail.com

1. Introduction

Molecular imprinting is a big and growing research field (9108 articles and 1185 patents in May 2014) [1,2] that has its roots in the immunology area, when Breinl and Haurowitz published in 1930 a paper concerning some chemical studies on the precipitate from haemoglobin and anti-haemoglobin serum and a theory regarding the nature of the antibodies [3]. The theory took shape in 1940 with the work of Linus Pauling, who considered that antibodies adopt a specific three-dimensional complementary structure toward the antigen upon contact with it [4]. This theory surpassed the boundaries of biology and inspired Frank H. Dickey to create, in 1949, adsorbents with specific affinities for predetermined substances [5]. Since then, the field of molecularly imprinting is exponentially growing, reaching 1012 papers in 2013. The target molecules, the molecular imprinted matrices, and the application fields are continuously improving and diversifying [6-12]. Nevertheless, the mathematical modelling studies of mass transfer in molecularly imprinted polymers (MIPs) are still underrepresented. That is why the present work aims to enrich the direction of mathematical modelling in MIPs. Previous mathematical models were applied for mass transfer in chromatographic columns [13], for nickel ion-imprinted membrane [14], and for hydrogels imprinted with 5-fluorouracil [15].

The aim of the present work is to complete the previous results regarding the MIPs obtained for diosgenin by phase inversion using three poly(acrylonitrile-methacrylic acid) systems as matrices [16].

2. Materials and methods

Adsorbate

The adsorbate for the batch adsorption experiments was diosgenin, a steroidal saponin with anti-tumoral [17-19], anti-leukemia [20], hypocholesterolemic [19,21] and estrogenic properties [22,23]. It is found in a variety of plants, having a robust molecule, molar mass of 414.62 g/mol, two hydroxyl functional groups, and two oxygen atoms in heterocycles. These functional groups was found to facilitate the molecular imprinting in by creating non-covalent bounds, like hydrogen bonds, hydrophobic, and/or van der Waals interactions with the matrix's functional groups [24-26].

Adsorbents

As adsorbents in the batch adsorption experiments were used three MIP systems (MIP-AN:MAA-90:10, MIP-AN:MAA-80:20, and MIP-AN:MAA-70:30) and the corresponding NIP systems (non-imprinted polymers), meaning same matrices,

but in the absence of template and encoded NIP-AN:MAA-90:10, NIP-AN:MAA-80:20, and NIP-AN:MAA-70:30. All these adsorbents, MIPs and NIPs, were prepared by an alternative imprinting method called phase inversion, which was described in previously published work.

Characterisation methods

MIPs can be characterized by extremely diverse methods, from thermal analyses to spectroscopy, gas and liquid chromatography, mass spectrometry, microscopy, to electrochemical methods [1,2,27-33]. In the previous work [16], the obtained selective (MIPs) and non-selective (NIPs) materials were characterised by elemental analysis, Fourier-transform infrared spectroscopy, Raman spectroscopy, size exclusion chromatography, thermogravimetry, derivative termogravimetry, differential scanning calorimetry, and Scatchard analysis. Briefly, the elemental analysis proved that the experimental results for the elemental composition are closed to the theoretical ones, which suggests that the copolymerization occurred in good conditions and that the template is present in MIPs before extraction and disappears after the extraction with ethanol.

The attenuated total reflection spectroscopy (ATR-FT-IR) evidenced characteristic peaks at 2860 cm^{-1}, 2244 cm^{-1}, 1727 cm^{-1}, 1211 cm^{-1}, and 1167 cm^{-1}[16]. The wavelength 2860 cm^{-1} corresponds to associated $-O-H$ stretching vibration and is characteristic for diosgenin and suggests also possible intramolecular H-bonds between the template and the copolymer matrix. The wavelength 2244 cm^{-1} corresponds to $-C\equiv N$ stretching vibration and at this wavelength the absorbance is higher in NIPs and extracted MIPs then it is in MIPs, signifying that the nitrile groups are more free to move and vibrate than they are in MIPs, and that confirms the imprinting mechanism, when the nitrile functional groups make hydrogen bonds with template's hydroxyl groups. The region 1727 cm^{-1}, 1211 cm^{-1}, and 1167 cm^{-1} is characteristic to C=O and C$-$O stretching vibrations and is extremely active, signifying that the -COOH functional groups, present in the methacrylic segments, interact with the template's -OH functional groups. So ATR-FT-IR analyses evidenced that in the imprinting process, both types of matrix's functional groups, $-C\equiv N$ and $-COOH$, are being involved, fact that increases the quality of molecular imprinting and, subsequently, the affinity for the template.

The Raman analyses evidenced hydrogen and van der Waals interactions between diosgenin and the matrix's functional groups, fact visible in the area 1200 − 2000 cm^{-1}. After diosgenin is extracted with ethanol, the extracted MIPs had similar spectrum as the non-imprinted materials (NIPs).

Batch adsorption method

The batch adsorption method was accomplished as previously described [16] and, briefly, consisted in contacting imprinted and the corresponding non-imprinted pearls with five diosgenin solutions of known concentration. The concentrations in liquid were determined through high performance liquid chromatography by correlating the peak areas with the calibration curve obtained with known diosgenin concentrations. The adsorption results were expressed as incipient study in the form of Scatchard diagram, which was further used to calculate the adsorption parameters of MIPs and NIPs. The adsorption and desorption studies evidenced that diosgenin attached to the matrix using its free −OH functional group and that the bounds are non-covalent and reversible. They break in the extraction conditions, ethanol at high temperature (60ºC), and re-establish in adsorption conditions (room temperature, batch contacting with concentrated solutions).

The main conclusion of the previous studies was that the adsorption properties and the affinity for the template, expressed as the imprinting factor (IF), decreased in the order MIP-AN:MAA-80:20 > MIP-AN:MAA-90:10 > MIP-AN:MAA-70:30, suggesting that the ratio 80:20 is the optimized solution between high affinity and low resistance, given by the MAA segments, and low affinity and high resistance, given by the AN segments. As continuation of the previous work, the adsorption results are in depth studied in the present work by mathematically modelling the batch adsorption process in diosgenin-MIPs with AN:MAA matrix.

Mathematical modelling

In batch contacting liquid-MIP, the frequently used models for sorption dynamics characterization are based on pseudo first-order rate equation and pseudo-second-order rate equation [34-36].

The phenomenological modelling of batch sorption dynamics for one or more components is not a simple problem due to the complexity of the equations and constraints system that characterize this process [37-39]. Considering the experiments reported above, it can be proposed the following descriptive model: i) inside of one pearl, diosgenin diffuses and interacts with the pearl's binding sites; ii) as long as in the site vicinity the equilibrium misses, the interaction occurs by species binding or releasing; ii) at the pearl surface vicinity, the liquid is vigorously stirred and, consequently, the mass transfer resistance is negligible. For passing from the descriptive model to process, the mathematical model it also assumes: a) the pearls (adsorbent particles) have a porous, non swelling, structure, with the same equivalent radius (*R*); b) the overall adsorption rate of diosgenin depends on the competition between the adsorption and the desorption processes; c) the kinetics of adsorption process is linear with respect to free pores surface and

species concentration in liquid phase; d) the diosgenin desorption kinetics is linear with respect to species concentration in solid phase; e) isothermal conditions are assumed for phases contacting; f) a formal multicomponent species sorption is considered with the model equations. Based on these considerations, the following system of equations and restrictions results as the mathematical model of the adsorption process:

- diosgenin or other species conservation in the liquid inside the spherical, porous, adsorbent pearl;

$$\frac{\partial c_i}{\partial \tau} = D_{ef,i}\left(\frac{\partial^2 c_i}{\partial r^2} + \frac{2}{r}\frac{\partial c_i}{\partial r}\right) - v_{Ri}(c_i, c_{si}) \qquad i = 1,2.,N \tag{1}$$

- diosgenin or other species balance equation, in respect to the solid phase (pearls);

$$\frac{\rho_P}{\varepsilon_P}\frac{\partial c_{si}}{\partial \tau} = v_{Ri}(c_i, c_{si}) \qquad i = 1,2.,N \tag{2}$$

- the rate equation describing the species adsorption kinetics;

$$v_{Ri}(c_i, c_{si}) = k_{ai}(1 - \frac{\sum\limits_{i=1}^{N}\alpha_i c_{si}}{Q})c_i - k_{di}\frac{\rho_P}{\varepsilon_P}c_{si} \qquad i = 1,2.,N \tag{3}$$

- interphase species transfer rate at pearl's surface;

$$-V_l\frac{dc_{li}}{d\tau} = m_s\frac{dc_{si\,mn}}{d\tau} \qquad i = 1,2.,N \tag{4}$$

- the instantaneous mean concentration of i species in solid phase:

$$c_{si,mn}(\tau) = \frac{1}{R}\int_0^R c_{si}(r,\tau)dr \tag{5}$$

- initial conditions for the concentration field in the solid and liquid phases:

$$\tau = 0 \qquad 0 \le r < R \qquad c_i = 0, \quad c_{si} = 0$$
$$\tau = 0 \qquad\qquad r > R \qquad c_{li} = c_{li0}, \qquad\qquad i = 1,2.,N \tag{6}$$

- boundary conditions for species diffusion inside the porous pearl:

$$\tau > 0 \qquad\qquad r = 0 \qquad \frac{dc_i}{dr} = 0, \ \frac{dc_{si}}{dr} = 0$$

$$\tau > 0 \qquad\qquad r = R \qquad V_l\frac{dc_{li}}{d\tau} = -D_{efi}S\left(\frac{dc_i}{d\tau}\right) \qquad i = 1,2.,N \tag{7}$$

The mathematical model {equations and restrictions (1)-(7)} was numerically transposed through an adequate finite differences method in a parameters identification problem. Further, the computed values of the instantaneous mean concentration of species in liquid phase, $c_{li,}$ (τ), which depend on known parameters, namely R, ε_P, ρ_P, α_i, Q, $c_{i0,}$ c_{li0} (see *table 1*), and on the unknown parameters $D_{ef,i}$, k_{ai}, k_{di}, are expressed relative to the measured mean concentration of species in liquid phase, given by equation (8), fact that produces the identification of D_{efi}, k_{ai} and k_{di}. Here $c_{li,exp}(\tau_j)$ is the experimental concentration of i species in liquid phase at time τ_j.

$$f_i\left(D_{ef,i}, k_{ai}, k_{di}\right) = \sum_j \left[c_{li,mn}(\tau_j) - c_{li,\exp}(\tau_j)\right]^2 \quad i = 1, 2., N \tag{8}$$

A procedure inspired by the stochastic algorithm for multiparameters optimization problem [40] has been used in order to obtain the minimization of the functional (8) after species effective diffusion coefficient, process adsorption constant, and, respectively, process desorption constant. It contains the following steps: 1) Choosing a start point; 2) Minimizing the functional after D_{ef} parameter; 3) Changing the start point by considering the identified values of the effective diffusion coefficient; 4) Minimizing the functional after k_a; 5) Changing the start point by considering the identified value of k_a; 6) Minimizing the functional after k_d; 7) Verifying the covering of the experimental considered c_l dynamics. The *figure 1* illustrates this minimization procedure.
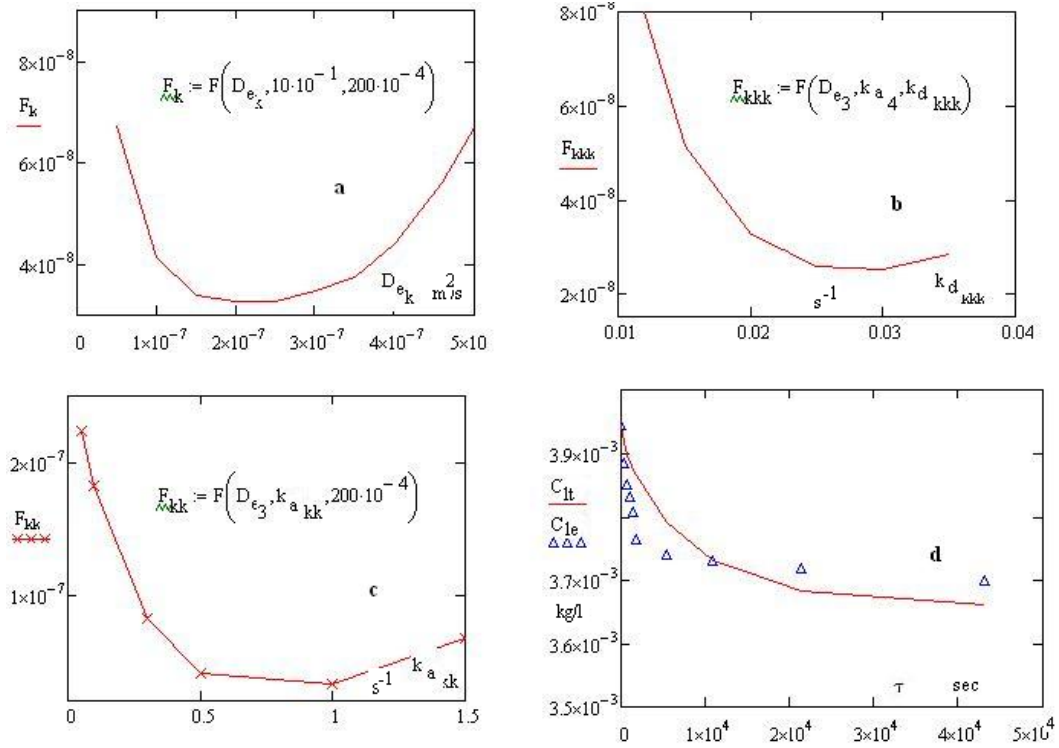
Table 1

The known parameters for model of species adsorption in MIP-AN:MAA pearls

	Parameter	Symbol	Value	Unit	Source
1	Pearl radius	R	0.05	cm	experimental
2	Pearl density	ρ_P	0.55	g/cm^3	experimental
3	Pearl porosity	ε_P	0.34	cm^3/cm^3	established from ρ_P
4	Adsorption pearl capacity	Q	0.05	g$_D$/g	initial diosgenin concentration in pearls
5	Mass of pearls in batch	m_s	1	g	experimental
6	Liquid volume in batch	V_l	80	cm^3	experimental
7	Initial liquid species concentration	C_{l0}	0.0007j, j=1,..5	g$_D$/g$_{lq}$	experimental

3. Results and discussions

The results of mathematical modelling of mass transfer in molecularly imprinted polymers with diosgenin in poly(acrylonitrile-methacrylic acid) matrix are presented in the following figures and tables.

Fig. 1. Minimization of the functional (8) with the start point $(5 \cdot 10^{-7}, 10 \cdot 10^{-1}, 2 \cdot 10^{-2})$: a) after D_e, b) after k_d, c) after k_a, d) experimental and model computed c_l dynamics.

For all tested systems of diosgenin MIPs are presented, under the form of *table 2*, the results of D_{ef}, k_a, k_d identification. As it was expected, it has been obtained a slowly dependence of these parameters on diosgenin concentration. An important influence on these parameters was obtained related to the copolymers' type. So, for each imprinted polymer type it was considered as representative the mean values of D_{ef}, k_a and respectively k_d.

The above considerations can be proposed based on these identified values: i) the diminishing of MAA content in the basic copolymer reduces the pore radius and pearl porosity and increases the pore tortuosity; this fact is sustained by the decreasing of effective diffusion coefficient ($D_{ef} = \varepsilon D_m / \xi$) from MIP-AN:MAA-70:30 ($6 \cdot 10^{-7}$ cm^2/s) to MIP-AN:MAA-90:10 ($2 \cdot 10^{-7}$ cm^2/s); ii) D_{ef} has the magnitude order of diffusion processes in porous solids with micronic pores [37,38]; iii) the evolution of k_a and k_d with copolymer type shows that the type MIP-AN:MAA-80:20 is the most favourable for diosgenin adsorption (it shows that the ratio between k_a for the MIP-AN-MAA-80:20 and the others give the values 3.2 and respectively 4); iv) the computation, for each tested MIP, of deviation from the mean value of D_{ef}, k_a and respectively k_d shows that the

smallest deviation from the mean are seen for the case of MIP-AN:MAA-80:20; the *figures 2-4* sustain this observation.

Table 2

Results of D_{ef}, k_a, k_d for diosgenin adsorption by MIP-AN:MAA systems for five concentrations (0.1, 0.2, 0.3, 0.4, and 0.5%)

|	Adsorbent code-sol.conc.	D_{ef} 10^6 (cm^2/s)	k_a 10^1 (s^{-1})	k_d 10^4 (s^{-1})
1	MIP-AN:MAA-70:30-0.1	0.80	15	250
2	MIP-AN:MAA-70:30-0.2	0.60	10	200
3	MIP-AN:MAA-70:30-0.3	0.50	10	200
4	MIP-AN:MAA-70:30-0.4	0.60	5	100
5	MIP-AN:MAA-70:30-0.5	0.50	10	150
Mean value		**0.60**	**10**	**180**
6	MIP-AN:MAA-80:20-0.1	0.40	40	150
7	MIP-AN:MAA-80:20-0.2	0.30	30	100
8	MIP-AN:MAA-80:20-0.3	0.30	30	100
9	MIP-AN:MAA-80:20-0.4	0.30	30	120
10	MIP-AN:MAA-80:20-0.5	0.30	30	150
Mean value		**0.32**	**32**	**120**
11	MIP-AN:MAA-90:10-0.1	0.20	10	230
12	MIP-AN:MAA-90:10-0.2	0.30	10	200
13	MIP-AN:MAA-90:10-0.3	0.15	10	300
14	MIP-AN:MAA-90:10-0.4	0.15	5	150
15	MIP-AN:MAA-90:10-0.5	0.20	10	300
Mean value		**0.20**	**8**	**240**

Related to the *figures 2-4*, it was shown that the selection of c_l/c_{10} axis seems to emphasize the differences between the three tested MIP systems. The large scattering of experimental points in *figures 2 and 4* is a consequence of this selection. If it is calculated the relative deviation of all experimental values c_l/c_{10} ratio to those obtained with the model with identified parameters, then are found values not higher that 6.5%.

The extension of the above presented model to the equilibrium state reveals that overall adsorption rate undergoes to very low or zero values when the adsorption process rate becomes equal with desorption processes rate. For the case of monocomponent sorption, adding this last observation inside of relation (3) leads to relation (9). Scatchard equilibrium expression is easily obtained by processing the relation (9). This processing leads to relation (10) which is the most known Scatchard equilibrium expression. Initially, this expression has been developed to characterise the reversible combination of small ions or molecules with specific sites on the surface of a protein or other biopolymer. Now the Scatchard equilibrium expression is used in many cases of liquid - solid equilibrium. The
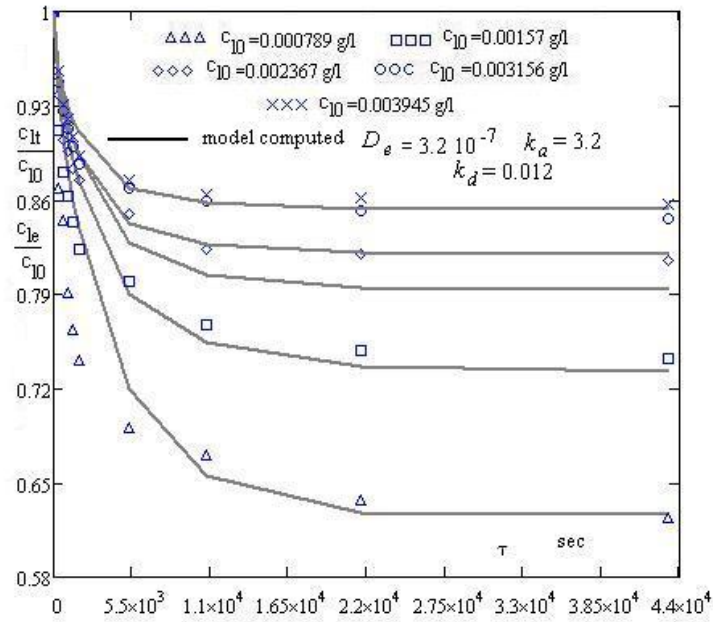
equilibrium liquid – adsorbent for imprinted polymer is part of these cases [41-43].

$$c_l^* = \frac{k_d \dfrac{\rho_p}{\varepsilon} c_s}{k_a \left(1 - \dfrac{c_s}{Q}\right)} \tag{9}$$
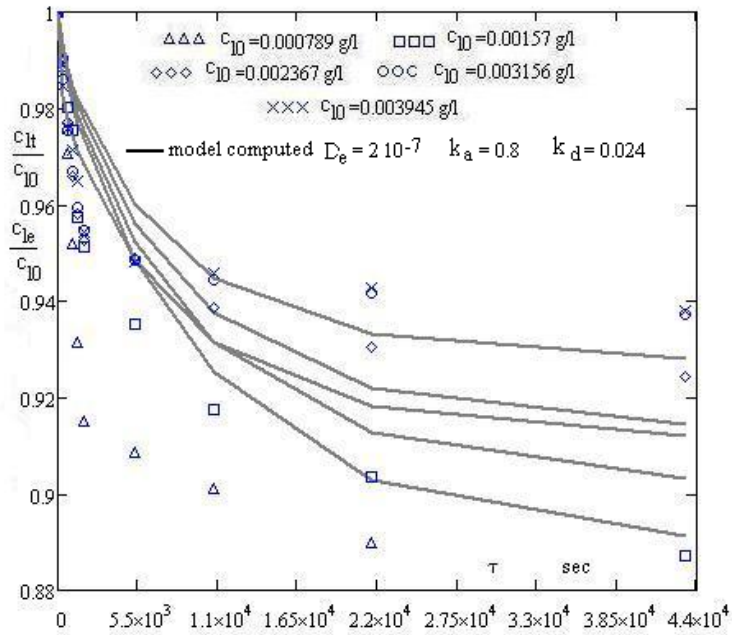
$$\frac{c_s}{c_l^*} = \frac{k_a}{k_d \dfrac{\rho_p}{\varepsilon}} - \frac{k_a}{k_d \dfrac{\rho_p}{\varepsilon} Q} c_s \tag{10}$$
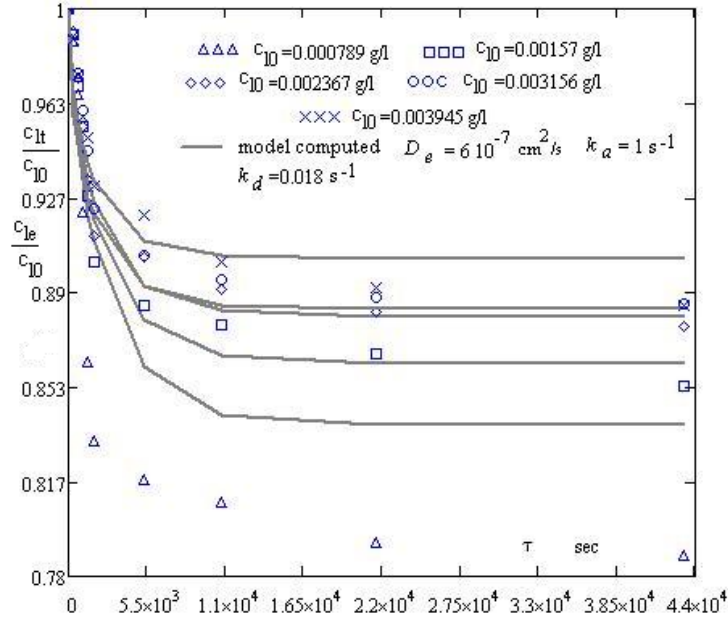
Fig. 2. Dispersion of experimental adsorption dynamics data around the model's computed data with the identified parameters (for MIP-AN:MAA-70:30).

Fig. 3. Dispersion of experimental adsorption dynamics data around the model's computed data with the identified parameters (for MIP-AN:MAA-80:20).
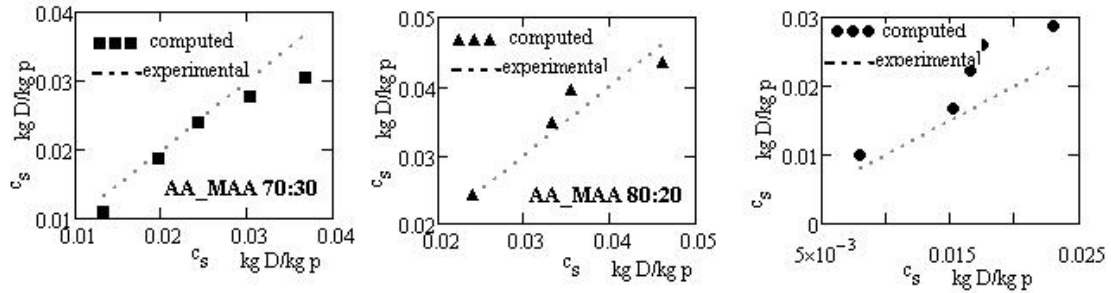

Fig. 4. Dispersion of experimental adsorption dynamics data around the model's computed data with the identified parameters (for MIP-AN:MAA-90:10).

Fig. 5. Comparison between experimental values and those calculated using the relation (9) for equilibrium concentration of diosgenin in solid phase (tested MIPs with k_a and k_d from *table 2* and with Q=0.05).

By mean of *figure 5* it is shown that for the system MIP-AN:MAA-80:20, a very good agreement between experimental and computed values of solid phase diosgenin concentration has been obtained. The differences that occur in the case of MIP-AN:MAA-70:30 system and respectively MIP-AN:MAA-90:10, can be attributed to the fact that for diosgenin imprinted systems, a part of this template has been physically irreversible bound. In these two cases the diminishing, under 0.05, of Q in relation (9) is better approaching the c_s calculated and experimental values.

4. Conclusions

The MIP pearls, developed from the three AN:MAA systems with diosgenin as template, were successfully prepared by phase inversion. Based on analytical proofs previously obtained, which confirmed the interaction between diosgenin and the specific molecular sites from the AN:MAA matrix, the study of mass transfer in D-MIPs was developed. The isothermal batch adsorption of diosgenin from alcoholic solutions on three types of D-MIP AN:MAA adsorbents has shown that the MIP adsorbent type AN:MAA-80:20 is the most efficient. A phenomenological mathematical model, with k_a, k_d and D_{ef} as parameters, has been considered to capitalize data characterizing the adsorption dynamics for the experimentally investigated cases. The identification of model parameters has revealed, as it was expected, a slowly dependence of these parameters on diosgenin concentration. An important influence on these parameters is obtained related to the copolymers type and, consequently, each MIP system has been characterized by its k_a, k_d and D_{ef} values. The adsorption process at equilibrium derived from the developed mathematical model led to the Scatchard relation which has been tested to compare the computed and experimentally obtained diosgenin concentrations at equilibrium, bound by the MIP systems. A good agreement has been obtained for the MIP-AN:MAA-80:20 system.

REFERENCES

[1]   Whitcombe M.J., Kirsch N., Nicholls I.A., Molecular imprinting science and technology: a survey of the literature for the years 2004-2011. *Journal of Molecular Recognition*, 27 (6), (2014), 297.

[2]   Alexander C., Andersson H.S., Andersson L.I., Ansell R.J., Kirsch N., Nicholls I.A., O'Mahony J., Whitcombe M.J., Molecular imprinting science and technology: a survey of the literature for the years up to and including 2003. *Journal of Molecular Recognition*, 19 (2), (2006), 106.

[3]   Breinl F., Haurowitz F., Chemical examinations on the precipitate from haemoglobin and anti-haemoglobin serum and comments on the nature of antibodies. *Hoppe-Seylers Zeitschrift für Physiologische Chemie*, 192 (45), Strassburg: K.J. Trübner, 1930.

[4]   Pauling L., A theory of the structure and process of formation of antibodies. *Journal of the American Chemical Society*, 62 (10), (1940), 2643.

[5]   Dickey F.H., The preparation of specific adsorbents. *Proceedings of the National Academy of Sciences of the United States of America*, 35 (5), (1949), 227.

[6]   Dima S.O., Meouche W., Dobre T., Iordache T.V., Sarbu A., Diosgenin-selective molecularly imprinted pearls prepared by wet phase inversion. *Reactive and Functional Polymers*, 73 (9), (2013), 1188.

[7]   Dima S.O., Sarbu A., Dobre T., Chetraru O., Nicolae C.A., Spataru C., Molecularly imprinted poly(acrylonitrile-co-acrylic acid) matrix with sclareol. *Polymer Engineering and Science*, DOI 10.1002/2013.pen.23689, Wiley, 2013.

[8]   Dima S.O., Bioengineered polymers to mimic anti-bodies' molecular recognition. *Current Opinion in Biotechnology*, 24 (1), (2013), 63.

[9]   Titirici M.M., Sellergren B., Thin molecularly imprinted polymer films via reversible addition-fragmentation chain transfer polymerization. *Chemistry of Materials*, 18 (7), (2006), 1773.

[10] Yoshikawa M., Tanioka A., Matsumoto H., Molecularly imprinted nanofiber membranes. *Current Opinion in Chemical Engineering*, 1 (1), (2011), 18.

[11] Schirhagl R., Bioapplications for Molecularly Imprinted Polymers. *Analytical Chemistry*, 86 (1), (2014), 250.

[12] Nicolescu T.V., Sarbu A., Dima S.O., Nicolae C., Donescu D., Molecularly imprinted "bulk" copolymers as selective sorbents for gallic acid. *Journal of Applied Polymer Science*, 127 (1), (2013), 366.

[13] Szabelski P., Kaczmarski K., Phenomenological modeling of separation of enantiomers by nonlinear chromatography. *Acta Chromatographica*, 20 (4), (2008), 513.

[14] Salehi E., Madaeni S.S., Vatanpour V., Thermodynamic investigation and mathematical modeling of ion-imprinted membrane adsorption. *Journal of Membrane Science*, 389 (1), (2012), 334.

[15] Wentao K., Xin L., Mathematical modeling and sustained release property of a 5-fluorouracil imprinted vehicle. *European Polymer Journal*, 49 (12), (2013), 4167.

[16] Dima S.O., Sarbu A., Dobre T., Purcar V., Nicolae C.A., Diosgenin selective molecularly imprinted polymers with acrylonitrile-methacrylic acid matrix. *Materiale Plastice (Bucharest, Rom.)*, 49 (2), (2012), 106.

[17] Lepage C., Léger D.Y., Bertrand J., Martin F., Beneytout J.L., Liagre B., Diosgenin induces death receptor-5 through activation of p38 pathway and promotes TRAIL-induced apoptosis in colon cancer cells. *Cancer Letters*, 301 (2), (2011), 193.

[18] Chang H.Y., Kao M.C., Way T.D., Ho C.T., Fu E., Diosgenin suppresses HGF-induced epithelial-mesenchymal transition by down-regulation of MDM2 and vimentin. *Journal of agricultural and food chemistry*, 59 (10), (2011), 5357.

[19] Chiang C.T., Way T.D., Tsai S.J., Lin J.K., Diosgenin, a naturally occurring steroid, suppresses fatty acid synthase expression in HER2-overexpressing breast cancer cells through modulating Akt, mTOR and JNK phosphorylation. *FEBS Letters*, 581 (30), (2007), 5735.

[20] Liu M.J., Wang Z., Ju Y., Wong R.N.S., Wu Q.Y., Diosgenin induces cell cycle arrest and apoptosis in human leukemia K562 cells with the disruption of Ca^{2+} homeostasis. *Cancer Chemotherapy and Pharmacology*, 55 (1), (2005), 79.

[21] Juarez-Oropeza M.A., Diaz-Zagoya J.C., Rabinowitz J.L., In vivo and in vitro studies of hypocholesterolemic effects of diosgenin in rats. *International Journal of Biochemistry*, 19 (8), (1987), 679.

[22] Zhai C., Lu Q., Chen X., Peng Y., Chen L., Du S., Molecularly imprinted layer-coated silica nanoparticles toward highly selective separation of active diosgenin from Dioscorea nipponica Makino. *Journal of Chromatography A*, 1216 (12), (2009), 2254.

[23] Komesaroff P.A., Black C.V., Cable V., Sudhir K., Effects of wild yam extract on menopausal symptoms, lipids and sex hormones in healthy menopausal women. *Climacteric*, 4 (2), (2001), 144.

[24] Dima S.O., Dobre T., Sarbu A., Ghiurea M., Bradu C., Proofs for molecular imprinting of an acrylic copolymer by phase inversion. *Scientific Bulletin - "Politehnica" University from Bucharest, Series B*, 71 (4), (2009), 21.

[25] Dima S.O., Sarbu A., Dobre T., Bradu C., Antohe N., Radu A.L., Nicolescu T.V., Lungu A., Molecularly imprinted membranes for selective separations. *Materiale Plastice (Bucharest, Rom.)*, 46 (4), (2009), 372.

[26] Dima S.O., Dobre T., Sarbu A., Mass transfer in a special type of nanomaterials: MIPs. *Journal of Optoelectronics and Advanced Materials*, 14 (7-8), (2012), 619.

[27] Nicolescu T.V., Sarbu A., Ghiurea M., Donescu D., Influence of crosslinker/porogen ratio upon imprinted polymer parameters, *Scientific Bulletin - "Politehnica" University from Bucharest, Series B*, 72, (2011), 163.

[28] Pardeshi S., Dhodapkar R., Kumar A., Influence of porogens on the specific recognition of molecularly imprinted poly(acrylamide-co-ethylene glycol dimethacrylate). *Composite Interfaces*, 21 (1), (2014), 13.

[29] Fa H.B., Zhang H.F., Yin W., Hou C.J., Huo D.Q., Mao Y.L., Zhang J., Molecularly imprinted polymeric microspheres with metalloporphyrin-based molecular recognition sites coassembled with methacrylic acid. *High Performance Polymers*, 25 (7), (2013), 790.

[30] Richter A., Belbruno J.J., Characterization of functional states in nicotine- and cotinine-imprinted poly(4-vinylphenol) films by nanoindentation. *Journal of Applied Polymer Science*, 124 (4), (2012), 2798.

[31] Nicolescu T.V., Meouche W., Branger C., Margaillan A., Sarbu A., Fruth V., Donescu D., A new microemulsion approach for producing molecularly imprinted polymers with selective recognition cavities for gallic acid. *Polymer International*, 62 (6), (2013), 949.

[32] Cao Y., Liu L., Xu W., Wu X., Huang W., Surface molecularly imprinted polymer prepared by reverse atom transfer radical polymerization for selective adsorption indole. *Journal of Applied Polymer Science*, 131 (13), (2014), DOI: 10.1002/app.40473.

[33] Granado V.L.V., Gutiérrez-Capitán M., Fernández-Sánchez C., Gomes M.T.S.R., Rudnitskaya A., Jimenez-Jorquera C., Thin-film electrochemical sensor for diphenylamine detection using molecularly imprinted polymers. *Analytica Chimica Acta*, 809, (2014), 141.

[34] Ho Y.S., McKay G., Pseudo-second order model for sorption processes, *Process Biochemistry*, 34, (1999), 451.

[35] Ho Y.S., McKay G., The sorption of lead(II) ions on peat. *Water Research*, 33, (1999), 578.

[36] Li X., Pan J., Dai J., Dai X., Xu L., Wei X., Hang H., Li C., Liu Y., Surface molecular imprinting onto magnetic yeast composites via atom transfer radical polymerization for selective recognition of cefalexin. *Chemical Engineering Journal*, 198–199, (2012), 503.

[37] Kim H., Kaczmarski K., Guiochon G., Mass transfer kinetics on the heterogeneous binding sites of molecularly imprinted polymers. *Chemical Engineering Science*, 60 (20), (2005), 5425.

[38] Kim H., Kaczmarski K., Guiochon G., Intraparticle mass transfer kinetics on molecularly imprinted polymers of structural analogues of a template. *Chemical Engineering Science*, 61 (16), (2006.), 1122.

[39] Zhang Y.L., Zhang J., Dai C.M., Zhoua X.F., Liu S.G., Sorption of carbamazepine from water by magnetic molecularly imprinted polymers based on chitosan-Fe_3O_4. *Carbohydrate Polymers*, 97 (2), (2013), 809.

[40] Dobre T., Sanchez J.M., Chemical Engineering-Modelling Simulation and Similitude. Wiley VCH, p. 255, 2007.

[41] Pan J., Xu L., Dai J., Li X., Hang H., Huo P., Li C., Yan Y., Magnetic molecularly imprinted polymers based on attapulgite/Fe_3O_4 particles for the selective recognition of 2,4-dichlorophenol. *Chemical Engineering Journal*, 174 (1), (2011), 68.

[42] Yuan Y., Wang Y., Huang M., Xu R., Zeng H., Nie C., Kong J., Development and characterization of molecularly imprinted polymers for the selective enrichment of podophyllotoxin from traditional Chinese medicines. *Analytica Chimica Acta*, 695 (1-2), (2011), 63.

[43] Chen C.Y., Wang C.H., Chen A.H., Recognition of molecularly imprinted polymers for a quaternary alkaloid of berberine. *Talanta*, 84 (4), (2011), 1038.

STRUCTURAL PROPERTIES OF CELLULOSE REGENERATED FROM ITS IONIC LIQUID SOLUTIONS

Catalin CROITORU, Silvia F.C. PATACHIA[*]

"TRANSILVANIA" University of Brasov, Department of Product Design, Environment and Mechatronics, 29 Eroilor Str., 500036, Brasov, Romania

Abstract

In this paper, structural features of cellulose regenerated from its corresponding solutions in 1-ethyl-3-methylimidazolium acetate, 1-allyl-3-methylimidazolium chloride and 1-buthyl-3-methylimidazolium chloride ionic liquids have been assessed by FTIR spectroscopy, contact angle and methylene blue sorption studies.

Key words: Cellulose; Ionic liquids; FTIR spectroscopy; Surface energy

1. Introduction

Cellulose, as being the most widespread biorenewable and biodegradable organic polymer on earth, may overcome the negative issues regarding the environmental and economic issues that have long been associated with non-renewable energy resources and materials [1-3]. Products that are derived from cellulose have been frequently used in the wood, paper, textile, paints and lacquers industry [4-8]. However, due to its complex structure, in which hydrogen-bonded supramolecular structures bearing a great amount of inter and intramolecular bonds are formed, cellulose is practically insoluble in most conventional solvents [8]. A limited number of systems, such as concentrated ammonia, concentrated urea or sodium hydroxide aqueous solution are able to perform limited swelling of cellulose material [1, 8]. Also, it has been reported that strong acidic (phosphoric acid, sulfuric acid) are able to initiate limited cellulose dissolution, but in this case degradation of cellulose may easily occur in the presence of atmospheric oxygen or hydrolysis and/or functionalization of the polymer occurs after a limited storage period, rendering this method of dissolution less useful. In the textile industry, several dissolution and regeneration techniques have been employed, such as viscose rayon, cupramonium cellulose, and lyocell fibers [1-3]. These solvent systems currently used for cellulose dissolution suffer from drawbacks such as chemical instability and generation of toxic gaseous emissions [1, 2].

---

[*]Corresponding author: E-mail address: st.patachia@unitbv.ro (Silvia Patachia)

To date, a number of complex solvent systems, such as N-methylmorpholine-N-oxide (NMMO) and NaOH/urea have been more efficiently used in cellulose dissolution, but their use implies some drawbacks, regarding toxicity, difficulties in solvent recovery, high cost and energy consumption [2, 9]. Thus, development of an environmental friendly and economically efficient solvent for cellulosic materials is of utmost importance. Ionic liquids (ILs) are a group of new organic salts that can exist as liquids at temperatures lower than 100 ^{0}C. They have many attractive properties, such as good chemical and thermal stability, lower toxicity, non-flammability and low volatility [3, 5, 10].

Studies regarding dissolution of cellulosics in ionic liquids (especially alkylimidazolium-based ones) have indicated that their dissolution efficiency can vary considerably. Among the most efficient cellulose-dissoluting alkylimidazolium ionic liquids are included: 1-buthyl-3-methylimidazolium chloride (BMIMCl), 1-ethyl-3-methylimidazolium acetate (EMIMAc) and 1-allyl-3-methylimidazolium chloride (AMIMCl) [3, 11]. Relatively few studies have focused on characterization of cellulose regenerated from ionic liquids solutions, the most studies being focused on dissolution ability of ILs toward different sources of cellulose (often pretreated) or wood [11]. The most frequent studies have used BMIMCl as dissolution agent for cellulose, and the structural features of the regenerated cellulosic material have been determined by spectroscopic or diffraction techniques (FTIR, XRD) in conjunction with imagistic methods of analysis (SEM, AFM), that revealed modifications in lowering the crystallinity of the samples and in morphology of the regenerated material [5, 10, 12].

However, most of the studies have employed dissolution of the cellulosic material under inert atmosphere (i.e. nitrogen) [12], which can offer a somewhat different view on the properties of the regenerated material, especially when in real-life applications; atmospheric oxygen would contribute to significant structural changes.

The paper aims to complete the existing database comprehending the properties of regenerated cellulose from different alkylimidazolium ionic liquids, under different operational parameters, by studying the properties of regenerated cellulose from its solutions in 1-ethyl-3-methylimidazolium acetate, 1-allyl-3-methylimidazolium chloride and 1-buthyl-3-methylimidazolium chloride ionic liquids, obtained at 100 ^{0}C and 120 ^{0}C.

Structural modification in crystallinity, crystal axis orientation, structural transitions and potential degradation has been assessed by FTIR spectroscopy (middle infrared and near-infrared) and correlated with water sorption experiments. Oxidation has been correlated with methylene blue sorption capacity of the cellulosic material, as regarded by the reference literature [13] and the surface properties (polarity; surface formal charge) of the regenerated cellulose have been assessed by surface energy measurements.

2. Experimental

Materials

The three ionic liquids, 1-ethyl-3-methylimidazolium acetate, 1-allyl-3-methylimidazolium chloride and 1-buthyl-3-methylimidazolium chloride have been purchased from IoLiTec Ionic Liquids Technologies GmbH, Germany. The purity of the purchased ionic liquids was ≥99.5%.
As cellulose source, Whatman no.4 filter paper with 204 μm thickness and 96 g/m^2 basis weight has been used without any modifications.
Other reagents, such as methylene blue been supplied by Sigma-Aldrich and have been of analytical purity.

Obtaining of regenerated cellulose

The filter paper has been milled by using a mechanical sieve grinder in order to better facilitate its dissolution in the ionic liquids. Prior to dissolution, it has been dried for 5 hours at 105^0C, in order to eliminate water traces that could influence further experimentation.
Then, briefly, 1g of cellulose has been added to 10g of the ILs preheated at $70\ ^0C$ in a stoppered glass vial, under magnetic stirring, and thereafter the temperature has been raised to $100\ ^0C$, and $120\ ^0C$, for another set of samples, respectively.
After the complete dissolution of the cellulose material in the selected ionic liquids under continuous magnetic stirring, the obtained clear and viscous solutions have been cooled to room temperature (cca. $24\ ^0C$) following the addition of non-solvent (50 mL of distilled water). At different time intervals, a new volume of distilled water has been added, in order to facilitate the elimination of ionic liquid under a higher concentration gradient. The complete elimination of ionic liquid from the system has been monitored by electrical conductance measuring of the washing water, until electrical conductance similar to the initial distilled water has been attained.
After the removal of ionic liquids, the precipitated cellulose has been dried in a desiccator (with $CaCl_2$) for one week, until constant mass has been achieved. This drying method has been chosen in favor of traditional heating at $105\ ^0C$, due to the fact that the heating of cellulose in presence of water could promote some structural changes [13], which could be later erroneously attributed to the ionic liquid processing.
After drying, the regenerated cellulose materials have been grounded; introduced in a dye and by means of a hydraulic press pelleted at 100 atmospheres into 1 cm diameter and 3 mm thickness pellets.

The pellets have been conditioned for a week in an atmosphere having 55% relative humidity, until they reached equilibrium moisture content of 3%, and then further used in the related methods of analysis.

Methylene blue sorption tests

The amount of carboxyl groups in cellulose, formed by potential oxidation of hydroxyl groups under thermal treatment of cellulose in the presence of ILs has been determined by methylene blue sorption tests [13, 14].
A weighed cellulose sample with a known moisture content was immersed in 25 mL of aqueous methylene blue chloride solution (300 mg/L) and 25 ml of borate buffer at pH = 8.5 at 20 °C for 1 hour. Then, the immersion solution has been filtered and 5 mL of the filtrate were transferred to a calibrated flask, with 10 ml of 0.1 N HCl and subsequently filled with water up to 100 ml. The methylene blue content of the solution has been determined with a Perkin Elmer Lambda 25 UV-VIS spectrophotometer.
The carboxyl group content of the sample is obtained according to Eq. 1 [14]:

$$mmol\ COOH/g = \frac{(7.5 - m_{MB}) \times 0.0013}{m} \tag{1}$$

Where m_{MB} is the total amount of free methylene blue in the solution after absorption (mg) and m is the weight of oven-dry sample (g).
All presented values are the mean value of triplicate measurements.

Water sorption tests

The conditioned regenerated cellulose samples were immersed in closed glass recipients containing 50 mL of distilled water and their mass has been monitored at precise time intervals until a constant value has been reached (20 days).
The relative mass (Δm) gain of the regenerated cellulose at equilibrium, during water storage, has been calculated by using the following equation (Eq. 2):

$$\mathrm{D}m = \frac{\left(m_t - m_{t=0}\right)}{m_{t=0}} \cdot 100 \tag{2}$$

Where:
- m_t represents the mass of the sample at time "t" of immersion in water corresponding to equilibrium absorption;
- $m_{t=0}$ represents the mass of the conditioned sample before water immersion (at t=0)

Surface energy determinations

Contact angle measurements of the regenerated cellulose samples, by using distilled water, glycerol and ethyleneglycol as reference liquids were performed with an OCA System 20 goniometer, provided by Data Physics Co., Ltd. at 25 ^{0}C. Five different single drops of test liquid with 2 μL volume were deposited on the surface of the same specimen.

The surface energy of the wood samples has been calculated using the Lifshitz-van der Waals and Lewis Acid-Base (LW/AB) approach, with the help of the instrument's software. According to this approach, the surface energy (γ) is decomposed into a Lifshitz-van der Waals (γ^{LW}) dispersive component as well as into a polar component - γ^{p}- with Lewis acid (γ^{p+}) and Lewis base (γ^{p-}) contributions respectively (Eq.3) [15]:

$$\gamma = \gamma^{LW} + \gamma^{p} = \gamma^{LW} + 2\sqrt{\gamma^{p+} \cdot \gamma^{p-}} \tag{3}$$

The initial contact angle θ_0, which is the contact angle at the beginning of the wetting process (for $t = 0$) for the test liquids was used in the calculation of surface energy. The dispersive and polar components of the surface tension of the test liquids have been obtained from the reference literature [16]

Photographic image analysis

Color changes on precipitated cellulose were analyzed using an alternative technique to those extensively used up to this date. The novelty is that it uses photographic image analysis, rather than the use of a photocolorimeter. In the paper we have demonstrated that this technique offers good relative results, in agreement with experimental data obtained by other analysis methods, such as FTIR spectroscopy.

Photographic images of the samples irradiated at different times have been taken with the help of a Sony DSC110 digital camera (3072x2034 pixels resolution), under the same lighting conditions.

The individual images of the samples have been loaded in Adobe Photoshop and the L^*, a^*, b^* parameters using the CIELAB (8 bit) channel were determined in twenty points for each specimen, and the average value was used in further interpretations.

L^* represents the lightness and varies from 100 (white) to 0 (black) while a^* and b^* represent chromaticity indexes: $+a^*$ red, $-a^*$ green, $+b^*$ yellow, $-b^*$ blue.

The color differences were calculated using Eqs. (4)– (6) and the total color difference ΔE was calculated from Eq. (7) for each sample [17, 18].

$$DL = L_2^* - L_1^* \tag{4}$$

$$\Delta a = a_2^* - a_1^* \tag{5}$$

$$Db = b_2^* - b_1^* \tag{6}$$

$$\Delta E = \sqrt{\Delta L^2 + \Delta a^2 + \Delta b^2} \tag{7}$$

Where subscript 1 denotes the values obtained for the reference and subscript 2 denotes the values after precipitation of the cellulosic material from its corresponding ionic liquid solution.

Positive values of *Δa* describe a red shift, negative values of *Δa* a green shift, while positive values of *Δb* represent a yellow shift and negative values of *Δb* a blue shift for the color of the precipitated samples, in comparison with the reference.

FTIR spectroscopy measurements

The FT-MIR spectra of the regenerated cellulose were obtained with a Bruker-Vertex 70 Fourier transform infrared spectrometer equipped with an attenuated total reflectance (ATR) device with a resolution of 2 cm^{-1} in the 4000-400 cm^{-1} interval. The FT-NIR spectra of the same materials have been obtained in the 4500-12500 cm^{-1} range, by using the same spectrometer.

3. Results and discussions

Regarding the objective color changes determined by photographic images analysis of the samples (Fig.1), it can be observed that, generally, significant overall color changes occur (as it can be seen from the ΔE values). The highest color changes occur in samples that have been obtained by dissolution of cellulose at 120 ^{0}C, probably due to the formation of more chromophoric carboxyl/carbonyl groups on the cellulose macromolecular chains, in comparison with the samples obtained from their ionic liquid solutions at 100^{0}C.

The more significant color changes occur in the samples precipitated from their solutions in AMIMCl and EMIMAc ionic liquids, probably due to cellulose oxidation and/or functionalization, that tends to darken (as seen from the negative ΔL values) and yellow the precipitated samples, as seen from the positive values of Δb (Fig.2). BMIMCl seems to promote less extensive changes in color of the precipitated material. This may be due to the fact that oxidation of the material in BMIMCl is less pronounced.
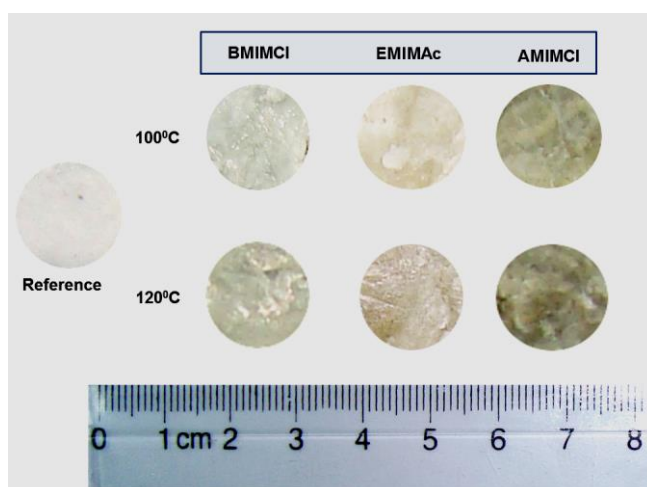
Fig.1. Photographic images of regenerated cellulose samples
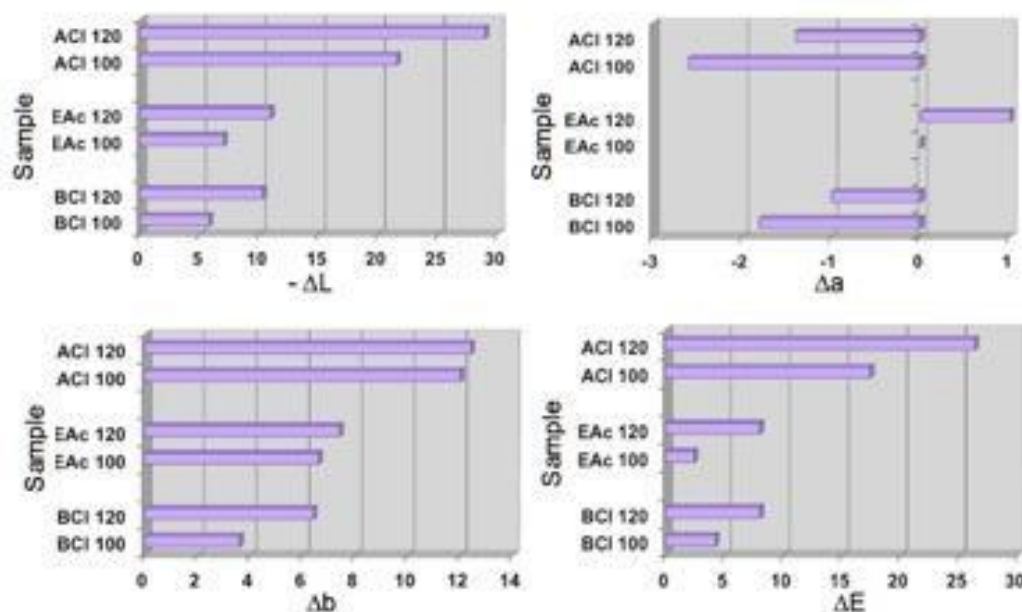
Fig.2. Photographic image analysis parameters of cellulose samples

Additional information can be also drawn from the data presented in Tab. 1, regarding the oxidation degree and the water sorption capacity of regenerated cellulose.

Table 1

Water sorption capacity and oxidation degree of the cellulose samples

Sample	Temperature treatment	Δm (%)	-COOH (mmol/g)
Reference	-	120.65	0.0417
BMIMCl	100 ^{0}C	142.48	0,0571
	120 ^{0}C	192.05	0.4937
EMIMAc	100 ^{0}C	195.84	0.0757
	120 ^{0}C	210.51	0.1608
AMIMCl	100 ^{0}C	400.66	0.2152
	120 ^{0}C	599.79	1.1726

Generally, it is observed that higher the color modifications (as seen from ΔE values in Fig.1) in the regenerated cellulose samples, higher the water sorption capacity and the carboxyl group content. So, the samples regenerated from its AMIMCl solution have the highest water sorption capacity regarding to their higher degree of oxidation that increases their hydrophylicity and also due to their lower crystallinity degree comparing to the other samples, as it will be shown from the interpretation of the FTIR spectra. Also in agreement with the total color modification parameter, BMIMCl ionic liquid seems to impart the lowest oxidation degree (and hence minor modification in color due to the formation of hydrophilic carbonyl/carboxyl groups) and water sorption capacity for the cellulose samples.

Also it can be seen that generally the samples obtained from their dissolution at 120 ^{0}C in ILs and precipitation with water bear the most pronounced modifications regarding the water sorption capacity and carboxyl groups content in comparison with the samples obtained by initial dissolution in ILs at 100 ^{0}C.

As shown in Tab.2, the total surface energy of reference cellulose ranges within the 25–60 mN/m, interval and it is mainly contributed to the LW component (non-polar), which agrees well with the results obtained for wood reported in the literature [15,16].

Regarding the regenerated cellulose it can be generally observed that the dissolution and precipitation two-phase process has a pronounced influence in increasing the wettability of the samples (higher surface energies than the reference cellulose).

The contribution of the dispersive nonpolar γ^{LW} component for the regenerated cellulose is lower, in favor of the polar γ^p component, by comparing to the reference, which clearly indicates cellulose oxidation and/or functionalization.

Since the regenerated cellulose has been pelleted in the same conditions (identic dye and applied pressure), it is to be noted that the contribution of the surface

roughness of the sample to the contact angle is less pronounced and it is appreciated that it can be ruled out from further discussions.

Also, it could be noted that the dominating contribution to the polar component of the surface energy is the Lewis base one, which means that the surface of the cellulose samples presents electron-donor properties, probably due to the presence of trace amounts of water and residual oxidation (in the case of reference) and in the case of precipitated samples due to the presence of polar and electron-donor – COO$^-$ and –C=O groups due to conjugated electromeric effects.

Table 2

Surface energies of the ionic liquid treated samples

| Sample	Temperature treatment (^{0}C)	$\theta_{0\ water}$ (degree)	γ (mN/m)	γ^{LW} (mN/m)	γ^p (mN/m)	γ^{p+} (mN/m)	γ^{p-} (mN/m)
Reference	-	63.35	27.34	16.37	10.97	2.64	11.37
BMIMCl	100 ^{0}C	62.3	36.58	17.41	19.17	1.93	47.55
	120 ^{0}C	43.45	48.37	4.97	43.4	8.42	55.91
EMIMAc	100 ^{0}C	58.25	47.16	19.36	19.36	8.90	21.70
	120 ^{0}C	39.00	51.49	2.97	48.52	8.06	73.02
AMIMCl	100 ^{0}C	40.5	50.96	47.50	3.46	0.23	12.86
	120 ^{0}C	36.85	54.28	0.64	53.64	8.63	83.37

Also it can be remarked that the contribution of the polar component to the surface energy of the analyzed samples is more pronounced in the case of initial dissolution in ILs at 120 ^{0}C, in accordance with the data presented in Tab.1.

Also, it could be noted that minimum surface energy modifications occur in the samples obtained from the cellulose precipitation from its BMIMCl solution obtained at 100 ^{0}C, in accordance with the values presented for the carboxyl group content and equilibrium water sorption values from Tab.1. AMIMCl imparts the highest surface energy among the studied ILs, probably due to the oxidation of cellulose when in solution.

Even if it is reported that AMIMCl and EMIMAc have higher cellulose dissolution capacity than BMIMCl [11, 12], if one's goal is to fractionate biomass and obtain cellulose of high purity, with properties close to that of the original material, than BMIMCl seems a better choice than the other two ILs studied. If highly amorphous and polar cellulose is required (for example in biomedical or in wastewater purification applications), then AMIMCl and/or EMIMAc should be used.

The FTIR spectrum of cellulose (Fig.3) reveals typical representative bands, related to different vibration modes, such as: H-bonded -OH stretching (~3300

cm^{-1}); CH$_2$ and CH stretching at ~2900 cm^{-1}; C–H asymmetric bending and wagging (1470–1455 cm^{-1}); CH bending in cellulose I and cellulose II (1375–1365); CH deformation in cellulose I and cellulose II (1282–1277 cm^{-1}) and C–O–C asymmetric stretching in cellulose I and cellulose II (1162–1125 cm^{-1}). Water weakly associated with cellulose is also present in the 1650–1638 cm^{-1} interval [19, 20].
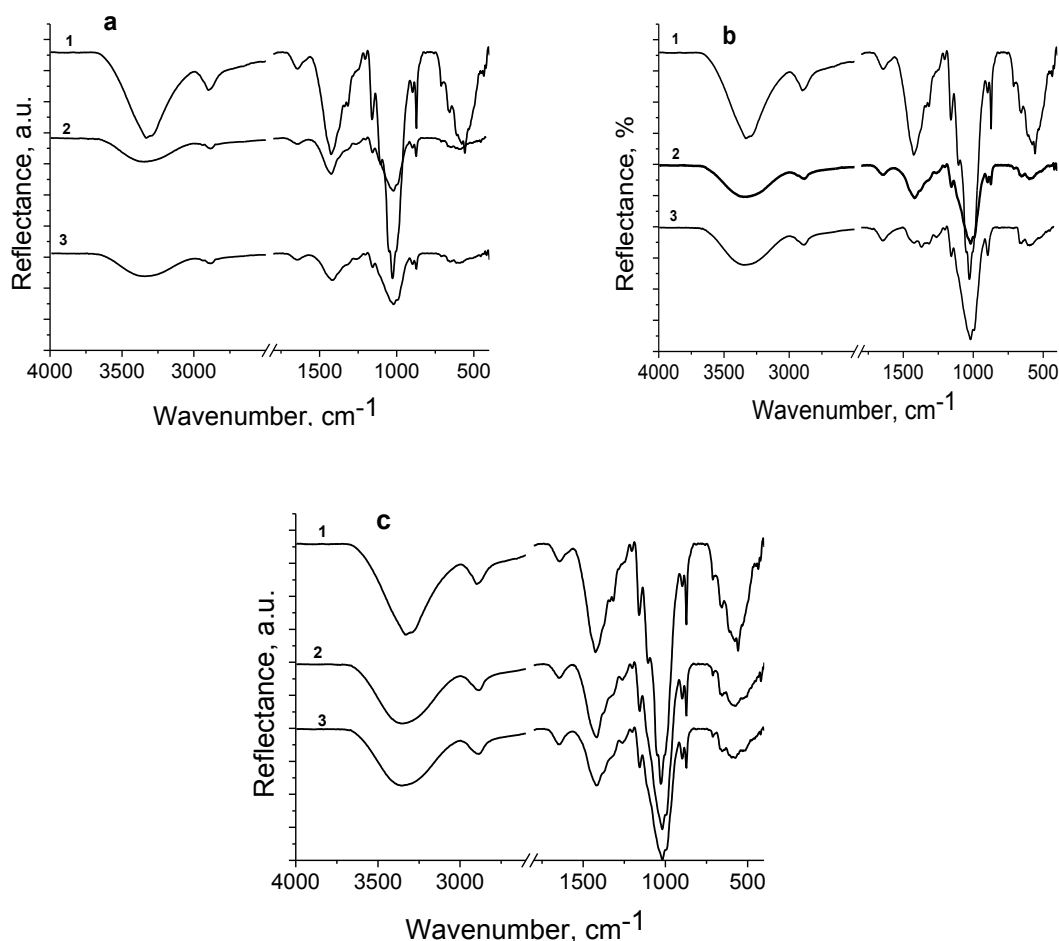
Fig. 3. FT-MIR spectra of cellulose -**1** and regenerated cellulose from its: (**a**) BMIMCl, (**b**) EMIMAc and (**c**) AMIMCl solutions obtained at **2-** 100^{0}C and (**3**)- at 120^{0}C

It has been remarked from Fig. 3 that no supplementary bands appear in the regenerated cellulose in comparison with the spectrum of pure cellulose, which could be due to the fact that the interaction between the studied ionic liquids and cellulose is of physical nature.

The increase in the intensities of the absorption band in the 1650-1700 cm^{-1} region is due to the carboxyl and/or carbonyl groups formation [21, 22] and due to

absorption of atmospheric water, facilitated by the increasing in hydrophilicity. Therefore, it is suggested that oxidation of cellulose end-groups has taken place during cellulose dissolution and processing in the selected ILs (as it can be seen from carboxyl groups determination by methylene blue sorption tests of the precipitated celluloses; Tab.1).

In order to asess the oxidation degree of the cellulose samples, the ratio between the areas of the bands at ~1639 cm^{-1} and at 2900 cm^{-1} has been calculated. This ratio is often recalled to as moisture index (MI) [23].

In order to determine the structural changes that occur in cellulose precipitated from its ILs solutions, the crystallinity index, the lateral order index, the energy of the hydrogen bonds, the ratio of I_β to I_α cellulose anomer and the width of the band associated with –OH stretching at half intensity have been calculated.

The height ratio of the bands at 1371 and 2900 cm^{-1} [21-23] has been used to determine the crystallinity index (CrI) of cellulose and the advantage is that it can be applied to both cellulose I and II [23]. This factor offers a comparative view of the precipitated cellulose structure and properties. A higher CrI owes for better mechanical properties and lower water absorption. Alternatively, a low CrI indicates a dominating amorphous structure of the material, owing for a higher affinity to water and better sound and thermal insulating properties [13].

The lateral order index (LOI) was calculated by using the ratio of the band heights at 1430 and 898 cm^{-1} that is related to the proportion of cellulose I from the sample [23]. Cellulose I generally has good mechanical properties (higher rigidity) owing to its high crystallinity, and it is converted by chemical or thermal treatment into cellulose II, which is dominating amorphous, more thermodynamically stable than cellulose I and more resistant to chemical treatments [13]. Native celluloses usually have high cellulose I content [23, 24].

It has also been found that native cellulose (cellulose I) is actually a mixture of two crystalline modifications (cellulose I_α and I_β) that vary in proportion, depending on the source of the cellulose. In bacterial cellulose the I_α (triclinic) form dominates, while in higher plants I_β (monoclinic) is predominant [24]. During chemical or thermal treatment, cellulose $I\alpha$ converts into the I_β anomer, the latter that is more thermodynamically stable [24, 25].

The ratio of cellulose I_β to I_α (AI) has been calculated as the height of the band at ~ 708 cm^{-1} (ascribed to I_β) divided by the height of the weak band at ~751 cm^{-1} (ascribed to I_α) [25].

It is important to assess whether if the precipitated cellulose is more thermodynamically stable and more resistant to chemical and thermal treatments, in order to define the potential applications of the cellulose material, and the LOI and AI values can semi-quantitatively offer an insight on this matter.

Supplementary, the energy of the hydrogen bonds in the cellulosic material (E_H), and the width of the band associated with –OH stretching at half intensity (w_{-OH})

could offer some additional information about the inter- and intramolecular interactions that occur in/between cellulose macromolecules. These parameters could be thus related also to the stability (physical, chemical) of the cellulosic material, in correlation with CrI and LOI.

The energy of the hydrogen bonds has been calculated by using the following equation (Eq.8):

$$E_H = (1/K)[(\nu - \nu_0)/\nu_0] \tag{8}$$

Where: $\nu_0 = 3650$ cm^{-1} (the standard wavenumber corresponding to the free –OH groups stretching); ν – the standard wavenumber corresponding to the –OH groups stretching observed in the FT-MIR spectra (Fig.3) and K=2.61·10^2 kJ, a spectroscopic constant

The values of the above mentioned parameters are illustrated in Fig.4, for regenerated celluloses and reference.

As it can be seen from Fig. 4, from the AI values of the reference, the I$_\beta$ content is higher than that of the I$_\alpha$, probably due to the thermo-mechanical processing of the original filter paper.

Crystallinity index of cellulose generally decreases in the order Reference > BMIMCl regenerated sample> EMIMAc regenerated sample > AMIMCl regenerated sample for both 100 ^{0}C and 120 ^{0}C, with the mentioning that the crystallinity index of the samples obtained at 120 ^{0}C is lower than in the case of cellulose processing at 100 ^{0}C. This can occur due to the fact that at higher temperatures, the ionic liquids are able to penetrate in a facile manner in the crystalline and semi-crystalline regions of the polymer and break more of the intermolecular hydrogen bonds between the cellulose molecules. The variation in CrI is generally consistent with the ability of the selected ionic liquids to dissolve cellulose. It has been reported that AMIMCl generally has the highest solvation capability for cellulosic biomass, followed by EMIMAc and finally by BMIMCl [4-6], thus AMIMCl having the highest ability to disrupt the hydrogen bonding network resulting in a regenerated material with dominating amorphous character (proved also by MB sorption ability and absorbed water amount, Tab.1).

So, it appears that BMIMCl ionic liquid is the choice of use when desiring a more crystalline cellulosic material.

In correlation with the CrI values it can be seen that the highest crystalline cellulose I content is recorded for the BMIMCl regenerated sample, while the highest cellulose II content is recorded for the AMIMCl regenerated sample. A higher processing temperature generally determines supplementary conversion of cellulose I to cellulose II, more thermodynamically stable.

Higher oxidation degree and thus higher atmospheric water sorption capacity in comparison with the reference sample has been observed from the calculated

values of the MI. Moisture index of cellulose generally increases in the order Reference < BMIMCl regenerated sample < EMIMAc regenerated sample < AMIMCl regenerated sample for both 100 ^{0}C and 120 ^{0}C, with the mentioning that the moisture index of the samples obtained at 120 ^{0}C is lower than in the case of cellulose processing at 100 ^{0}C.

It appears that also, with the higher solvation power and ability to convert cellulose in the thermodynamically stable and amorphous polymorph, the cellulose processing in ionic liquids can also favor degradation, by cellulose oxidation in the presence of atmospheric oxygen, and due to the slightly acidic pH that the molten ILs possess. BMIMCl can act as a cellulose oxidation inhibitor, as demonstrated by our previous results regarding lignocellulosic biomass [26, 27].

Even if the data from Fig. 4 suggests that the ILs are able to convert cellulose I into the amorphous cellulose II; the remaining unconverted cellulose I content is subjected to a second order transition, rearranging itself into the I_α anomer structure, less thermodynamically favored, but with a more compact crystal structure than the I_β anomer [25]. This result is consistent with our previous findings regarding cellulose treated with similar alkylimidazolium ionic liquids [27].

Disrupting of the H bonding in the structure of the biopolymer imparted by the ILs is reflected in the E_H values. For all regenerated samples from their ILs solutions obtained at 100 and 120 ^{0}C, E_H values are lower than in the case of the reference, which owes for quantitatively less hydrogen bonds between the polymer macromolecules. E_H values for the samples from their ILs solutions obtained at 120^{0}C are higher than those of the samples processed at 100^{0}C, probably due to the fact that the treatment at a higher temperature leads to oxidation of the polymer, by forming of carboxylic and carbonylic groups, which supplementary contribute to the formation of hydrogen bonds in the regenerated cellulose. In this case, also, it seems that the BMIMCl ionic liquid is able to preserve upon regeneration a quantitatively similar hydrogen bonding network as the original reference sample.
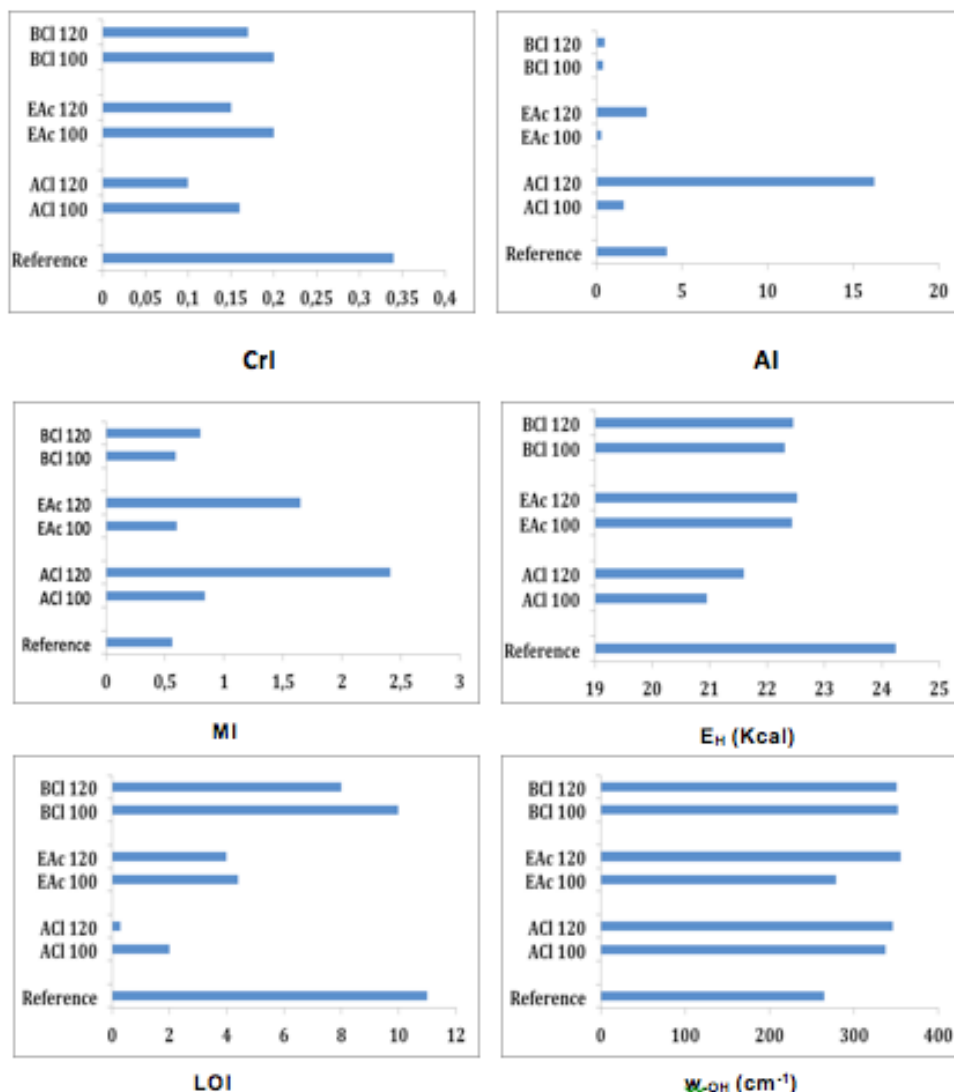
**Fig. 4.** Cellulose samples structural parameters, obtained from interpretation of their FTIR spectra

Similar information is obtained from the width of the –OH stretching band at half intensity (W_{OH}). As all the regenerated samples have a higher value of the W_{OH} comparing with the reference, this may indicate supplementary interactions of the –OH groups from cellulose with polar molecules, such as water. It has been reported in the reference literature, that the –OH groups of regenerated cellulose are generally more reactive than those from the original cellulose samples [13], probably also due to the favorable macromolecular rearrangement of the

macromolecular chains, their –OH groups being faced outwards, thus being more accessible to other reagents.

Similar information could be drawn from the analysis of the FT-NIR spectra of cellulose and regenerated cellulose samples, illustrated in Fig.5. Near infrared spectroscopy has been extensively used as a tool to identify the taxonomic origin of several wood samples, as well as a tool for discriminating between cellulose from bacterial or algal origin and cellulose from superior plants (based on the principal component analysis method), due to some specific overtones belonging to –OH, weakly absorbed water and alkyl groups [28,29].

To our knowledge, this type of spectroscopy has not been used before to characterize cellulose regenerated from their ionic liquid solution.
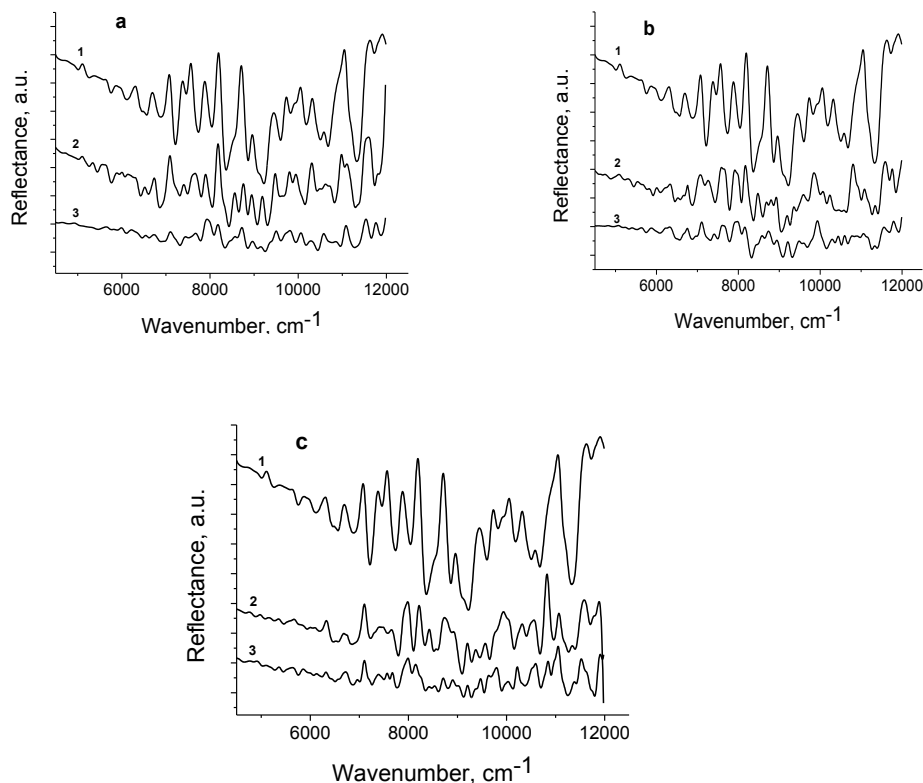
Fig. 5. FT-NIR spectra of cellulose -**1** and regenerated cellulose from its: (**a**) BMIMCl, (**b**) EMIMAc and (**c**) AMIMCl solutions obtained at **2-** 100^0C and (**3**)- at 120^0C

4. Conclusions

The paper aims to complete the existing database comprehending the properties of regenerated cellulose from different alkylimidazolium ionic liquids, under different operational parameters, by studying the properties of regenerated

cellulose from its solutions in 1-ethyl-3-methylimidazolium acetate, 1-allyl-3-methylimidazolium chloride and 1-buthyl-3-methylimidazolium chloride ionic liquids, obtained at 100 ^{0}C and 120 ^{0}C.

Structural modification in crystallinity, crystal axis orientation, structural transitions and potential degradation has been assessed by FTIR spectroscopy (middle infrared and near-infrared) and correlated with water sorption experiments. Oxidation has been correlated with methylene blue sorption capacity of the cellulosic material, and the surface properties (polarity; surface formal charge) of the regenerated cellulose have been assessed by surface energy measurements. It has been observed that crystallinity index of cellulose generally decreases in the order reference > BMIMCl regenerated sample> EMIMAc regenerated sample > AMIMCl regenerated sample for both 100 ^{0}C and 120 ^{0}C, with the mentioning that the crystallinity index of the samples obtained at 120 ^{0}C is lower than in the case of cellulose processing at 100 ^{0}C. In correlation with the CrI values it can be seen that the highest crystalline cellulose I content is recorded for the BMIMCl regenerated sample, while the highest cellulose II content is recorded for the AMIMCl regenerated sample. A higher processing temperature generally determines supplementary conversion of cellulose I to cellulose II, more thermodynamically stable. Also, the regenerated material obtained by precipitation of the solutions obtained at 120 ^{0}C are more polar (hydrophilic) and tend to have a darker color, due to the formation of chromophoric carbonyl groups.

REFERENCES

[1] Zhao, D., Li, H., Zhang J., Fu, L, Liu, M., Fu, J., Ren P. Dissolution of cellulose in phosphate-based ionic liquids. *Carbohydrate Polymers*, 87, (2012), 1490–1494.

[2] Dogan, H. & Hilmioglu, N. D. Dissolution of cellulose with NMMO by microwave heating. *Carbohydrate Polymers*, 75, (2009), 90–94.

[3] Fukaya, Y., Hayashi, K., Wada, M. & Ohno, H. Cellulose dissolution with polar ionic liquids under mild conditions: Required factors for anions. *Green Chemistry,* 10, (2008), 44–46.

[4] Chang, C., Zhang, L. Cellulose-based hydrogels: Present status and application prospects. *Carbohydrate Polymers,* 84, (2010), 40–53.

[5] Duchemin, B., Aji, M., Oksman, K. All-cellulose composites by partial dissolution in the ionic liquid 1-butyl-3-methylimidazolium chloride. *Composites: Part A*, 40, (2009), 2031–2037.

[6] Simkovic I. What could be greener than composites made from polysaccharides? *Carbohydrate Polymers*, 4, (2008), 759–762.

[7] Schurz J. Trends in polymer science – a bright future for cellulose. *Prog Polym Sci*, 24, (1999), 481–483.

[8] O'Sullivan AC. Cellulose: the structure slowly unravels. *Cellulose*, 4, (1997), 173–208.

[9] Potthast, A., Rosenau, T., Buchner, R., Ebner, G., Bruglachner, H., Sixta, H. & Kosma, P. The cellulose solvent system N,N-dimethylacetamide/lithium chlo- ride revisited: The effect of water on physicochemical properties and chemical stability. *Cellulose*, 9, (2002), 41–53.

[10] Croitoru, C., Patachia, S., Cretu, N., Boer, A., Friedrich, C. Influence of ionic liquids on the surface properties of poplar veneers. *Appl. Surf. Sci.*, 257, (2011), 6220–6225.

[11] Garcia, H., Ferreira, R., Petkovic, M., Ferguson, J.L., Leitao, M.C., Gunaratne, H.Q.N. Dissolution of cork biopolymers in biocompatible ionic liquids. *Green Chem.*, 9, (2010), 12367–12369.

[12] Soykeabkaew N, Nishino T, Peijs T. All-cellulose composites of regenerated cellulose fibres by surface selective dissolution. *Compos Part A: Appl Sci Manuf 2,* 40 Issue 4, (2009), 321-328.

[13] Klemm D, Philipp B, Heinze T, Heinze U, Wagenknecht W. Comprehensive Cellulose Chemistry Volume I, Fundamentals and Analytical Methods. Wiley-VCH, Weinheim,1998, p. 105-170.

[14] Schnabelrauch M, Heinze T, Klemm D, Nehls I, Kotz J. Investigations on Synthesis and Characterization of Carboxy-Groups Containing Cellulose Sulfates. *Polym Bull,* 27, (1991), 147-153.

[15] Rudawska, A., Zajchowski, S., Surface free energy of polymer/wood composites. *Polimery*, 52, (2007), 453-455.

[16] Mohammed-Ziegler, I., Oszlanczi, A., Somfai, B., Horvolgyi, Z., Paszli, I., Holmgren, A.Surface free energy of natural and surface-modified tropical and European wood species. *J Adhes Sci Technol.*, 18, (2004), 687-713.

[17] Oltean L, Teischinger A, Hansmann C. Visual Classification of the Wood Surface Discolouration Due to Artificial Exposure to UV Light Irradiation of Several European Wood Species - a Pilot Study. *Wood Res-Slovakia*, 55, (2010), 37-48.

[18] Temiz A, Yildiz UC, Aydin I, Eikenes M, Alfredsen G, Colakoglu G. Surface roughness and color characteristics of wood treated with preservatives after accelerated weathering test. *Appl Surf Sci.*, 250, (2005), 35-42.

[19] Horikawa Y, Clair B, Sugiyama J. Varietal difference in cellulose microfibril dimensions observed by infrared spectroscopy. *Cellulose* 16, (2009), 1170-1178.

[20] Ibrahim M, Osman O. Spectroscopic Analyses of Cellulose: Fourier Transform Infrared and Molecular Modelling Study. *J Comput Theor Nanos.*, 6, (2009), 1054-1058.

[21] Yang CQ, Freeman JM. Photooxidation of Cotton Cellulose Studied by FT-IR Photoacoustic-Spectroscopy. *Appl Spectrosc*, 45, (1991), 1695-1698.

[22] Popescu CM, Popescu MC, Singurel G, Vasile C, Argyropoulos DS, Willfor S. Spectral characterization of eucalyptus wood. *Appl Spectrosc*, 61, (2007), 1168-1177.

[23] He JX, Tang YY, Wang SY. Differences in morphological characteristics of bamboo fibres and other natural cellulose fibres: Studies on X-ray diffraction, solid state C-13-CP/MAS NMR, and second derivative FTIR spectroscopy data. *Iran Polym J.*,16, (2007), 807-818.

[24] Marechal Y, Chanzy H. The hydrogen bond network in I-beta cellulose as observed by infrared spectrometry. *J Mol Struct Volume,* 52, (2000), 183-196.

[25] Sturcova A, His I, Apperley DC, Sugiyama J, Jarvis MC. Structural details of crystalline cellulose from higher plants. *Biomacromolecules*, 5, (2004), 1333-1339.

[26] Patachia, S., Croitoru, C., Friedrich, C. Effect of UV exposure on the surface chemistry of wood veneers treated with ionic liquids. *Applied Surface Science*, 258, (2011), 135-140.

[27] Croitoru, C., Patachia, S., Porzsolt, A., Friedrich, C. Effect of alkylimidazolium based ionic liquids on the structure of UV-irradiated cellulose. *Cellulose*, 18, (2011), 1469-1479.

[28] Krämer, K., Ebel, S. Application of NIR reflectance spectroscopy for the identification of pharmaceutical excipients. *Analytica Chimica Acta* 420, (2000), 155-161.

[29] Poke, F.S., Raymond, C.A. Predicting Extractives, Lignin, and Cellulose Contents Using Near Infrared Spectroscopy on Solid Wood in Eucalyptus globulus. *Journal of Wood Chemistry and Technology*, 26, (2002), 187-199.

PHASE EQUILIBRIUMEXPERIMENTS AND MODELING FOR THE CARBON DIOXIDE + ETHANOL SYSTEM AT HIGH PRESSURES

Sergiu SIMA[1], Catinca SECUIANU[1,2*], Viorel FEROIU[1*], Dan GEANĂ[1]

[1]Depart. Inorganic Chemistry, Physical Chemistry & Electrochemistry, Politehnica University of Bucharest, 1-7 Gh. Polizu Street, S1, 011061 Bucharest, Romania
[2]Honorary Research Fellow, Depart. Chemical Engineering, Imperial College London, South Kensington Campus, SWR7 2AZ London, United Kingdom

Abstract

Isothermal (P, T, x, y) data have been measured for the binary system carbon dioxide + ethanol at 333.15 K. The pressure range under investigation was between 6.8 and 105.5 bar. The phase equilibrium apparatus used in this work was a variable-volume visual cell coupled with ROLSI^{TM} (Rapid Online Sample Injector) valves and a GC (gas chromatograph). The new experimental data are modeled with the Soave-Redlich-Kwong (SRK) equation of state coupled with G^E-EOS (excess Gibbs free energy) mixing rules.

Keywords: VLE, CO_2, ethanol, SRK, high-pressures

1. Introduction

Nowadays supercritical fluid processes are important alternative to conventional methods in many fields, such as extractions, particle micronization, material processing, chromatography or crystallization/purification [1-3]. A fundamental role in the success of these applications is played by the equilibrium and volumetric properties of binary mixtures containing organic solvent and supercritical fluids, especially carbon dioxide.

High-pressure vapor-liquid equilibrium data of carbon dioxide + alcohol systems are of interest due to their importance in the supercritical extraction of thermal labile compounds, extraction of natural products using near critical solvents, and dehydration of alcohols using supercritical carbon dioxide [1-3].Among the most important compounds in separation processes are the low molecular weight alcohols. They are often used as entrainers to control the polarity of a supercritical fluid (SFC) solvent in extraction applications and are also used as modifiers in

---

[*]Corresponding authors: E-mail address:c_secuianu@chim.upb.ro (C. Secuianu),
v_feroiu@chim.upb.ro (V. Feroiu)

SFC chromatography. The most important supercritical fluid for these processes has shown to be carbon dioxide, because it is cheap, nontoxic, nonflammable, and has a low critical temperatures of 304.25 K.

The carbon dioxide + ethanol mixture is very important industrially and the system has received much attention. However, numerous articles present only solubility of carbon dioxide in ethanol or VLE data at low pressures. A number of papers have reported experimental vapor-liquid equilibria data around the critical temperature of carbon dioxide (298-333 K). Although we found many papers investigating the carbon dioxide + ethanol binary system [4], only few report VLE data measured from low pressures (5 bar) to the critical point of mixture. In addition, there are significant deviations among the data from different sources [5].

The purpose of this paper is to present new high-pressure vapor-liquid equilibrium data for the carbon dioxide + ethanol system at 333.15 K. In this work we made new measurements using ROLSI^{TM} valves and a GC, in a high-pressure visual cell, for carbon dioxide + ethanol system up to 105.5bar.

The phase equilibria data for the studied system were modeled with the Soave-Redlich-Kwong [6] (SRK) equation of state coupled with a G^E-EOS mixing rule.The Huron–Vidal (HV) mixing rules [7] coupled with the reduced UNIQUAC excess Gibbs energy model [8,9] was chosen.

2. Experimental

Materials

Carbon dioxide (mass fraction purity > 0.997) was provided by LindeGaz Romania, Bucharest, Romania and ethanol (mass fraction purity 0.998) was a SIGMA product. Chemicals were used without further purification, except for the careful degassing of ethanol. The mole fraction purity of ethanol was checked by gas chromatographic analysis and it is > 0.999.

Apparatus and procedure

A detailed description of the experimental installation was presented in earlier papers [10-12]. The main component of the installation is a high pressure visual cell with variable volume connected with a modern sampling and analysis equipment. Samples from liquid and vapor phases are collected via ROLSI^{TM} valves and sent to the gas chromatograph (GC) equipped with a TCD (thermal conductivity detector). The apparatus is completed with a Teledyne ISCO model 500D syringe pump.

The procedure is similarly as described previously [10-12]. The entire internal loop of the apparatus including the equilibrium visual cell is rinsed several times with carbon dioxide. Then, the visual cell is evacuated with a vacuum pump. The alcohol is degassed with a vacuum pump and vigorously stirring, and it is charged into the cell. The lighter component (in this case CO_2) is introduced with the Teledyne syringe pump into the cell and the pressure is set to the desired value. Then the cell is heated to the experimental temperature. To facilitate the approach to an equilibrium state, the mixture in the cell is stirred for a few hours. Next the stirrer is switched off, and about one hour was allowed to pass until the coexisting phases are completely separated. Samples of liquid and vapor phases are withdrawn with the ROLSI valves and analyzed with the GC. At the equilibrium temperature and pressure, at least six samples of the liquid phase are analyzed to check the repeatability. As the sample sizes are very small, the equilibrium pressure in the cell remains constant.

The calibration of the TCD for CO_2 and ethanol is done using gas chromatographic syringes by injecting known amounts of each component. Calibration data are fitted to quadratic polynomials to obtain the mole number of the component versus chromatographic area. The correlation coefficients of the GC calibration curves were 0.999 for carbon dioxide and 0.997 for ethanol.

The uncertainties of the measurements are estimated to be within ± 0.1 K for temperature and to be better than ± 0.01 MPa for pressure from calibration with a precision hydraulic deadweight tester (model 580C, DH-Budenberg SA, Aubervilliers, France).

3. Modeling

The phase of the carbon dioxide + ethanol binary system was modeled using the Soave-Redlich-Kwong (SRK) equation of state (EOS) [6] coupled with Huron-Vidal (HV)-residual UNIQUAC [7-9] mixing rules. This model was chosen based on previous results with mixtures containing hydrogen bonding compounds.The Soave-Redlich-Kwong equation of state is [6]:

$$P = \frac{RT}{V-b} - \frac{a(T)}{V \cdot (V+b)} \tag{1}$$

The Huron and Vidal mixing rules [7] for the SRK EOS are given by:

$$b = \sum_i x_i b_i \tag{2}$$

$$\frac{a}{bRT} = \sum_i x_i \left(\frac{a_i}{b_i RT} - \frac{\ln \gamma_i (P \to \infty)}{\ln 2} \right) \tag{3}$$

where $\gamma_i (P \to \infty)$ is the activity coefficient of the component in the mixture at infinite pressure.

The HV mixing rule is based on a reduced UNIQUAC model suitable for infinite pressure conditions [8,9]. The model is reduced to its residual part only:

$$\ln \gamma_i (P \to \infty) = q_i \left[1 - \ln \left(\sum_j \theta_j \tau_{ji} \right) - \sum_j \frac{\theta_j \tau_{ij}}{\sum_k \theta_k \tau_{kj}} \right] \tag{4}$$

$$\theta_i = \frac{q_i x_i}{\sum_j q_j x_j} \tag{5}$$

$$\tau_{ij} = \exp \left(-\frac{u_{ij}}{T} \right) \tag{6}$$

The interaction parameters are considered temperature dependent [8,9]:

$$u_{ij} = u_{ij}^0 + u_{ij}^1 \frac{1}{T} \tag{7}$$

4. Results and discussions

The equilibrium compositions for the carbon dioxide + ethanol binary system were measured at 333.15 K and the results are plotted in Figure 1. The values are typically averages offive or six sample measurements. For the VLE measurements, theuncertainty of the mole fraction in the liquid phase is typically0.0005.

Figure 2 shows a comparison of the new measurements with existing data [4,12] for the same temperature. A good agreement can be observed, nearly within the experimental uncertainty.It should be remarked that the data reported by ref. [4] are measured using a static-analytical method with manual phases sampling, while ref. [12] presents only the liquid phase. A more detailed comparison of our data with existing literature data at nearest temperatures is made in Figure 3. It can be noticed that there are significant deviations among the data from different sources, as Polishuk et al. [5] also remarked. Therefore new experiments are required. Although it is difficult to appreciate the quality of data, our new measurements are

in good agreement with those previously measured in our group [4,12] as well as with those of Cruz et al. [20] and Galicia-Luna et al. [21], which are more recent and measured with high quality equipments.
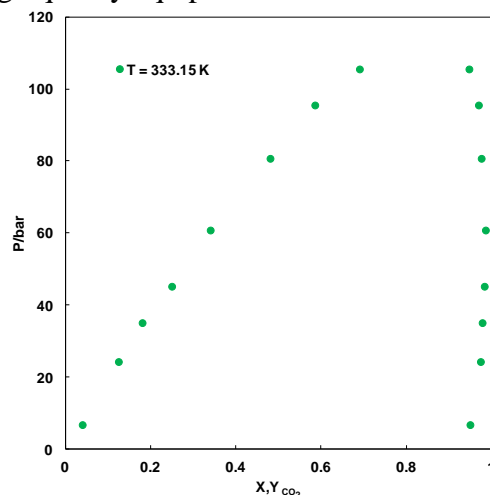
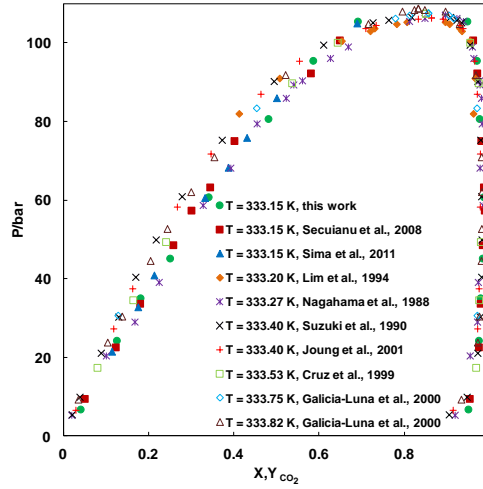**Fig. 1.** Pressure composition data for the carbon dioxide + ethanol binary system at 333.15 K.
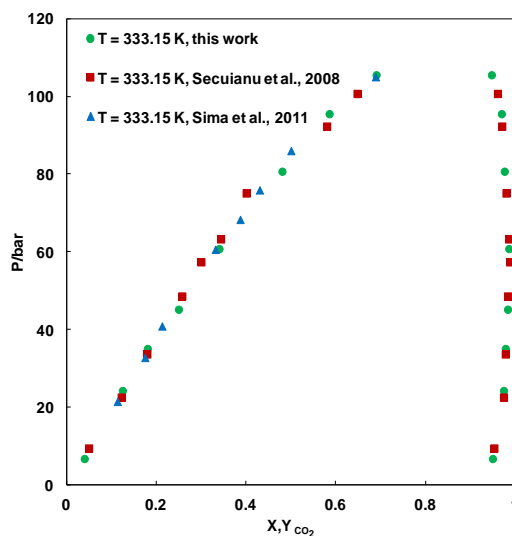
Fig. 2. Comparison of measured and literature data for the carbon dioxide + ethanol system at 333.15 K.

The new data measured in this work and literature data were modeled with the SRK/HV mixing rules and the reduced UNIQUAC model using a semi-predictive approach [13,14].

The calculations were made using the software package PHEQ (Phase Equilibria Database and Applications), developed in our laboratory [15].

The modeling procedure is explained in detail in our previous works [13,14]. VLE data at three temperatures near the critical point of the carbon dioxide (i.e., 293.15, 303.15, and 313.15 K) for the carbon dioxide + ethanol system were firstly correlated with the SRK equation of state [6] coupled with the HV mixing rules and the reduced UNIQUAC model (Eqs.(4)–(6)).

Fig. 3. Comparison of measured and literature data for the carbon dioxide + ethanol system at 333 K.

These values of the HV-residual UNIQUAC parameters (u_{12} and u_{21}) were used to obtain a linear dependence with the inverse of the temperature (Eq. (7)).Thus, the linear equations [13] for the temperature dependence of the reduced UNIQUAC parameters (u_{12} and u_{21}) are:

$$u_{12} = 196826.3 \cdot T^{-1} - 425.5 \tag{8}$$

$$u_{21} = -165316.9 \cdot T^{-1} + 598.9 \tag{9}$$

with u_{ij} and T in K. The values of SRK/HV parameters from the linear correlations were used to predict VLE at higher or lower temperatures.

The results of the calculations by the above procedure are compared with our experimental data in Figure 4. As can be seen, the agreement between the experimental data and the calculations results is very good.

Several isotherms comparing the prediction results with experimental data are also illustrated in Figure 5 (selected literature data). Taking into account the semi predictive approach used in this work, the VLE prediction for the carbon dioxide + ethanol system is reasonable.
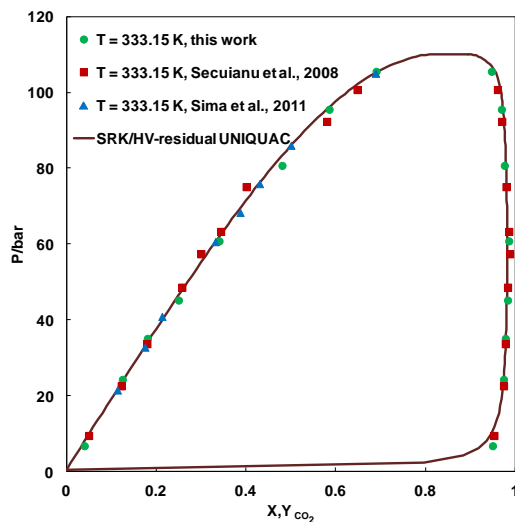
Fig. 4. Comparison of experimental phase equilibrium data with calculated resultsby the SRK/HV-residual UNIQUAC model for the carbon dioxide + ethanol system.
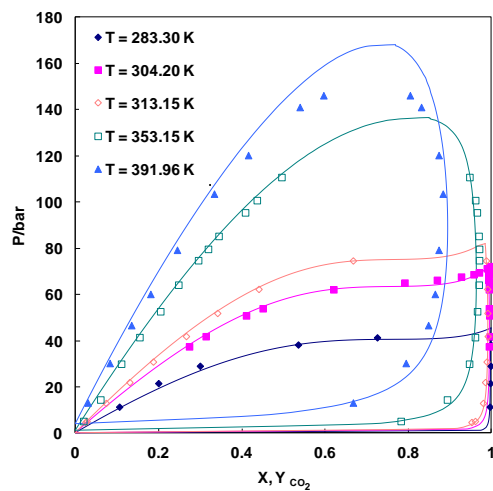
Fig. 5. Comparison of selective literature data for the carbon dioxide + ethanol system and predictions with SRK/HV-residual UNIQUAC: ♦, Hirohama et al., 1993 [22]; ■, Takishima et al., 1986 [23]; ◊, Galicia-Luna et al., 2000 [21]; □, Secuianu et al., 2008 [4]; ▲, Mendoza de la Cruz &Galicia-Luna, 1999 [20].

6. Conclusions

A visual high-pressure variable volume static-analytic apparatus coupled with ROLSI^{TM} valves and a GC was used to obtain VLE data for the carbon dioxide + ethanol system. New experimental data were measured 333.15 K and pressures up to 105.5 bar. The SRK/HV model with the reduced UNIQUAC model is applied in modeling the phase behavior of the mixture under study in a semi-predictive approach. The VLE data of three isotherms measured near room temperature (i.e., 293.15, 303.15, and 313.15 K) were used to obtain a linear correlation of the HV-reduced UNIQUAC parameters with the temperature. The values of the parameters from the linear correlation were used to predict VLE curves. The VLE data is well predicted taking into account the relative simple model and the semi-predictive approach used.

REFERENCES

[1] Fonseca J.M.S., Dohrn R., Peper S., Review. High-pressure fluid-phase equilibria: Experimental methods and systems investigated (2005−2008). *Fluid Phase Equilibria*, 300 (1–2), (2011), 1–69.

[2] Dohrn R., Peper S., Fonseca J.M.S., High-pressure fluid-phase equilibria: Experimental methods and systems investigated (2000–2004). *Fluid Phase Equilibria*, 288 (1–2), (2010), 1–54.

[3] Christov M., Dohrn R., Review Article. High-pressure fluid phase equilibria: Experimental methods and systems investigated (1994–1999). *Fluid Phase Equilibria*, 202 (1), (2002), 153–218.

[4] Secuianu C., Feroiu V., Geană D., Phase behavior for carbon dioxide + ethanol system: Experimental measurements and modeling with a cubic equation of state. *Journal of Supercritical Fluids*, 47 (2), (2008), 109–116.

[5] Polishuk I., Wisniak J., Segura H., Simultaneous prediction of the critical and sub-critical phase behavior in mixtures using equation of state I. Carbon dioxide-alkanols. *Chemical Engineering Science*, 56 (23), (2001), 6485–6510.

[6] Soave G., Equilibrium constants from a modified Redlich-Kwong equation of state. *Chemical Engineering Science*, 27 (6), (1972), 1197–1203.

[7] Huron M.-J., Vidal J., New mixing rules in simple equations of state for representing vapour-liquid equilibria of strongly non-ideal mixtures. *Fluid Phase Equilibria*, 3 (4), (1979), 255–271.

[8] Feroiu V., Geană D., Prediction of vapor-liquid equilibria at high pressures using activity coefficients at infinite dilution. *Fluid Phase Equilibria*, 120 (1–2), (1996), 1–10.

[9] Geană D., Feroiu V., Prediction of Vapor−Liquid Equilibria at Low and High Pressures from UNIFAC Activity Coefficients at Infinite Dilution. *Industrial & Engineering Chemical Research*, 37 (3), (1998), 1173–1180.

[10] Secuianu C., Feroiu V., Geană D., High-pressure phase equilibria for the carbon dioxide plus methanol and carbon dioxide plus isopropanol systems. *Revista de Chimie*, 54 (11), (2003), 874–879.

[11] Secuianu C., Feroiu V., Geană D., High-pressure vapor-liquid equilibria in the system carbon dioxide and 2-propanol at temperatures from 293.25 K to 323.15 K. *Journal of Chemical and Engineering Data*, 48 (6), (2003), 1384–1386.

[12] Sima S., Feroiu V., Geană D., New High Pressure Vapor–Liquid Equilibrium and Density Predictions for the Carbon Dioxide + Ethanol System. *Journal of Chemical and Engineering Data*, 56 (12), (2011), 5052–5059.

[13] Secuianu C., PhD Thesis, (2004), University "Politehnica" of Bucharest.

[14] Secuianu C., Feroiu V., Geană D., High-pressure vapor–liquid and vapor–liquid–liquid equilibria in the carbon dioxide + 1-heptanol system. *Fluid Phase Equilibria*, 270 (1-2), (2008), 109–115.

[15] Geană D., Rus L., Proceedings of the Romanian International Conference on Chemistry and Chemical Engineering (RICCCE XIV), Vol. 2, (2005), Bucharest, Romania, Pages 170–178.

[16] Lim J.S., Lee Y.Y., Chun H.S., Phase equilibria for carbon dioxide-ethanol-water system at elevated pressures. *The Journal of Supercritical Fluids*, 7 (4), (1994), 219–230.

[17] Nagahama K., Suzuki J., Suzuki T., High pressure vapor-liquid equilibria for the supercritical CO2 + ethanol + water system, in: Perrut, M. (Ed.), (1998), Proc. Int. Symp.Sup. Fluids, Nice, France, Vol.1, 143–150.

[18] Suzuki K., Sue H., Itou M., Smith R.L., Inomata H., Arai K., Saito S., Isothermal vapor-liquid equilibrium data for binary systems at high pressures: carbon dioxide-methanol, carbon dioxide-ethanol, carbon dioxide-1-propanol, methane-ethanol, methane-1-propanol, ethane-ethanol, and ethane-1-propanol systems. *Journal of Chemical and Engineering Data*, 35 (1), (1990), 63–66.

[19] Joung S.N., Yoo C.W., Shin H.Y., Kim S.Y., Yoo K-P., Lee C.S., Huh W.S., Measurements and correlation of high-pressure VLE of binary CO2-alcohol systems (methanol, ethanol, 2-methoxyethanol and 2-ethoxyethanol). *Fluid Phase Equilibria*, 185 (1-2), (2001), 219–230.

[20] Mendoza de la Cruz J.L., Galicia-Luna L.A., High-pressure vapor-liquid equilibria for the carbon dioxide + ethanol and carbon dioxide + propan-1-ol systems at temperatures from 322.36 K to 391.96 K. *ELDATA: The International Electronic Journal of Physico-Chemical Data*, 5, (1999), 157–164.

[21] Galicia-Luna L.A., Rodríguez A.O., Richon D., New apparatus for the fast determination of high-pressure vapor-liquid equilibria of mixtures and of accurate critical pressures. *Journal of Chemical and Engineering Data*, 45 (2), (2000), 265–271.

[22] Hirohama S., Takatsuka T., Miyamoto S., Muto T., Measurement and correlation of phase equilibria for the carbon dioxide-ethanol-water system. *Journal of Chemical Engineering of Japan*, 26, (1993), 408–415.

[23] Takishima S., Saiki K., Arai K., Saito S., Phase equilibria for CO_2-C_2H_5OH-H_2O system. *Journal of Chemical Engineering of Japan*, 19 (1), (1986), 48–56.

LONG RANGE TRANSPORT OF HAZARDOUS AEROSOL PARTICLES. CASE STUDY: INTRUSIONS OVER ROMANIA

Horaţiu ŞTEFĂNIE*, Nicolae AJTAI, Alexandru OZUNU

Babes Bolyai University, Faculty of Environmental Science, Department of Environmental Science, 30 Fântânele Street, 400294, Cluj-Napoca, Romania

Abstract

The main objective of this study is to assess the hazards associated with the presence of hazardous aerosol particles in Romania using remote sensing techniques. The hazardous aerosols particles present in the atmosphere have various origins and are represented by mineral dust, biomass burning soot particles and volcanic ash. Every type of aerosol has different optical and microphysical properties. Considering this properties, one can identify the type of particle and its origins.

Keywords: aerosol, remote sensing, optical properties, hazardous particles.

1. Introduction

This study presents evidences of long range transport of hazardous particles from different types of sources. Monitoring of such atmospheric particles remainsa difficult task since aerosol particles are highly inhomogeneousand variable in time and space. Consequently,aerosol observations have to be global and continuous. The ground-based aerosol remote sensing contributes significantly to the understandingof aerosols properties and potential impacts associated.

In Romania the hazardous particles intrusions are monitored at 4 stations belonging to the Romanian Atmospheric 3D Research Observatory (RADO): *Bucharest_Inoe*station (Lat: 44.34806° N, Long: 26.02972° E; elevation: 93 m),*CLUJ_UBB* station (Lat: 46.76833° N, Long: 23.55139° E, elevation: 405m),*Eforie* station (Lat: 44.07500° N, Long: 28.63222° E, elevation: 40 m) and *Timisoara* station (Lat: 45.7462° N, Long: 21.22736° E, elevation: 122 m).

The most common intrusions of hazardous particles are represented by mineral dust, volcanic ash and soot particles from biomass burning [1-3].

The saharan mineral dust intrusions that may reach over Europe are a good example. Even though they occur relatively often, there is a low associated risk to

---

*Corresponding author - E-mail: horatiu.stefanie@ubb.cluj.ro (Horatiu Stefanie)

human health and the environment due to the fact that dust particles are transported in the upper layers of the atmosphere most of the time.

The volcanic ash proved its hazardous properties in recent history. Although it is composed of small particles compared to other materials usually ejected during an eruption, damages and hazards associated can be significant because once in the atmosphere, is subject to long-range transport processes and spread over large surfaces [4].

Another example of long range transport of aerosol is the soot particles from biomass burning. The wildfires may occur in the Balkan Peninsula or in Eastern Europe, huge amounts of soot being injected into the atmosphere [5].

2. Material and method

Data analyzed in this study were provided by the Romanian Atmospheric 3D Research Observatory, NASA – AERONET stations in Romania equipped with Cimel CE 318 sun-photometers [6] (Fig. 1). The AERONET network aim is to provide two types of data: direct Sun spectral data and inversion data derived from the angular distribution of the sky radiance.

The basic direct sun algorithm parameters used for this study are AOT (Aerosol Optical Thickness) and Angstrom parameter.

The **Aerosol Optical Thickness (AOT)** is the degree to which aerosols prevent the transmission of light through absorption and scattering processes. The aerosol optical thickness (τ) is defined as the integrated extinction coefficient over a vertical column of unit cross section [7] (GESDISC, 2014).

The **Angstrom parameter (α)** describes the dependency of the aerosol optical thickness, or aerosol extinction coefficient on wavelength [8]. The first derivative of AOT with wavelength in a logarithmic scale is known as the Angstrom parameter (α) [9]. The Angstrom parameter is a good indicator of the aerosol particle size. Large values of the Angstrom exponent indicate the predominance of small particle scattering, whereas lower values are associated with coarse particles.

The inversion data used in this study are the fine and coarse volume concentrations - C_{vf} and C_{vc} ($\mu m^3/\mu m^2$) and the single scattering albedo - $\omega_0(\lambda)$.

The **fine and coarse volume concentrations** (C_{vf} and C_{vc} ($\mu m^3/\mu m^2$)) retrieved within the size range $0.05\mu m \leq r \leq 15 \ \mu m$. The fine and coarse volume concentrations are calculated using sky radiance almucantar measurements at 440, 675, 870 and 1020 nm and the direct sun measurements (AOT) at the same wavelengths [10].

The **single scattering albedo** is represented by the ratio of scattering efficiency to total extinction efficiency at wavelengths corresponding to the sky radiance measurements.

HYSPLIT back-trajectories were used to identify different patterns of long range transport phenomena [11]. Results show intrusion events which can be validated also by modeling software such as Barcelona Supercomputer's BSC-DREAM8b v2.0 Atmospheric Dust Forecast System [12].
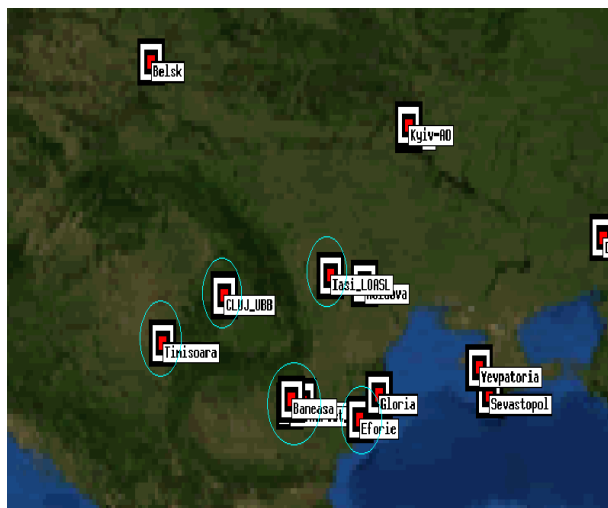

Fig. 1. NASA – AERONET - Aerosol Robotic Network stations in Romania
Source: http://aeronet.gsfc.nasa.gov/cgi-bin/type_piece_of_map_opera_v2_new

3. Results and discussions

3.1. Mineral dust

A good example of Saharan dust intrusion over Romania occurred in 16st August 2010. Representative for the mineral dust aerosol is a clear bimodal representation and the predominance of the coarse mode in the size distribution (for AERONET data, r > 0.6 μm, Fig. 2). The Angstrom parameter also has lower values (values< 1.2, Fig.3). Given the fact that mineral dust particles are larger and significantly less absorbing, the single scattering albedo $\omega_0(\lambda)$ increases or remains neutral with the increase of λ. This are a major characteristic employed in the characterization of a dust intrusion [13].
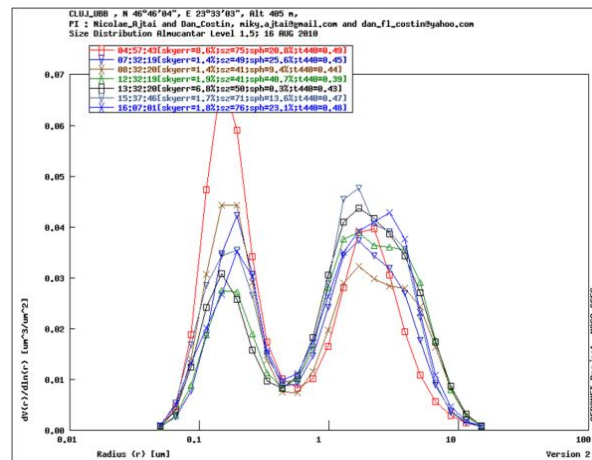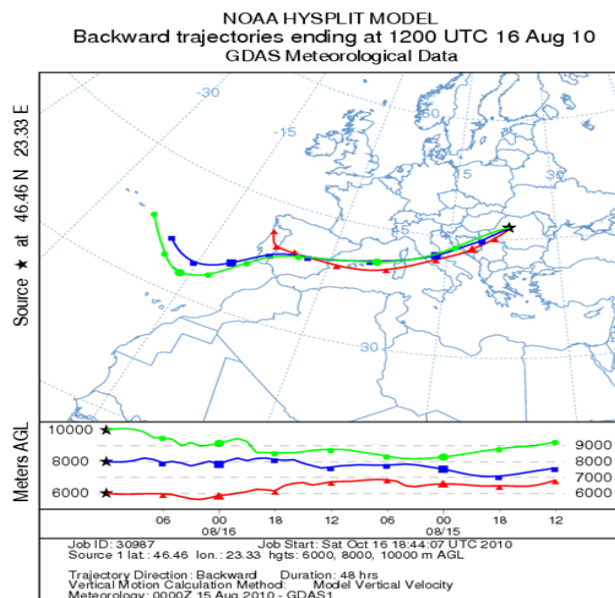
Fig. 2. Size distribution for August 16st 2010at *CLUJ_UBB*AERONET station
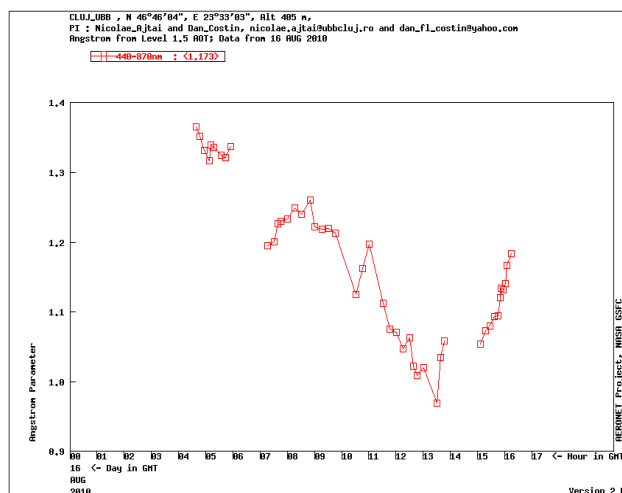
**Fig. 3.** Angstrom parameterforAugust16st 2010at *CLUJ_UBB*AERONET station

We also compute a HYSPLIT model backward trajectory for the air mass over Cluj-Napoca for 16st August 2010, (Fig. 4), were we can see that the air mass was near de Saharan desert a few days before arriving over Cluj-Napoca.

Fig. 4. NOAA HYSPLIT Backward TrajectoryforAugust16st 2010

Also, using the Barcelona Super Computer BSC DREAM model, we obtained a dust load simulation for the same day, simulation which confirm thesaharan dust intrusion over Romania
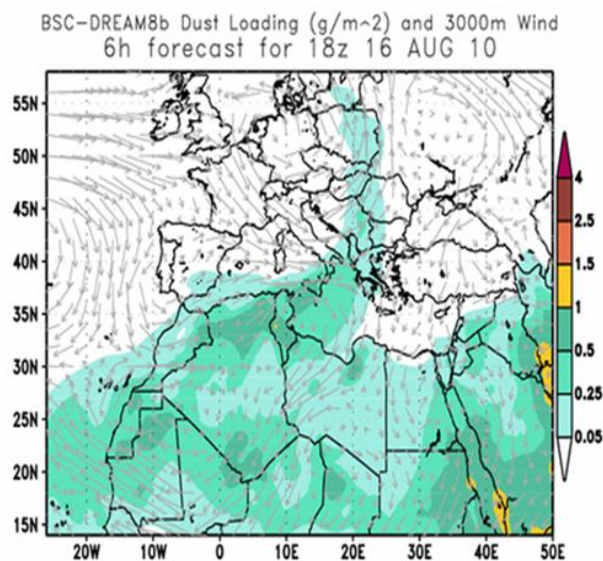
**Fig. 5.** BSC-DREAM dust loading simulation for August 16st 2010

3.2. *Volcanic ash*

An eruption at Grímsvötn volcano in Iceland occurred in May 21st 2011. According to simulations regarding the volcanic ash dispersion made by the Rheinisches Institut für Umweltforschung [14] (Fig. 6), the ash plume reached over Northern and North-Eastern parts of Romania in small quantities during 26th of May.
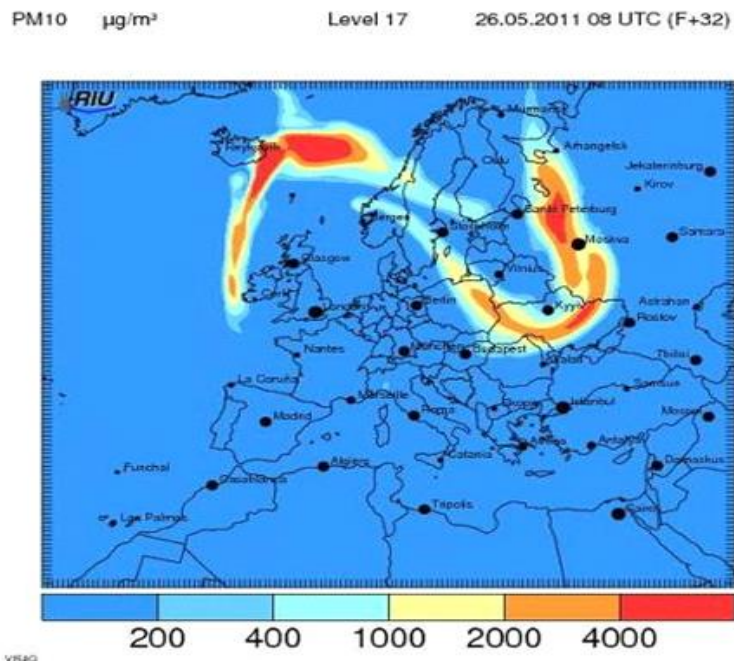
Fig. 6. Rheinisches Institut für Umweltforschung – RIU simulation of Volcanic Ash dispersion

Measurements made with the CIMEL sun photometer at the Cluj_UBB AERONET station determined the presence of volcanic ash particles over Cluj-Napoca city on May 26st 2014. We can observe an increased AOT (Fig. 7)and the low values of the Angstrom parameter (Fig. 8) which indicates the predominance of the coarse particles in the atmosphere associated with the volcanic ash.
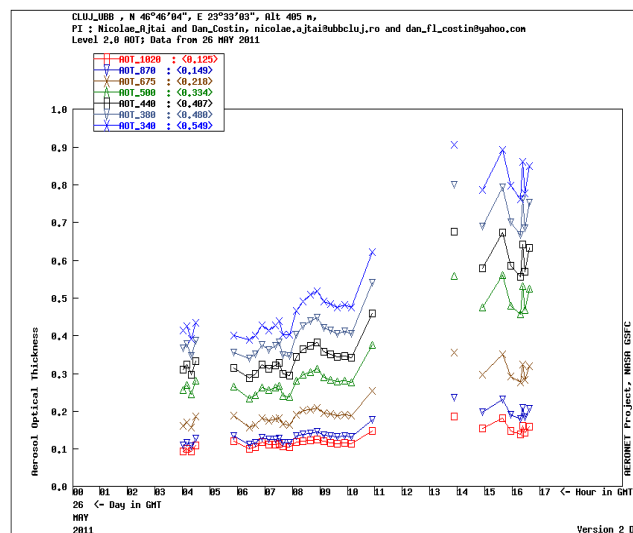
Fig. 7. Aerosol Optical Thickness (AOT) for 26st of May 2011 at *CLUJ_UBB*AERONET station
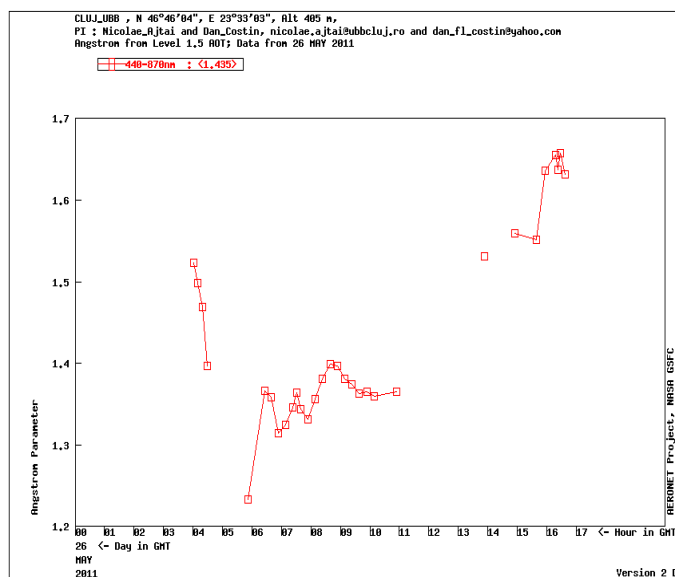
Fig. 8. Angstrom parameterfor 26st of May 2011 at *CLUJ_UBB*AERONET station

3.3. Biomass burning aerosols

The main sources of biomass burning aerosols are the wildfires which cover large surfaces in Eastern and Southern Europe (Fig.9) in the summer periods. The

145

resulting aerosols, which are subjected to long-range transport, can arrive over Romania.

Fig. 9. Fire Information for Resource Management System (FIRMS, 2012)

The particle size distribution for biomass burning aerosols is mainly dominated by the accumulation mode. The size of these particles increases the hazard they pose on human health, small particles penetrating deeper into the respiratory system.

The properties associated with small particle scattering can be observed [13], with high values of α (1.7 - 2.0), decrease of $\omega_0(\lambda)$ with increase of λ and a pronounced decrease of the asymmetry parameter to relatively low values.

Although biomass burning smoke is known as an absorbing aerosol due to its high concentration of black carbon produced by combustion, AERONET data show that the value of single scattering albedo ($\omega_0(\lambda)$) for smoke varies significantly for different origins, age, and type. A study regarding the North American forest fires [15] showed the dependency of $\omega_0(\lambda)$ as a function of time after ignition. Measurements showed an increase in $\omega_0(\lambda)$ as the fires progressed from intense burning ($\omega_0(\lambda) = 0.7$) to smoldering combustion ($\omega_0(\lambda) = 0.92$).

The hazards associated with biomass burning aerosols are represented by compounds containing nitrates, ammonium, sulphate, organic components and black carbon [16].

4. Conclusions

Long range transport of particles is a widespread phenomenon. The aerosols transported may include hazardous particles with different risk grades. We may conclude that the most hazardous particles for human beings are the volcanic ash particles. Health effects are not negligible, the inhalation of ash resulting in respiratory problems and eye irritation. Besides health effects, one of the most important risk factors concerns aircrafts, due to the strong corrosive effect of the ash injected to high altitudes, on the engines of the aircrafts. This results in an increased risk of malfunctions. Ash poses a hazard also to turbine blades and causes friction scratches on the windshield, resulting in poor visibility.

Dust has a major contribution to the loading of the atmosphere with aerosols, contributing tothe optical extinction of light through the atmosphere. Saharan dust intrusions may have an impact on visibility and on some occasions, when increased concentrations are present at ground level during the deposition, it can affect the human health.

Biomass burning aerosols may have a significant large–scale impact on radiative forcing and the climate system due to its high absorption.

Acknowledgements

REFERENCES

[1] Ajtai, N., Ştefănie, H., Costin, D., Ozunu, A., Comparative study of regional aerosols from columnar sunphotometric data in Romania, Papers presented at the 4th Workshop on Optoelectronic Techniques for Environmental Monitoring 2010, 37, ISSN 2066-8651.

[2] Ajtai, N.,Ştefănie, H.I., Ozunu, A., Description of aerosol properties over Cluj-Napoca derived from AERONET sun-photometric data, *Environmental Engineering and Management Journal*, 12(2), (2013).

[3] Ajtai N., Ştefănie, H., Stoian L.C., Oprea M.G., The volcanic ash and its impact on European air transport industry. A case study on the detection and impact of the theEyjafjallajökull

volcanic ash plume over North-Western Europe between 14th and 21st April 2010, *AES Bioflux* 2(1), (2010), 57-68.

[4] Mortier, A., Goloub, P., Podvin, T., Deroo, C., Chaikovsky, A., Blarel, L., Tanre, D. Ajtai, N., Detection and Characterization of Volcanic Ash Plumes over Lille during Eyjafjöll Volcano Eruption, *ACP/AMT Inter-Journal SI*, (2013).

[5] Nicolae, D.; Nemuc, A.; Mueller, D.; Talianu, C.; Vasilescu, J.; Belegante, L.; Kolgotin, A., Characterization of fresh and aged biomass burning events using multiwavelength Raman lidar and mass spectrometry, *Journal of Geophysical Research-Atmospheres*, 118(7), (2013), 2956-2965.

[6] ***AERONET, Aerosol Robotic NETwork, On line at: http://aeronet.gsfc.nasa.gov, (accessed in April 2014).

[7] *** GESDISC, Goddard Earth Sciences Data and Information Services Centre, Aerosol Optical Thickness, On line at:
http://daac.gsfc.nasa.gov/dataholdings/PIP/aerosol_optical_thickness_or_depth.shtml, (accessed in April 2014).

[8] Stefan, S., Mihai, L.,Nicolae, D.,Boscornea, A., Ångström turbidity in the lower layers of the troposphere, *Environmental Engineering and Management Journal*, 10, (2011), 133-138.

[9] Angstrom, A., On the atmospheric transmission of sun radiation and on dust in the air, *Geografiska Annale,* 11, (1929), 156–166.

[10] Dubovik, O., King, M.D., A flexible inversion algorithm for retrieval of aerosol optical properties from Sun and sky radiance measurements, *Journal of Geophysical Research.*, 105, (2000), 20673-20696.

[11] Draxler, R.R. and Rolph, G.D., *HYSPLIT (*HYbrid Single-Particle Lagrangian Integrated Trajectory)* Model access via NOAA ARL READY Website (http://www.arl.noaa.gov/HYSPLIT.php). NOAA Air Resources Laboratory, College Park, MD, 2013.

[12] BSC-DREAM8b (Dust REgional Atmospheric Model) On line at: http://www.bsc.es/projects/earthscience/BSC-DREAM/ (accessed in April 2014).

[13] Dubovik, O., Holben, B.N., Eck, T.F., Smirnov, A., Kaufman, Y.J., King, M.D., Tanre, D., Slutsker, I., Variability of absorption and optical properties of key aerosol types observed in worldwide locations*, Journal of Atmospheric Science*, 59, (2002),590-608.

[14] *** Rheinisches Institut für Umweltforschung, On line at: http://db.eurad.uni-koeln.de/de/index.php

[15] Radke, L.F., Hegg, D.A., Hobbs, P.V., Nance, J.D., Lyons, J.H., Laursen, K.K., Weiss, R.E., Riggan, P.J., Ward, D.E., Particulate and trace gas emissions from large biomass fires in North America.Global Biomass Burning: Atmospheric, Climatic, and Biospheric Implications, J. S. Levine, Ed., MIT Press, (1991), 209–224.

[16] Andreae, M.O., Merlet, P., Emission of trace gases and aerosols from biomass burning, *Global Biochemistry Cycle*, 15(4), (2001), 955–966.

FUEL TYPE AND ACCIDENT CONDITION INFLUENCE ON BLEVE FIRE CONSEQUENCES FROM AN INDUSTRIAL CHEMICAL PLANT

Hasan Hadi Salman KHWAYYIR, Daniel DINCULESCU, Gheorghe MARIA[*]

Depart. Chemical and Biochemical Engineering, POLITEHNICA University of Bucharest, 1-7 Gh. Polizu, 011061, Bucharest, Romania

Abstract

One of the most concern in (petro)chemical complexes including high-risk plants and reactors used for conducting highly exothermic hazadous reactions, refers to possible accident consquences when the chemical plants are located in a close proximity. This study highlights, by using a classical BLEVE fire model, the importance of the stock vessel size, plant capacity, operating severity, and fuel nature on the accident effects (radiative heat flux), consequences (P% of fatalities), and possible Domino effect occurrence at various distances from the fire source.

Keywords: accident consequences and effects, BLEVE fire, butane, alcohols

1. Introduction

(Petro)chemical plants belong to the category of the so-called "Critical Infrastructures (CI)" [1], that is social-economic structures which are vital elements for the proper functioning of a society. Apart from others CI-s like information technology, telecommunications, energy, transportation systems, emergency services, nuclear reactors, materials and waste, agriculture and food, defense industrial base, etc., the chemical CI-s are subjected to complex risk analyses, extensive and multi-layer plans for accident prevention and protection, all being focused on reducing the impact of possible chemical accidents leading to important casualties [2].

A quite large number of chemical plants belong to this category, by processing important quantities of hazardous substances at intense temperature and pressure conditions, or by conducting hazardous reactions or complex physico-chemical processes, all making these plants potential sources of severe accidents. Besides, due to a high level of interactions among chemical platform subsystems, and small

distances between plants, the accident consequences are worse often generating accidents in-chain (the so-called Domino effects [3,4]).

Even if such plants, including highly sensitive exothermic chemical reactors, are design to be operated under minimum risk conditions, the market pressure for getting a high plant productivity leads to set the nominal running point in the vicinity of the safety limits (in the parametric space). As a consequence, the presence of uncertainties in the runaway boundaries, random disturbances in operating parameters, raw-material / recycling variable conditions, catalyst replacement or reactivity modifications result in the presence of a low but not negligible technological risk in spite of a tight process control [5,6].

Runaway of such thermally sensitive plants may lead to severe fires when flammable substance and fuels are manipulated, or to the release of toxic puffs. The effects and consequences of such chemical accidents strongly depend on the accident conditions, plant location, severity of plant operation, on-site human population density, and equipment thermal sensitivity. The investigated process dynamics and accident scenarios involving the key-equipments are evaluated through valuable mathematical models for the accident source, outputs (explosions, fire, toxic substance dispersion), and consequences (percent of fatalities of humans). Finally, the plant operation risk results from a complex combination of the plant failure probability, and of the effects and consequences of a number of different accident scenarios [1,4].

The aim of this paper is to use the classical BLEVE fire model to evaluate the influence of accident conditions on its consequences and possible Domino effect occurrence involving storage tank / risky reactors manipulating hazardous fuels. Few common flammable substances of very different combustion heat are checked in this respect. The case studies include the butane storage tank of the maleic anhydride catalytic synthesis plant (with the reactor operated at 1.3-2 atm., 350-450°C, [5]), and alcohols used for biodiesel production (methanol and ethanol [7]). From safety reasons, the approached intermediate storage tanks do not contains stocks larger than the necessary for one week of plant continuous operation. Such BLEVE fires involving very flammable fuels may easily escalate generating accidents in chain. The considered fireball accident parameters refers to:

- The influence of the *fuel mass;*

- The influence of the *used model relationships* to evaluate the radiative heat flux at various distance from source;

- The influence of the *fuel heat of combustion* (butane and alcohols in this case).

2. BLEVE model relationships and application rule

The worst possible fire accident case considered in most of the chemical plant risk assessments is the fireball ("Boiling Liquid Expanding Vapour Explosion", BLEVE). Such an accident happens following a sudden loss of a flammable superheated liquid or liquefied gas from a pressure tank, leading to the rapid expansion of the liquid (flashing) to the atmosphere.

The blast wave, vessel fragment projectile speed, and fireball magnitude following the tank rupture depend on several factors [4,8]: type and properties of the released fuel, the produced expansion energy and its release rate, shape of the vessel, type of rupture the presence of neighboring reflecting surfaces. The materials below their normal boiling point do not produce BLEVE fires.
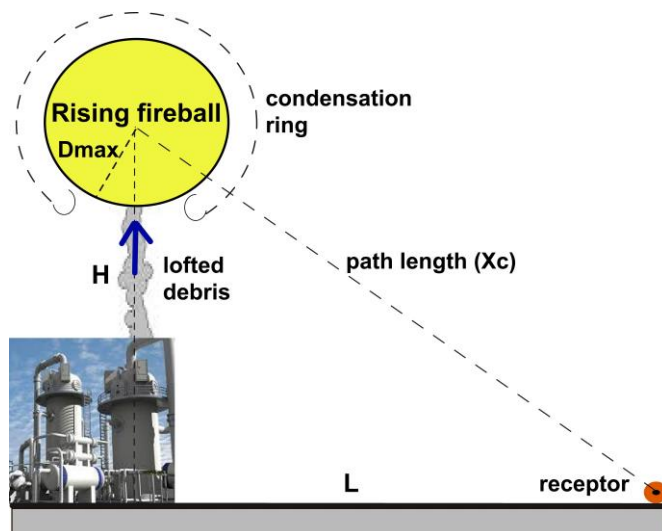
Fig. 1. Geometry of a BLEVE fireball.

The effects and consequences of the fireball depends on the flammable liquid combustion heat, its boiling point / vapour pressure, the released mass, and the distance to the receptor. The BLEVE characteristics (i.e. fireball diameter, combustion duration, center height of fireball, and thermal emissive power, Table 1, Fig. 1) can be satisfactorily modelled by using empirical correlations with the released fuel mass and type, and athmospheric conditions (Table 1). Eventually, these relationships lead to evaluate the received thermal flux by a receptor (humans, equipment, etc.) located at a given distance from fire source. This flux is necessary to evaluate the received thermal radiative dose (DTL) and fire consequences (P% of fatalities) using the relationships given in the Table 1. The

received thermal radiation can be evaluated using various assumptions using the horizontal, or vertical receptor surface model, the Roberts' formula, or the Hasegawa-Sato formula. More conservative predictions are given by taking the maximum of radiative heat flux predicted by all these models.

Table 1

BLEVE fire and Probit models for evaluating the radiative heat flux at the receptor, and fatality levels at various distances from source (after AIChE [4]; Maria et al. [3]).

Variable	*Relationship*
Maximum diameter of the fireball	$D_{max} = 5.8M^{1/3}$, (m)
Fireball combustion duration	$t_{\text{BLEVE}} = 0.45M^{1/3}$ (for $M < 30$ t) , (s)
	$t_{\text{BLEVE}} = 2.6M^{1/6}$ (for $M > 30$ t) , (s)
Center height of fireball	$H_{\text{BLEVE}} = 0.75\, D_{max}$, (m)
Initial ground level hemisphere diameter	$D_{initial} = 1.3\, D_{max}$, (m)
The emitted flux at fireball surface	$E = R\, M\, H_c\, /(\pi\, D_{max}^2 t_{\text{BLEVE}})$, (kW m^{-2})
The horizontal geometrical view factor between fireball and receptor	$F_{21,\text{hor}} = H_{\text{BLEVE}}\, (0.5D_{max})^2/(L^2 + H_{\text{BLEVE}}^2)^{1.5}$
The vertical geometrical view factor between fireball and the receptor	$F_{21,\text{ver}} = L\, (0.5D_{max})^2/(L^2 + H_{\text{BLEVE}}^2)^{1.5}$
Path length from fireball center to the receptor	$X_c = \sqrt{H_{\text{BLEVE}}^2 + L^2}$, (m)
Path length from fireball surface to the receptor	$X_s = \sqrt{H_{\text{BLEVE}}^2 + L^2}$ - $0.5D_{max}$, (m)
Water partial pressure in air [9]	$p_w = 101325\, R_H \exp(14.4114 - 5328/T_a)$, (Pa)
Atmospheric transmissivity	$\tau_{\text{air}} = 2.02(p_w\, X_s)^{-0.09}$
Received flux at horizontal receptor	$E_{r,\text{hor}} = \tau_{\text{air}}\, E\, F_{21,\text{hor}}$, (kW m^{-2})
Received flux at vertical receptor	$E_{r,\text{ver}} = \tau_{\text{air}}\, E\, F_{21,\text{ver}}$, (kW m^{-2})
Received flux (formula of Roberts)	$E_{r,\text{R}} = 2.2 \cdot 10^{-3} R H_c M^{2/3}/(4\pi\, X_c^2)$, (kW m^{-2})
Received flux (Hasegawa-Sato rule)	$E_{r,\text{RHS}} = 828 \cdot M^{0.771}/ X_c^2$, (kW m^{-2})
Maximum radiative heat flux	max ($E_{r,\text{hor}}$, $E_{r,\text{ver}}$, $E_{r,\text{R}}$, $E_{r,\text{RHS}}$), (kW m^{-2})
Probit variable (Y) (E_r in W m^{-2})	$Y = -14.9 + 2.56\, \ln\!\left(t_{\text{BLEVE}} E_r^{4/3} / 10^4\right)$
Thermal radiation intensity threshold	4.7 kW m^{-2}

Notations: M = initial mass of the fuel in the fireball (kg); L = distance from fireball center to the receptor at ground level (m); H_c = heat of combustion (kJ kg^{-1}); R = radiative factor of H_c (adopted R = 0.4, for fireballs from vessels bursting at or above the relief set pressure); T_a = ambient air temperature (K); R_H = relative humidity of air (%).

The fireball accident consequences can be expressed by means of various models (e.g. F-N curves [4]), but the most common rule uses the Probit variable $Y(x)$ evaluated at various distances (x) from source, and log-linearly

correlated with the received thermal radiative dose. Consequently, the fatality level $P(Y_{fuel}(x))$, that is P% human fatalities resulting from the exposure of a population to the radiative dose DTL at various distances x from the fire source, can be evaluated by means of the general relationship [4,8]:

$$P\% = 50\left[1 + \frac{Y-5}{|Y-5|}\,erf\left(\frac{Y-5}{\sqrt{2}}\right)\right], \text{ with } Y = Y_{fuel} = k_1 + k_2\ln(\text{DTL}) \quad (1)$$

where k_1 and k_2 are given in Table 1, while the thermal radiative dose DTL = $t_{\text{BLEVE}}E_r^{4/3}/10^4$ is evaluated by using the BLEVE model.

3. Analysis of the case study

The analysis of the influence of BLEVE fire accident conditions on the accident consequences is based on scenario simulations using nominal, but also minimum, and maximum values of the model parameters specified in Table 2 for the three considered fuels (butane, methanol, and ethanol stock vessels).

Table 2

The fire conditions and BLEVE model parameter range considered in the accident sensitivity analysis. The receptor is situated at maximum L = 300 m from fire source. The ambiental temperature is 298 K. The Pasquill class of stability is D (neutral).

Model parameter	Nominal value (model)	Other tested values (models)
Type of model for the received flux at the receptor (Er, kW/m^2)	Maximum (Er)	Roberts' model
Heat of Combustion of fuel (kJ/kg)	49700 (butane)	30540 (ethanol) 23000 (methanol)
Fuel mass in the stock tank at the ignition moment (1 day stock = 10 t)	3 days stock (30 t)	1 days stock (10 t) 7 days stock (70 t)

Apart from the maximum radiative heat flux model, the Robers' formula was also considered as being explicitly correlated with the combustion heat (while RHS model does not explicitly include this term). The BLEVE model outputs are the followings:
- Maximum fireball diameter
- Fireball combustion duration
- Fireball height
- Radiative heat flux (E_r) at various distances from source
- Heat radiative dose (DTL), and P% of fatalities at various radius around source.

4. Results discussion and conclusions

The analysis of the influence of fireball accident conditions on its consequences is based on scenario simulations using combinations of parameters and models specified in Table 2. The tank blast involving the butane, methanol, and ethanol fuel feeding the maleic anhydride and biodiesel production plants respectively is considered over three different scenarios, depending on its filling level ensuring one day, three days, or seven days raw-material stock for continuous plant operation.
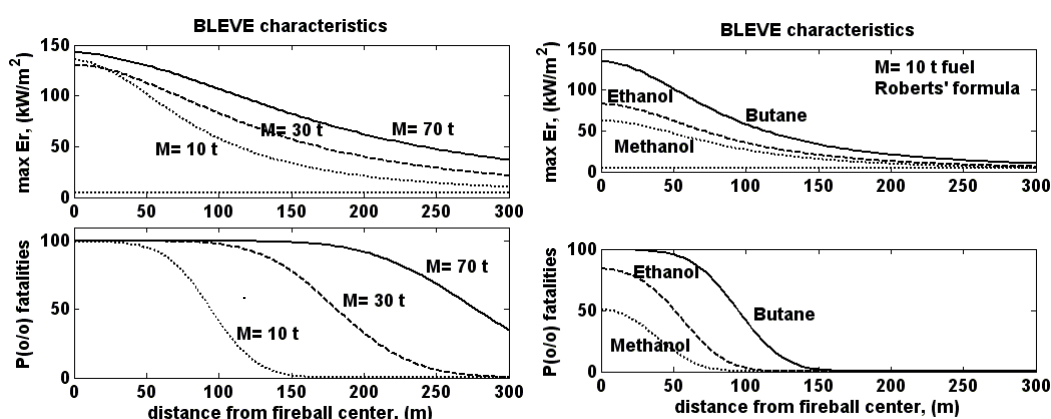
Fig. 2. (left) The influence of the fireball fuel mass (butane fuel, BLEVE model with the Max *Er* formula) and, (right) of the combustion heat of the fuel (butane, ethanol, and methanol for a *M* = 10 t stock; BLEVE model with only Roberts' formula) on the accident effects (radiative flux *Er*, and P% of fatalities) at various distances from the fireball center (nominal conditions of Table 2).

Scenarios simulations lead to the following conclusions:

- The effect of tank *fuel mass* on the fireball scale is very high (left of Fig. 2), the percentage of fatalities P(%) and emitted radiative flux (*Er*) sharply increasing with the involved fuel mass in the fire. As expected, the worst scenario corresponds to the level of 7 days butane-stock, the value of *Er* being higher than the threshold of 37.5 kW m^{-2} [4] causing damages to the process equipment over more than 300 m radius (P% > 40%). Even if the calculated fireball life-time is short (10-30 seconds) compared to reported minutes required to cause serious plant damages, the flux intensity is very high (usually 150-400 kW m^{-2} at source) possible generating Domino effects in a close vicinity [3].
- The effect of the *used model* (see Table 1 relationships) to calculate the radiative heat flux is also very important (see Roberts' formula results in Fig.

2-right vs. the maximum radiative flux model results in Fig. 2-left). To generate risk assessment in the worst possible scenario, the Max (Er) formula is recommended. In any simulated alternative, the dangerous radius around fireball where the radiative flux $E_r > 37.5$ kW m^{-2} is about 150 m. Also the possibility of Domino effects generation should be taken into account in complex accident scenario studies.

- The influence of the fuel *heat of combustion* on the accident consequences, that is P% fatalities and radiative heat flux (E_r) is also very high. The higher is the combustion heat (i.e. butane fuel case) the greater is fireball effect, thus leading to high fatality levels over a larger radius around the fire source (Fig. 2-right). The methanol tank used for biodiesel fuel production exhibits the lowest fire consequences under similar accident conditions.

As a general conclusion, the BLEVE-fire model is proving to be suitable for simulating various accident scenario consequences involving industrial plants. Such models are quite flexible, by accounting for the accident source size, fireball scale, and environmental conditions. The study points-out the tremendous importance of considering all parameters influencing the accident magnitude and occurrence risk directly related to the plant operating severity, its location, hazardous raw-material stock level, plant proximity, etc.

Such a risk assessment analysis associated to sensitive chemical plants is of significant importance in the process design phase, but also during the process operation and risk management, by adjusting the severity of plant operation conditions vs. the associated risk. Such a complex accident consequence analysis, completed with evaluation of the incident occurrence frequency may lead to valuable conclusions related to the dangerous operating conditions of the chemical plants.

Notations

$D_{initial}$	-	initial ground level fireball hemisphere diameter
D_{max}	-	maximum diameter of the fireball
E	-	the emitted flux at the surface of the fireball
E_r	-	thermal radiation flux received by the receptor
F_{21}	-	geometrical view factor between fireball and the receptor
H_{BLEVE}	-	center height of fireball
H_c	-	heat of combustion
L	-	distance from fireball center to the receptor at ground level
M	-	molar H_2/NB feed ratio, or initial mass of the fuel in the fireball
p_w	-	water partial pressure in air
$P\%$	-	percentage of fatalities

R	-	radiative factor of H_c
R_H	-	relative humidity of air
t_{BLEVE}	-	fireball combustion duration
T_a	-	ambient air temperature , or cooling agent temperature
x	-	axial distance
X_c	-	path length from fireball center to the receptor
X_s	-	path length from fireball surface to the receptor
Y	-	probit variable

Greeks

τ_{air}	-	atmospheric transmissivity

Index

a	-	ambient air
hor	-	Horizontal
max	-	Maxim
o	-	Initial
ver	-	Vertical
w	-	Water

Abbreviations

BLEVE	-	boiling liquid expanding vapour explosion
CI	-	Critical infrastructure
DTL	-	toxic dose

REFERENCES

[1] Gheorghiu, A.D., Nour E., Ozunu A., Critical infrastructure protection in Romania. Evolution of the concept, vulnerabilities, hazards and threats. *AES Bioflux*, 5(2), (2013), 148-157.

[2] Gheorghiu, A.D., Influence of natural hazards on critical infrastructure, PhD Thesis, University Babeş-Bolyai, Cluj-Napoca, 2013.

[3] Maria, G., Dinculescu, D., Khwayyir, H.H.S., Proximity risk assessment for two sensitive chemical plants based on the accident scenario consequence analysis, *Asia-Pacific Journal of Chemical Engineering*, 9, (2014), 146–158. DOI: 10.1002/apj.1755.

[4] AIChE, Guidelines for chemical process quantitative risk analysis, AIChE, New York, (2000), 2nd edition.

[5] Maria, G., Dan, A., Setting optimal operating conditions for a catalytic reactor for butane oxidation using parametric sensitivity analysis and failure probability indices, *Journal of Loss Prevention in the Process Industries, 25, (*2012), 1033-1043.

[6] Maria, G., Dan, A., Derivation of critical and optimal operating conditions for a semi-batch reactor under parametric uncertainty based on failure probability indices. *Asia-Pacific Journal of Chemical Engineering*, **7**, (2012), 733-746.

[7] *** *Wikipedia Encyclopedia,* Biodiesel production, Wikimedia Foundation, Inc., San Francisco (CA), 2014. http://en.wikipedia.org/wiki/Biodiesel_production

[8] Maria, G., Chemical process quantitative risk analysis and modelling of accident consequences, Printech Publ., Bucharest, (2007) (in Romanian).

[9] Mudan K.S., Croce, P.A. Fire hazard calculations for large open hydrocarbon fires, *SFPE Handbook of Fire Protection Engineering*, Society of Fire Protection Engineers, (1988) Boston (MA).